



TECHNISCHE
UNIVERSITÄT
WIEN
Vienna University of Technology

Unterschrift des Betreuers

DIPLOMARBEIT

Insights from strong-coupling diagrammatic methods

The temperature dependence of the scattering rate in cuprates

Ausgeführt am Institut für
Festkörperphysik
der Technischen Universität Wien

supervised by
Associate Prof. Dr. Alessandro TOSCHI

co-supervised by
Dr. Thomas SCHÄFER
Dr. Georg ROHRINGER
Prof. Ph.D. Alexey N. RUBTSOV

by
B.Sc. Marie-Therese PHILIPP
Georg Sigl-Gasse 11/8
A-1090 Wien, Österreich
marie-therese.philipp@riken.jp

Datum

Unterschrift (Student)

The temperature dependence of the scattering rate in cuprates:
Insights from strong-coupling diagrammatic methods

Die Temperaturabhängigkeit der Streurrate in Kupraten:
Erkenntnisse aus stark-koppelnden diagrammatischen Methoden

Master thesis, (2017)

Institut für Festkörperphysik, TU Wien, Karlsplatz 13, Vienna, Austria

Russian Quantum Center, Novaya street 100, Skolkovo, Moscow, Russia

Abstract

Cuprates—beyond the unconventional superconductivity—feature an extraordinarily rich phase diagram, which has yet to be described in its full complexity. Among the various distinct phases, the DC resistivity most characteristically changes its temperature (T) dependence.

Notwithstanding, in 2015 novel experimental findings [1] by N. Barišić *et al.* have revealed a surprising universal temperature behaviour. In particular, the ratio of the DC resistivity over the Hall resistivity ρ/ρ_H a very clear T^2 -dependence. This appears universally for the pseudogap phase, the strange metal phase, and the Fermi liquid phase across all hole-doping and temperature regimes, as well as in different compounds.

In our work, we analyzed a possible connection between the experimentally observed quadratic T -dependence of ρ/ρ_H and the T -dependence of the electronic scattering rate. Our numerical calculations are based on the two dimensional single-band Hubbard model on a square lattice with next, 2nd next and 3rd next nearest neighbor hopping.

Due to the combination of low dimensionality and strong electronic correlations in this system, non-local correlations are likely to provide important contributions to the solution. On the basis of this consideration we employed the ladder dynamical vertex approximation (D Γ A) and the dual fermion (DF) theory, i.e. cutting edge many-body algorithms, capable of including antiferromagnetic fluctuations on all length scales.

The D Γ A and DF results yield strongly momentum dependent single particle quantities such as the electronic self-energy on the Matsubara axis. For the hole-dopings $\delta = 0.1, 0.15$ and 0.2 we have observed that the momentum dependence appears stronger at small doping. To be more quantitative we approximated the scattering rate by two methods:

First, we obtained the scattering rate by extracting the value of the imaginary part of the self-energy at the Fermi level. To this end we performed an analytic continuation of the Matsubara data by means of Padé approximation. Although the spectral function gave rise to plausible trends, the analytic continuation fails to reveal the T -dependence due to large uncertainties, which are intrinsic to the ill-defined problem of analytic continuation.

Second, we approximated the spectral weight at the Fermi surface by means of the single-particle Green's function at the imaginary time point equal to half the inverse temperature. In our case this could *not* be directly interpreted in terms of the scattering rate, though.

Although we were not able to produce a stable prediction for the scattering rate the D Γ A results revealed two physically interesting results: (i) The spin susceptibility shows commensurate and incommensurate fluctuations accompanied by a characteristic T -dependence of the correlation length w.r.t. the doping level in the intermediate

temperature regime. (ii) The self-energy on the Matsubara axis strongly suggests the presence of a pseudogap as well as the absence of any universal behaviour w.r.t. different doping or different temperature regimes.

We hence see the necessity to go beyond the single-particle scattering rate in order to describe the experimentally observed T -dependence of ρ/ρ_H . In particular, we became aware of expressions in the literature, which treat ρ/ρ_H within the linear response theory. In this work, we merely sketch them as a possible preparation for future studies in terms of the charge susceptibility.

Kurzfassung

Kuprate besitzen, neben der unkonventionellen Supraleitung, ein außerordentlich vielseitiges Phasendiagramm, das bislang nicht in seiner vollständigen Form beschrieben werden konnte. Innerhalb der unterschiedlichen Phasen weist insbesondere der Widerstand des Gleichstroms kennzeichnende Temperaturabhängigkeiten auf.

Gleichwohl legten aktuelle experimentelle Ergebnisse [1] von N. Barišić *et al.* eine unerwartet einheitliche Temperaturabhängigkeit dar. Eingehend handelt es sich um eine quadratische Temperaturabhängigkeit des Verhältnisses des Widerstandes bei Gleichstrom und des Hall-Widerstandes ρ/ρ_H . Diese tritt für jedwede Lochkonzentration und jeglichen Temperaturbereich gleichsam auf, sofern das System sich innerhalb der Phase der Pseudo-Energielücke, der seltsamen Metallphase oder der Fermiflüssigkeitsphase befindet.

In der vorliegenden Arbeit, haben wir die Möglichkeit eines Zusammenhanges der experimentell festgestellten quadratischen Temperaturabhängigkeit von ρ/ρ_H und der Temperaturabhängigkeit der elektronischen Streurrate untersucht. Unsere numerischen Ergebnisse basieren auf dem Ein-band Hubbard Model für ein zweidimensionales quadratisches Gitter mit Nächsten-nachbar-, Zweit- und Drittnächstennachbarhüpfen.

Aufgrund der Kombination aus Niederdimensionalität und starken elektronischen Korrelationen innerhalb des Systemes, ist es naheliegend, dass nicht-lokale Korrelationen von hoher Bedeutung für die Lösung sind. Aus diesem Umstand heraus verwenden wir die Leiterversion der dynamischen Vertexapproximation (D Γ A) und die Theorie der Dualfermionen (DF), und somit führende Algorithmen im Bereich der Vielteilchenphysik, um antiferromagnetische Fluktuationen jeder Größe zu berücksichtigen.

Die D Γ A und DF Ergebnisse ergeben eine starke Impulsabhängigkeit der Einteilchen Größen auf der Matsubara-Achse. Für die betrachteten Lochkonzentrationen von $\delta = 0.1, 0.15$ und 0.2 ist die Impulsabhängigkeit für kleinere Konzentrationen größer. Die Streurrate wird auf zwei Arten abgeschätzt:

Einerseits bestimmen wir die Streurrate durch Bestimmung des Imaginärteils der Selbstenergie am Ferminiveau. Dafür wurde eine analytische Fortsetzung der Matsubara-Daten mithilfe von Padé Approximation durchgeführt. Obwohl die Spektralfunktion plausible Tendenzen gezeigt hat, hat die analytische Fortsetzung aufgrund der dem Problem intrinsischen Unbestimmtheit zu große Unsicherheiten geliefert, um eine Temperaturabhängigkeit zu bestimmen.

Andererseits, haben wir das spektrale Gewicht auf der Fermifläche mithilfe der Einteilchen-Green Funktion am Punkt der Imaginärzeit gleich der Hälfte der inversen Temperatur bestimmt. Dieses kann hier jedoch nicht in Form der Streurrate interpretiert werden.

Obwohl es uns nicht möglich war eine stabile Vorhersage für die Streurate zu treffen, liefern die DGA Resultate zwei physikalisch interessante Ergebnisse: (i) Die Spinsuszeptibilität zeigt Kommensurabilität und Inkommensurabilität begleitet durch eine kennzeichnende Temperaturabhängigkeiten der Korrelationslänge bzgl. der Dotierung. (ii) Die Selbstenergie gegeben auf der Matsubara-Achse deutet stark auf die Anwesenheit der Pseudo-Energielücke hin, und ebenso die Abwesenheit jeglichen universellen Verhaltens weder bzgl. der der Dotierung noch des Temperaturbereiches.

Wir sehen daher die Notwendigkeit eine umfassendere Beschreibung als die Einteilchenstreurrate aufzubauen, um die experimentell beobachtete Temperaturabhängigkeit von ρ/ρ_H zu beschreiben. Im Speziellen haben wir in der Literatur Ausdrücke ausgemacht, welche ρ/ρ_H innerhalb der linearen Antworttheorie behandeln. In der vorliegenden Arbeit wird lediglich die Vorbereitung für eine eingehende kommende Studie, welche auf die Ladungssuszeptibilität eingeht, präsentiert.

Acknowledgments

At this point I would like to show gratitude towards the many people who have contributed to this work. My interest in the study of the scattering in cuprates started during my master's course at TU Wien at the institute of solid state physics. In particular, I would like to thank my supervisor Prof. Alessandro Toschi for his inspiring guidance towards and within this project. This work would have certainly not been possible without the patience and effort of Thomas Schäfer and Georg Rohringer. And with special emphasis I would like to thank Prof. Alexey N. Rubtsov for discussions and his hospitality at the Russian Quantum center, where I deeply enjoyed my stay.

This project was enabled by the effort of the people who implemented the numerical methods and composed the code snippets that form the foundation for this work. In conjunction with the DΓA code I would like to thank A. Toschi, T. Schäfer and G. Rohringer for the base and Clemens Watzenböck for implementing higher order hopping terms. Furthermore, in regards to the DF code I thank Hartmut Hafermann for the permission to use the code package pydual and his guidance in this regard.

I am grateful for fruitful discussions with Prof. Ryotaro Arita, Shiro Sakai, Prof. Masatoshi Imada, Jan Tomczak, as well as Prof. Karsten Held and all members of his group, who vividly exchange ideas on a daily basis.

I would also like to acknowledge financial support from the Austria-Russia FWF Joint project “Quantum criticality in strongly correlated magnets” project no. I 610-N16, and the SFB ViCoM F41 project P15: “Kollektive Phaenomene in dünnen Schichten und Heterostrukturen von Oxiden” (no. F 4115-N28).

I dedicate this work to my grandma who was not allowed to study. Times have certainly changed. I am grateful to my parents and my entire family in Styria, Vienna and Germany for nourishing my curiosity. And finally I am grateful for the free Austrian educational system.

Tokyo, 11. Dezember 2017

Marie-Therese Philipp

Meiner Familie und Stephan.

Contents

1. Introduction	2
1.1. Brief phenomenology of cuprates	3
1.2. Novel experimental findings	5
1.3. Ansatz	8
1.4. Outline	11
2. Model	13
2.1. Intuitive picture	13
2.2. Viewpoint of realistic material calculations	15
2.3. The Hubbard model in quantum field theory (QFT)	20
2.4. Parameters to model cuprates	22
3. Methods	24
3.1. Dynamical mean-field theory (DMFT)	24
3.1.1. Anderson impurity model (AIM)	25
3.1.2. Self-consistency loop	26
3.1.3. Exact Diagonalization (ED)	28
3.2. Diagrammatic extensions to DMFT	29
3.2.1. Diagrammatics at the two particle level	30
3.2.2. Dynamical vertex approximation (D Γ A)	32
3.2.3. Dual fermion (DF) theory	37
3.3. Pad \acute{e} Approximation	40
4. Results	45
4.1. The self-energy	46
4.1.1. DMFT	48
4.1.2. D Γ A	52
4.1.3. DF	65
4.2. The ratio ρ/ρ_H	70
5. Conclusion and Outlook	79
Appendices	82
A. Crystal structure	83
B. Derivations	85
B.1. The fermionic coherent state path integral	85

Contents

B.2. Filling and chemical potential	89
B.3. The hybridization function of AIM	91
B.4. Lehmann representation of one-particle Green's function	92
B.5. Hubbard Stratonovic transformation	93
B.6. Padé fit for $n = 4$	94
C. Formalism	96
C.1. Sum convention	96
C.2. n-particle Green's functions	96
C.3. Fourier transformation and Matsubara frequencies	96
D. Angle-resolved photoemission spectroscopy (ARPES)	98

1. Introduction

Gut Ding braucht Weile.

Volksmund

Superconductivity (SC) has been driving advances in condensed matter physics for decades. At the beginning of the 20th century, the first superconductors were discovered [2]. These materials have two main properties below a critical temperature T_c : Zero electric resistivity and they expel magnetic field lines [3]. These properties make these materials both, fundamentally and technically appealing. The first samples featuring SC were simple metals with T_c below 10 K. The following decades revealed more metals and metallic alloys with increasing T_c up to almost 30 K. Clearly, most of the desired technological or commercial application remained far out of reach, and at the same time, so did an acceptable explanation of the phenomenon.

Not until 46 years after the discovery of SC, the well-known BCS theory [4–7] was established. In this theory J. Bardeen, L. N. Cooper and R. Schrieffer successfully described the microscopic mechanism in metals and metallic alloys, which we now call conventional SC. Here, an arbitrarily small attractive interaction between electrons leads to the formation of Cooper pairs. Electronic states close to the Fermi level become unstable and create pairs of opposite momentum, which act as Bosons. These Bosons form a Bose-Einstein condensate at the Fermi surface, while opening a gap in the excitation spectrum.

The goal to find SC at room temperature was still unattainable. Another three decades passed before the first unconventional superconductor brought a slight twist. In 1986 J. G. Bednorz and K. A. Mueller discovered a lanthanum and copper oxide compound [8], which becomes superconducting upon doping with barium. At that point the copper age of SC started. Many copper oxide-based materials, that are now known as cuprates, were discovered to display SC upon doping. The value of T_c quickly rose up to 135 K. Even to this day, cuprates classify as high temperature superconductors (HTSCs). The vague definition of HTSCs addresses materials with T_c roughly above 40 K. It is often used as a synonym for unconventional superconductors. However, unconventional SC in fact refers to all superconducting mechanisms that are not understandable within the BCS theory.

It has been 31 years since their discovery and we remain in anticipation of a theory that explains the complexity of HTSCs. In particular, the very different phases found in cuprates demand better understanding. Although SC may be characteristic of the most desirable phase, other phases in cuprates intrigue by means of nontrivial fluctuations. In the subsequent section, we briefly explore the extent of their phenomenology. Thereafter

we want to highlight novel experimental findings that shaped the onset of this work. In the present scope the electronic scattering rate is investigated by means of a model generally aimed to represent cuprates. The ansatz and outline in the end of this chapter offer more insight with respect to the employed model and methods.

1.1. Brief phenomenology of cuprates

Cuprates are a class of materials that consist of copper-oxide (CuO_2) planes. The electronic properties that arise from these quasi-two dimensional planes dominate the physics of cuprates. In this section, we want to recall commonalities among cuprates and explore what features are characteristic of a cuprate phase diagram. However to grasp the amount of material that belong to the class of cuprates, it seems necessary to mention some details with respect to the classification of cuprate compounds.

The CuO_2 -planes are embedded in buffer layers that can consist of various elements. A first categorization of cuprates is often made in terms of the elements that appear in these buffer layers. For instance, in the present work we will mainly refer to mercury based compounds, where the buffer layer is HgO_δ . δ is an oxygen induced hole-doping. Moreover, the unit cell of a compound may consist of one or multiple layers of CuO_2 -planes which are separated by an additional ion, such as Ca in the case of Hg-based compounds. The electronic structure of distinct CuO_2 -planes inside one unit cell couple weakly¹ and slightly change the electronic response. Therefore, it is most common to clarify two aspects, when reporting about one type of cuprate: Firstly, the basis element in the buffer layer, and secondly, the amount of CuO_2 -layers in one unit cell.

Let us briefly introduce the phase diagram of cuprates, which is shown in Figure 1.1. Along, we will mention some experimental observations that are common to all compounds.

The parent compound² is an antiferromagnetic insulator (AF) below the Neèl temperature T_N . This phase seems to be well-understood in terms of [10] an antiferromagnetic charge transfer insulators. This is a specific case of the well-known Mott insulator, where the conducting band is split into upper and lower Hubbard band due to strong electronic correlations. A charge transfer insulator features a filled band in between the Hubbard bands. Nevertheless the central point w.r.t. experimental observations of the parent compound is represented by the localization of spins in a checkerboard manner.

A small doping to either hole or electron abundance leads to a rapid decrease of T_N . The mentioned filled band in between the Hubbard bands leads to an inherent particle-hole asymmetry. This immediately reflects in the fact that the antiferromagnetic dome is more robust to electron doping than hole doping.

Furthermore, on both sides of the antiferromagnetic phase a superconducting dome (SC) emerges below a critical temperature T_c . The superconducting phase features the

¹High-energy electron spectroscopy (EELS and XAS) demonstrated the quasi two-dimensional nature [9] of the system by means of a polarization analysis. It showed that only a small fraction of the spectra is due to Op_z and $\text{Cu}3d_{3z^2-r^2}$ states.

²The material without doping is called parent compound.

1. Introduction

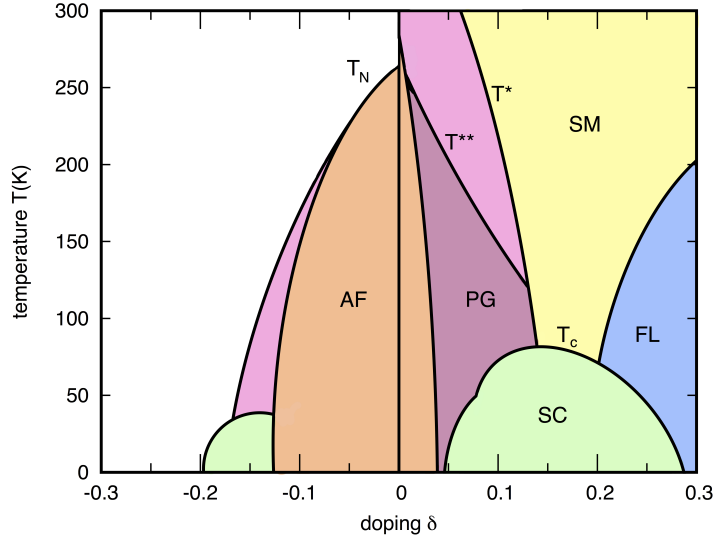


Figure 1.1.: Prototypical phase diagram of cuprates. The left and right hand side correspond to hole and electron doping, respectively. The phases shown are the antiferromagnetic insulator (AF), the superconducting dome (SC), a pseudogap region (PG), a strange metal phase (SM), as well as the Fermi liquid regime (FL).

basic properties of superconductors: Zero resistivity, the Meissner Effect, the Josephson effect, the isotope effect, an anomalous specific heat capacity and abnormal infrared electromagnetic absorption. A direct measurement of the flux quantum ($hc/2e$) has shown that Cooper pairs with charge $2e$ occur and the superconducting gap was unambiguously detected via tunneling experiments [11]. In contrast to known conventional superconductors, in the case of cuprates angle-resolved photoemission spectroscopy (ARPES) [12] captured an anisotropic superconducting gap. The superconducting gap function has a $d_{x^2-y^2}$ -type symmetry with nodes on the Fermi surface in the direction of $\mathbf{k} = (\pm\pi, \pm\pi)$. At this so-called nodal point the superconducting gap function is zero and changes its sign.

The superconducting dome appears in a wider range of doping and features a higher value for T_c in the hole-doped case. This roughly serves as a motivation to continue our discussion on the hole-doped side of the phase diagram. Note, that the doping concentration that features the maximum of T_c is called *optimal doping*. It is approximately at 15% hole concentration. The region of lower doping is the so-called *underdoped regime*, while upon higher doping the *overdoped regime* is entered.

The normal state above the superconducting dome features an unexpected amount of peculiar phases. The most mentioned phase is the pseudogap phase (PG) located in the underdoped regime. The most characteristic property of the pseudogap phase is the suppression of spectral weight on specific parts of the Fermi surface. ARPES measurements prominently show arcs at the nodal point, while a spectral gap forms towards the boundary of the first Brillouin zone. The point closest to the boundary,

1. Introduction

which is furthest from the nodal point, is called anti-nodal point. The pseudogap phase is entered below a crossover temperature T^* and can only be called phase to a certain extent. Within this region there is experimental evidence for a multitude of fluctuation, such as stripes emerging due to charge density waves as well as a changing temperature dependence of transport coefficients in different parts. This very rich and different phenomenology makes it somewhat troublesome to refer to it as a single phase.

Directly above the optimal doping a strange metal phase (SM) emerges in a funnel-shaped way up to high temperatures. The main characteristic of this regime is an unconventional temperature dependency of transport coefficients. This is often referred to as non-Fermi liquid like behaviour or bad metal, as it cannot be easily interpreted in terms of a Fermi liquid mass renormalized picture. The shape of this phase motivated theoretical discussions about a hidden quantum critical point [13], however in the present work this path is not explored.

Finally, upon inducing a large hole concentration a Fermi Liquid phase (FL) is recovered. This essentially refers to the fact that a normal metallic behaviour is restored. From the viewpoint of strongly correlated electron systems we can easily understand this as a result of diluting the system. Thus, electronic correlation effects lose their influence.

Hitherto, the phase diagram shown in Figure 1.1 has been theoretically described only by focusing on single specific regions. Moreover, experimental findings continue to refine nuances in the phenomenology of the appearing phases. These details in observation are not only derived from contributions of specific compounds as we will see in the subsequent section.

1.2. Novel experimental findings

In the previous section, we have briefly reviewed the discovery of superconducting materials and in particular copper-based superconductors, so-called cuprates. Subsequently, we discussed the most striking phenomenology of cuprates and mentioned that, despite many approaches, no complete theory for this class of materials has been formulated yet.

Very recently, novel experimental findings are promising to give new insight. The remarkable feature is, that the observed properties are compound and doping independent. In other words, phases that otherwise look very distinct and are only well-described by fundamentally different models, would be characterized by one single property, unique in the entire phase diagram.

In the experiment [1], N. Barišić *et al.* have measured the DC resistivity and the Hall coefficient of the compound $\text{HgBa}_2\text{CuO}_{4+\delta}$ with doping (δ). In Chapter 2, we will elaborate on the structure of the compound, while in the following we briefly illustrate the corresponding experimental measurements, before discussing the experimental results.

▶ Hall experiment 

1. Introduction

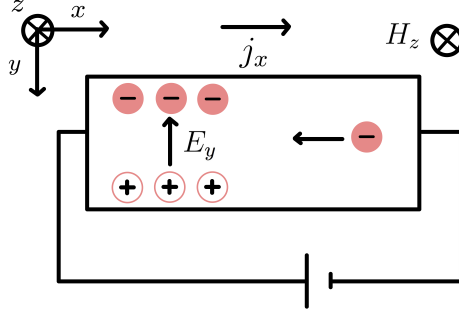


Figure 1.2.: Hall experiment in the Drude picture. A current density $j_x = ev_x n$ is carried by electrons. The applied magnetic field H_z induces a charge imbalance. As a result a Hall electric field E_y emerges in compensation of the Lorentz force $-eE_y - ev_x H_z = 0$.

The DC resistivity (ρ) is the resistance along a unit distance in the direction parallel to an applied electric field (E_x). The basic dimension $[\text{mass}][\text{length}]^3[\text{time}]^{-3}[\text{current}]^{-2}$ can be expressed as Ωm . The inverse point of view is to consider the conductivity σ . It is the tensor valued linear response function of the electrical current \mathbf{j} due to an external electro-magnetic perturbation (here: E_x), hence

$$j_\alpha = \sigma_{\alpha\beta} E_\beta. \quad (1.1)$$

$$\text{Here: } j_x = \sigma_{xx} E_x, \quad (1.2)$$

where the off-diagonal entries vanish as a result of the Lorentz force,

$$\mathbf{F}_L = q[\mathbf{E} + (\mathbf{v} \times \mathbf{H})], \quad (1.3)$$

acting on a charge q , where we consider the case that the magnetic field within the material $\mathbf{H} = 0$. The DC resistivity in x -direction is therefore given as

$$\rho = \frac{1}{\sigma_{xx}}. \quad (1.4)$$

The Hall resistivity (ρ_H), is measured when additionally to the E -field (E_x) a magnetic field (H_z) is applied perpendicularly, see Figure 1.2. Due to E_x there is a current j_x . In a Drude picture, this implies that charge $q = -e$ moves with a velocity $-v_x$. H_z forces the charge carriers in y -direction with the Lorentz force $\mathbf{F}_L = (-eE_x, -ev_x H_z, 0)$. Consequently, a charge imbalance builds up in y -direction, resulting in the so-called Hall electric field (E_y). In our example $E_y < 0$ points in the negative y -direction. The quantity that best characterizes the Hall effect, while being experimentally easy to access, is the Hall coefficient (R_H), defined as

$$R_H := \frac{E_y}{j_x H_z}. \quad (1.5)$$

1. Introduction

The Hall resistivity $\rho_H := E_y/j_x$ is consequently given as

$$\rho_H = R_H H_z. \quad (1.6)$$

In order to enable a theoretical discussion of the Hall coefficient, let us rewrite Equation (1.5) in terms of the conductivity tensor $\sigma_{\alpha\beta}$. Combining Equations (1.1) and (1.5), yields

$$R_H = \frac{-\sigma_{yx}}{\sigma_{xx}\sigma_{yy} - \sigma_{xy}\sigma_{yx}} \frac{1}{H_z}. \quad (1.7)$$

In a weak field limit, a response σ_{xy} can only be due to the applied magnetic field H_z . As a result the off-diagonal elements, σ_{xy} and σ_{yx} , are at least of linear order in H_z , while the diagonal elements, σ_{xx} and σ_{yy} , are of 0th order in H_z . This justifies further simplification, yielding³

$$\begin{aligned} R_H &= \frac{\sigma_{xy}}{\sigma_{xx}\sigma_{yy}} \frac{1}{1 - \frac{\sigma_{xy}\sigma_{yx}}{\sigma_{xx}\sigma_{yy}}} \frac{1}{H_z} \\ &= \frac{\sigma_{xy}}{\sigma_{xx}\sigma_{yy}} \frac{1}{H_z} + \mathcal{O}(H_z). \end{aligned} \quad (1.8)$$

Ultimately, by combining Equations (1.6) and (1.8), we obtain an expression for the Hall resistivity. Here we neglect quadratic and higher orders in H_z , and assume $\sigma_{xx} = \sigma_{yy}$, in order to yield

$$\rho_H \simeq \frac{\sigma_{xy}}{(\sigma_{xx})^2}. \quad (1.9)$$

The experimental results [1] we investigate in the present work were obtained by N. Barišić *et al.*. They carefully measured the DC resistivity and Hall coefficient of $\text{HgBa}_2\text{CuO}_{4+\delta}$. In Figure 1.3, their result is depicted for three exemplary samples.

The DC resistivity, $\rho \hat{=} \rho_{xx}$ in Equation (1.4), is shown in Figure 1.3 A and B as a function of temperature T and T^2 , respectively. We observe that, above the critical superconducting temperature T_c and below the optimal doping $\delta < \delta_{\text{opt}}$, a quadratic temperature dependence is obtained. It remains quadratic up to a temperature T^{**} . Note at this point, that T^{**} was also displayed in Figure 1.1, although we had not yet discussed its significance. Upon further increasing the temperature, the temperature dependence changes to behave linear above T^* . For temperatures $T^{**} < T < T^*$ the system features a crossover in terms of a mix of linear and quadratic temperature dependence. Hence,

$$T < T_c : \quad \rho = 0, \quad (1.10a)$$

$$T_c < T < T^{**} : \quad \rho \propto T^2, \quad (1.10b)$$

$$T^{**} < T < T^* : \quad \rho \propto aT + bT^2, \quad (1.10c)$$

$$T^* < T : \quad \rho \propto T. \quad (1.10d)$$

³ To get from the first to the second line the following considerations were applied: The factor $\frac{\sigma_{xy}\sigma_{yx}}{\sigma_{xx}\sigma_{yy}} \ll 1$ is small, since it is of order $\mathcal{O}(H_z^2)$. Thus $\left[1 - \frac{\sigma_{xy}\sigma_{yx}}{\sigma_{xx}\sigma_{yy}}\right]^{-1} = 1 + \mathcal{O}(H_z^2)$ is expanded by using $1/(1+x) = 1 + x + x^2 + \dots$

1. Introduction

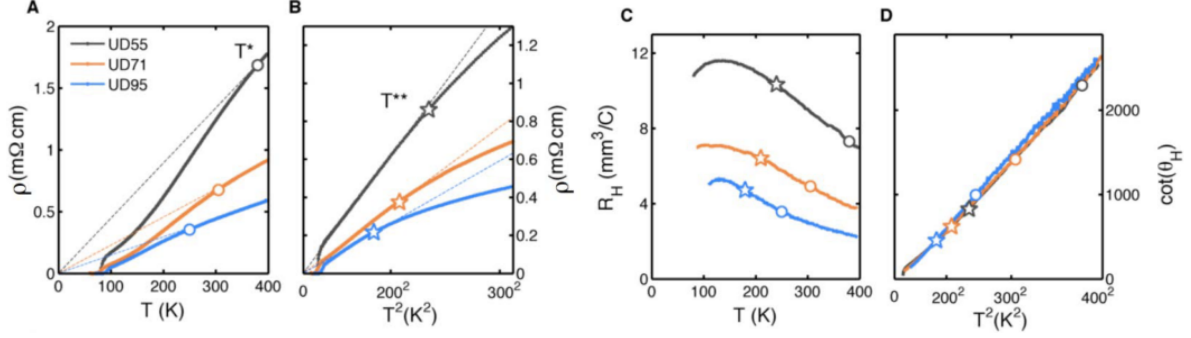


Figure 1.3.: Experimental results of in Hg1201. (A),(B) Temperature dependence of resistivity ρ , (C) the Hall coefficient as a function of temperature T , and (D) the cotangent of Hall angle $\cot(\theta_H) = \rho/\rho_H$ and a function T^2 . The data corresponds to three representative samples with $T_c = 55$ K, 71 K and 95 K, which reside within the underdoped region. The plot is taken from Ref. [1]

In Figure 1.3 C the Hall coefficient R_H , as in Equation (1.5), is shown. We observe $R_H > 0$ is positively valued, which suggests that holes are the effective charge carriers in the system. The significance of its temperature dependence becomes only apparent upon taking the ratio $\rho/\rho_H = \cot(\theta_H)$, where θ_H is the so-called Hall angle. In Figure 1.3 D, the measurement of $\cot(\theta_H)$ is shown as a function of T^2 . We observe that a quadratic temperature dependence is given across all temperature scales. And moreover all three samples universally align as one curve. We note,

$$T < T_c : \quad \rho/\rho_H = 0, \quad (1.11a)$$

$$T_c < T : \quad \rho/\rho_H \propto T^2. \quad (1.11b)$$

In Figure 1.4, the experimental result is summarized. Let us stress the great simplification this observation yields w.r.t. the rich phase diagram of cuprates. The experimental results pose an intriguing question to the theory: How can such an universal behaviour across the phase diagram of cuprates emerge? Different regimes are governed by fundamentally different scattering processes, yet the same temperature dependency of ρ/ρ_H is obtained at all doping levels and temperature scales. In the next section we will elaborate how we start to investigate this phenomenon.

1.3. Ansatz

Hitherto, we have familiarized the reader with cuprates and their rich phenomenology in Section 1.1. In Section 1.2, we highlighted novel experimental results by the group of N. Barišić et al. at TU Wien. The most striking observation is a universal⁴ temperature

⁴Compound independent and valid for different phases, including the pseudogap phase, strange metal phase and Fermi liquid phase.

1. Introduction

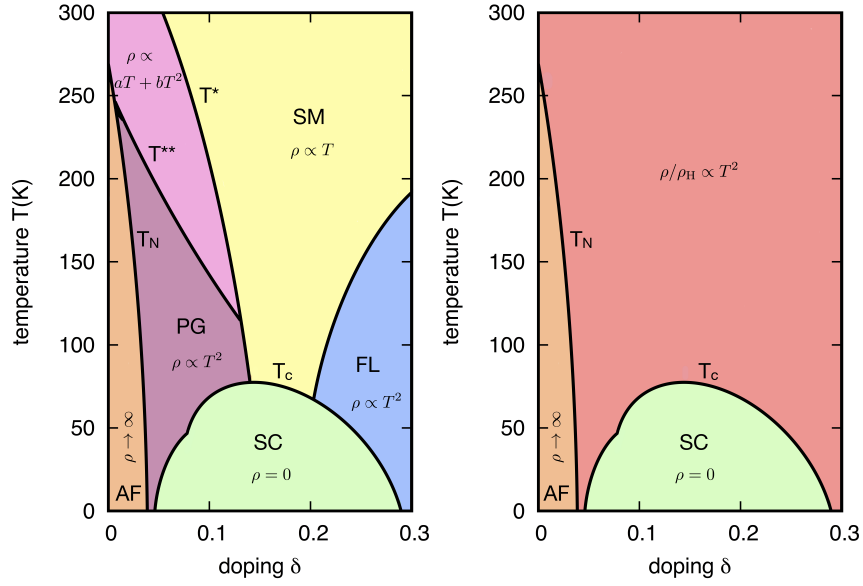


Figure 1.4.: The resistivity in a prototypical phase diagram of cuprates. The left panel shows the temperature dependence of the DC resistivity ρ , and the right panel juxtaposes the ratio of DC resistivity and Hall resistivity ρ/ρ_H . The phases shown are the antiferromagnetic insulator (AF), the superconducting dome (SC), a pseudogap region (PG), a strange metal phase (SM), as well as the Fermi liquid regime (FL) upon hole-doping δ . Figure is reproduced from Ref. [1].

1. Introduction

squared behaviour of the ration ρ/ρ_H , where ρ is the DC resistivity and ρ_H is the Hall resistivity.

A first crude explanation, given in the same experimental paper, is the following:

Within the simple effective-mass approximation that assumes a parabolic band,

$$\rho = m^*/(ne^2\tau) \quad (1.12)$$

and

$$R_H = 1/(ne), \quad (1.13)$$

where m^* is the effective mass and n is the carrier density, so that

$$\cot(\theta_H) = \rho/\rho_H \propto m^*/\tau \quad (1.14)$$

is independent of the carrier density and essentially a direct measure of the scattering rate $1/\tau$. [1]

This would suggest that the scattering rate has a T^2 -dependence consistent with Fermi liquid theory. Despite the beauty of this result and of its most natural interpretation, the approximation of a parabolic band and in particular the Drude model is a priori rather questionable for low-dimensional strongly correlated compounds such as cuprates.

In the scope of this thesis, we aim to understand how the ratio of ρ/ρ_H ought to be interpreted. Being at the same institute of TU Wien, where the measurements have been originally performed, we are highly motivated to gain a fundamental understanding.

From the theoretical point of view, as a first step, we need to define our model of choice for cuprates. Throughout the analysis we approach cuprates from the Mott insulator side. This approach was briefly compared to other perspectives in Section 1.1 and will be explained in more detail in Chapter 2. Before elaborating later on, let us state that, within the scope of this thesis, we model cuprates by a single band Hubbard model on a two dimensional square lattice with on-site Coulomb interaction and appropriate dispersion relation including nearest, next-nearest and next-next-nearest neighbor hopping.

As a next step, we solve the Hubbard model by state-of-the-art quantum many-body methods, such as the diagrammatic extensions to dynamical mean field theory, namely the dynamical vertex approximation (D Γ A) and the dual fermion (DF) theory.

Finally the data will be analyzed following two strategies:

- Extracting the scattering rate from the self-energy. We recall that the self-energy, in its most general form, is a momentum and frequency dependent correction of the dispersion relation, which accounts for temporal and spatial fluctuations due to electron-electron correlations. By evaluating the self-energy at the Fermi surface, we observe a small imaginary part, which is naturally interpreted as scattering rate. Here we follow the intriguing question, whether said scattering rate displays universal temperature dependence.

- Direct computation of the ratio ρ/ρ_H . The difficulty here is that even within the Kubo formalism the Hall conductivity, or rather the off-diagonal element of the conductivity tensor⁵ is diagrammatically speaking a three-particle vertex. The computation of such a vertex is currently not feasible in terms of numerical effort within DGA and DF. Therefore, we will aim to at least identify sufficient approximations, that potentially allow for both computation and physical interpretation.

The basic idea is to determine to what extent the methods employed and approximations applied are able or not able to capture and identify the physics observed in the experimental data. This will be crucial in understanding the scattering processes dominating the system and rejecting the theoretical paradigms not compatible with the new experimental evidence. These processes might result to be quite helpful to define the 'glue' that makes superconductivity in cuprates possible.

1.4. Outline

In Chapter 1, we have outlined the discovery of superconducting materials with a particular focus on cuprates. More specifically, in Section 1.1, we have highlighted some phenomenology that all compounds have in common. This is supported by Chapter D, where angle-resolved photoemission spectroscopy is briefly explained. In Section 1.2, we have turned towards the main motivation of our work by discussing novel experimental results obtained by the group of N. Barišić *et al.* at the institute of solid state physics at TU Wien. In Section 1.3, we propose our ansatz to theoretically investigate the physics underlying the experimental results.

In Chapter 2, we introduce the crystal structure of our physical system and the model we apply to describe it. In Section 2.1, we motivate the Hamiltonian of our model. In Section 2.3, the quantum field theoretical perspective is preceded, which is later exploited in order to explain the methods in Chapter 3. In Section 2.4, all parameters that define the model are stated. In particular, we illustrate the dispersion relation and show the non-interacting density of states.

In Chapter 3, the numerical methods are discussed. This chapter is split in three sections: Section 3.1 lays out the general idea of dynamical mean field theory (DMFT). Section 3.2 goes beyond DMFT by means of diagrammatic extensions such as the dynamical vertex approximation and the dual fermion theory on top of the local description of DMFT. Finally, in Section 3.3, we have briefly discussed the issue of analytic continuation and in particular the Padé approximation.

In Chapter 4, we present results for the scattering rate in cuprates by means of different quantum many-body approaches. Specifically, in Section 4.1, the temperature

⁵The conductivity tensor was introduced in Section 1.2. Within the Kubo formalism the conductivity tensor can be written as current-current correlation function.

1. Introduction

dependence of the scattering rate is extracted from single-particle quantities in DMFT, DΓA and DF. Secondly, in Section 4.2, some linear response theory expressions are proposed to be used within the previous schemes in order to make a more direct connection with the experiment by N. Barišić *et al.* .

In Chapter 5, we summarize the theoretical description emerging from current results and discuss possible future paths to circumvent the present drawbacks and gain a significantly improved theoretical understanding.

2. Model

In this chapter, we introduce our physical system and the model we apply to describe it. In Section 2.1, the crystal structure is shown and by physical arguments we motivate the Hamiltonian of our model. Subsequently, in Section 2.2, we place this model in the context of realistic material calculations and briefly compare it to possible alternative models.

In Section 2.3, we introduce the model from a quantum field theoretical perspective. This allows to introduce the formalism, which is later exploited in order to explain the methods in Chapter 3.

In Section 2.4, all parameters that define the model are stated. In particular, we illustrate the dispersion relation, as well as show the corresponding non-interacting density of states.

2.1. Intuitive picture

Cuprates, the class of materials subject to this work, consist of a layered structure of weakly coupled quasi two dimensional CuO_2 -planes. In Figure 2.1 (left), the crystal structure of an exemplary cuprate, namely $\text{HgBa}_2\text{CuO}_4$, is shown.

For an introduction on the classification of cuprates please refer to Ref. [15] or see Appendix A. In a nutshell, $\text{HgBa}_2\text{CuO}_{4+\delta}$ classifies as one of the mercury based compounds, belonging to the family of $\text{HgBa}_2\text{Ca}_{n-1}\text{Cu}_n\text{O}_{2n+2+\delta}$ ($\text{Hg}-12(n-1)n$), where n is the number of CuO_2 -planes per unit cell. In particular, $\text{HgBa}_2\text{CuO}_{4+\delta}$ is a single layer compound, and it is referred to as $\text{Hg}-1201$. Here, δ denotes the doping: In case of hole doping, this compound is annealed in oxygen atmosphere, which lets excess oxygen ions immigrate with concentration δ in the buffer layer $\text{Hg}-\text{O}_\delta$, not explicitly shown.¹

¹The position of the excess oxygen would be cubic centered between the top (bottom) Hg atoms in

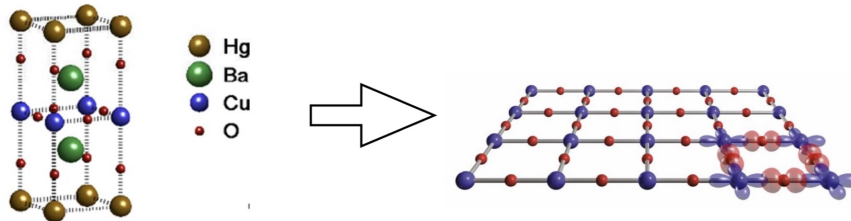


Figure 2.1.: (left) Structure of the parent compound $\text{HgBa}_2\text{CuO}_4$ [14]. (right) Isolated CuO_2 -planes.

2. Model

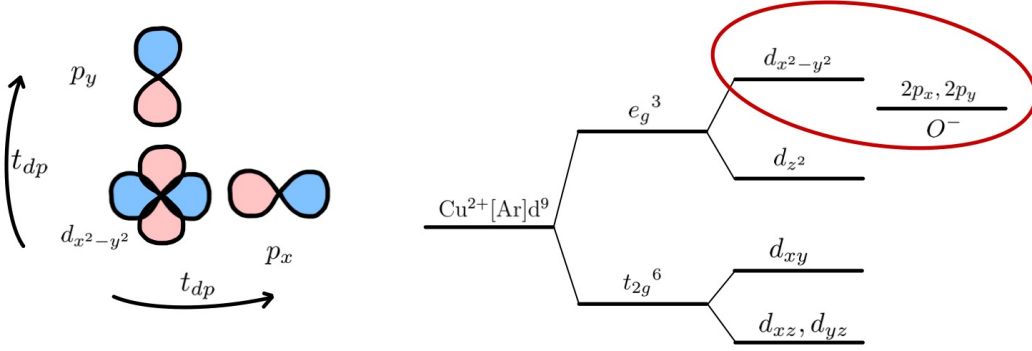


Figure 2.2.: (left) Cartoon of 3-band model. (right) Schematic CuO_2 energy splitting.

We present the specific case of Hg–1201 as exemplary cuprate, because it is the one mostly used in the experiment by N. Barišić *et al.* [1], which is of interest in the scope of this work. In particular, the experiment measured the temperature (T) dependence of the DC resistivity $\rho(T)$ and the Hall resistivity $\rho_H(T)$, see Section 1.2. As argued in Section 1.2, the universal T^2 -behaviour of the ratio ρ/ρ_H observed experimentally is compound and doping independent, as far as the currently available data allows to conclude. In fact, the models discussed are representative for single-layer cuprates in general.

The CuO_2 -planes depict in Figure 2.1 (right) are the key ingredient, that all cuprates have in common. Within the CuO_2 -planes, the copper appears in the form of positively charged ions, $\text{Cu}^{2+}[\text{Ar}]3d^9$. Hence, 9 electrons occupy 5 twofold spin-degenerate $3d$ -orbitals, giving rise to single occupation of the highest energy $3d$ -level. In particular, the cubic crystal field leads to an energy splitting into a triplet t_{2g}^6 and a higher energetic doublet e_g^3 , see Figure 2.2 (right). A further tetragonal crystal field splitting² yields one doublet d_{xz}, d_{yz} and 3 singlets $d_{xy}, d_{z^2}, d_{x^2-y^2}$; ordered by increasing energy. Hence, the $d_{x^2-y^2}$ remains single occupied.

In the undoped case, the single occupied $\text{Cu } 3d_{x^2-y^2}$ -orbitals build up a half-filled band crossing the Fermi surface. Furthermore, it is important to notice that, any orbital of the $3d$ shell ($n = 3, l = 2$), has a radial quantum number ($n - l + 1$) equal to 0. Thus, the radial wave function has *no* nodes. This leads to strong localization of the electrons, and as a result to stronger electronic correlation. In particular, the Coulomb repulsion of the electrons in this orbital is of the same order of magnitude as their kinetic energy.

As a result to the high localization in the $\text{Cu } 3d_{x^2-y^2}$ orbital state, the undoped, so-called *parent*, compound features an insulating, antiferromagnetic phase below the Néel temperature. This phase is due to the strong electronic correlations and hence unexpected in virtue of band theory, which predicts a conducting parent compound.

The simplest approach to explain this antiferromagnetic behaviour is to reduce the

¹Figure 2.1 (left). See also Figure A.1 in the Appendix.

²Depending on the compound and/or doping the additional field splitting can be due to tetragonal or orthorhombic crystal fields. In Hg–1201, one has a tetragonal crystal structure.

2. Model

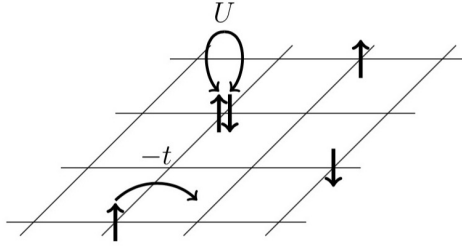


Figure 2.3.: The single band Hubbard model in two dimensions.

problem to the physics occurring within the strongly localized $\text{Cu } 3d_{x^2-y^2}$ -orbitals. The corresponding model is the *single band 2-dimensional Hubbard model* [16–18] on a square lattice. Figuratively, one may imagine electrons hopping, with probability amplitude $-t$, from one $\text{Cu } 3d_{x^2-y^2}$ -orbital state to another on a square lattice. When two electrons, of opposite spin, occupy the same lattice site, they pay a price in energy, the so-called Hubbard- U , due to Coulomb repulsion, see illustration in Figure 2.3. If the price is high enough, the electronic motion is suppressed, causing the system to be insulating. A preferred checkerboard ordering arising from a residual superexchange interaction between the spins also accounts for the antiferromagnetic instability at low temperature.

The Hamiltonian representing the above-mentioned single band 2-dimensional Hubbard model reads

$$H = - \sum_{\langle i,j \rangle, \sigma} t_{ij} \hat{c}_{i\sigma}^\dagger \hat{c}_{j\sigma} + U \sum_i \hat{c}_{i\uparrow}^\dagger \hat{c}_{i\downarrow}^\dagger \hat{c}_{i\downarrow} \hat{c}_{i\uparrow}, \quad (2.1)$$

where $\hat{c}_{i\sigma}^\dagger$ ($\hat{c}_{i\sigma}$) are electronic creation (annihilation) operators with spin $\sigma = \uparrow, \downarrow$ at site i , respectively. The first term represents the kinetic energy with hopping amplitude $-t_{ij}$ between nearest neighboring sites $\langle i, j \rangle$. While the second term corresponds to a static on-site Coulomb interaction of strength U in case of double occupation. The occupation of a site is given by $\hat{c}_{i\sigma}^\dagger \hat{c}_{i\sigma} = \hat{n}_{i\sigma}$.

This is the model we will employ throughout this work. The exact parameters applied are shown in Section 2.4. In the next section we will place this model in the context of realistic material calculations. The expert reader may skip the following section without missing essential details.

2.2. Viewpoint of realistic material calculations

The weary reader may ask: What about the oxygen? And how is the hopping parameter $-t$ and the Coulomb interaction U determined?

A complete discussion should start at the level of the *ab-initio* many-electron Hamiltonian of the material. If relativistic corrections are neglected, which is typically appropriate for $3d$ -oxides, and the Born-Oppenheimer [19] approximation is applied, this

2. Model

yields [20]

$$\begin{aligned}
 H = \sum_{\sigma} \int d^3r \hat{\Psi}^{\dagger}(\mathbf{r}, \sigma) & \left[-\frac{\hbar^2}{2m} \nabla^2 + \underbrace{\sum_l \frac{-e^2}{4\pi\epsilon_0} \frac{Z_l}{|\mathbf{r} - \mathbf{R}_l|}}_{\equiv V_{\text{ion}}(\mathbf{r})} \right] \hat{\Psi}^{\dagger}(\mathbf{r}, \sigma) \\
 + \frac{1}{2} \sum_{\sigma\sigma'} \int d^3r d^3r' & \hat{\Psi}^{\dagger}(\mathbf{r}, \sigma) \hat{\Psi}^{\dagger}(\mathbf{r}', \sigma') \underbrace{\frac{e^2}{4\pi\epsilon_0} \frac{1}{|\mathbf{r} - \mathbf{r}'|}}_{\equiv V_{ee}(\mathbf{r} - \mathbf{r}')} \hat{\Psi}(\mathbf{r}', \sigma') \hat{\Psi}(\mathbf{r}, \sigma), \quad (2.2)
 \end{aligned}$$

where $\hat{\Psi}(\mathbf{r}, \sigma)$ ($\hat{\Psi}^{\dagger}(\mathbf{r}, \sigma)$) create (annihilate) an electron with spin σ , charge $-e$ and mass m at position \mathbf{r} , \mathbf{R}_l is the position of an ion with charge $Z_l e$, ϵ_0 is the vacuum dielectric constant and \hbar the Planck constant. $V_{\text{ion}}(\mathbf{r})$ and $V_{ee}(\mathbf{r} - \mathbf{r}')$ correspond to the ionic lattice potential and the electron-electron interaction, respectively. As mentioned above, at this point, phonon corrections, i.e. the kinetic energy of the lattice ions, and relativistic corrections, e.g. spin-orbit coupling, have been neglected.

We recall, that density functional theory (DFT) treats the *ab-initio* Hamiltonian on the basis of the Hohenberg-Kohn theorem [21], which states that the ground state energy is an exact functional of the electronic density. This leads to a minimization principle, which can be rewritten in Kohn-Sham equations [22], shown below in Equation (2.4), by means of an auxiliary set of one-particle wave functions (φ_i) and eigenvalues (ϵ_i). The Kohn-Sham equations are basically one-particle Schrödinger equations, describing single electrons moving in a time-averaged, i.e. static mean, potential that effectively accounts for ionic, electronic density and exchange-correlation effects of the rest of the system. In fact, the latter is the actual unknown. It is a non-local exchange-correlation energy functional $E_{\text{xc}}[\rho]$, that bares all many-body difficulties and necessities of further approximation.

One unexpectedly good approximation for many materials is the local density approximation (LDA), where the exchange-correlation energy functional is replaced by a functional of the local density only. This yields the LDA Hamiltonian,

$$H^{\text{LDA}} = \sum_{\sigma} \int d^3r \hat{\Psi}^{\dagger}(\mathbf{r}, \sigma) \left[-\frac{\hbar^2}{2m} \nabla^2 + V_{\text{ion}}(\mathbf{r}) + \int d^3r' V_{ee}(\mathbf{r} - \mathbf{r}') + \frac{\partial E_{\text{xc}}^{\text{LDA}}(\rho(\mathbf{r}))}{\partial \rho(\mathbf{r})} \right] \hat{\Psi}(\mathbf{r}, \sigma). \quad (2.3)$$

In practice, the local density, that is the basis of the LDA exchange-correlation energy functional, is computed by means of a weakly correlated model, namely the jellium model. As a consequence, LDA can obtain good results for materials that exhibit weak electronic correlations, while it fails to accurately describe strongly correlated electron systems, such as the materials of our focus: the cuprates. [20]

Nevertheless, one can compute an approximate band-structure by means of LDA. This is done by interpreting the eigenvalues of the Kohn-Sham equations,

$$H^{\text{LDA}} \varphi_i = \epsilon_i \varphi_i, \quad (2.4)$$

2. Model

Model	Hamiltonian
Hubbard model	$H = \sum_{\mathbf{k}, \sigma} \epsilon_{\mathbf{k}} \hat{c}_{\mathbf{k}\sigma}^\dagger \hat{c}_{\mathbf{k}\sigma} + U \sum_i \hat{n}_{i,\uparrow} \hat{n}_{i,\downarrow}$
Extended Hubbard model	$H(\tau - \tau') = \sum_{\mathbf{k}, \sigma} \epsilon_{\mathbf{k}} \hat{c}_{\mathbf{k}\sigma}^\dagger(\tau) \delta(\tau - \tau') \hat{c}_{\mathbf{k}\sigma}(\tau') + \frac{1}{2} \sum_{q\sigma\sigma'} \hat{n}_\sigma(\tau) U(\tau - \tau') \hat{n}_{\sigma'}(\tau')$
<i>dp</i> -model	$H = \sum_{\substack{\mathbf{k}, \sigma, \\ l, m \in \{d, p_x, p_y\}}} h_{\mathbf{k}, l, m} \hat{c}_{l\mathbf{k}\sigma}^\dagger \hat{c}_{m\mathbf{k}\sigma}$ $+ U_{dd} \sum_i \hat{n}_{d,i\uparrow} \hat{n}_{d,i\downarrow} + U_{pp} \sum_j \hat{n}_{p,j\uparrow} \hat{n}_{p,j\downarrow} + U_{dp} \sum_{\langle ij \rangle \sigma \sigma'} \hat{n}_{d,i\sigma} \hat{n}_{p,j\sigma'}$

Table 2.1.: Three possibilities of a low-energy modelization of the cuprate physics.

as single particle energies. Note that this is a leap, as the Hohenberg-Kohn theorem is in principal only applicable to the ground state energy. Therefore, the LDA band-structure is assumed to be reliable only in the close vicinity of the Fermi surface and not for high energy excitations. The reader may refer to Ref. [23] for LDA band-structure calculations, that are specifically performed for Hg-1201.

Once the Kohn-Sham equations are solved, the wave functions $\hat{\Psi}(\mathbf{r}, \sigma)$ can be expanded in a sophisticatedly chosen basis set, e.g. O. K. Andersen's linearised muffin-tin orbital [24] (LMTO) basis or its N th order extensions [25] (NMTO).³ This gives direct access to interpret the LDA band-structure in terms of "atomic" orbitals. In the framework of an LDA band-structure calculation, O. K. Andersen *et al.* applied the LMTO downfolding technique to cuprates in 1995. They deduced an effective low-energy Hamiltonian, which consists of 8-bands [28].

In particular, the 8-bands are formed by copper and oxide-orbitals of the CuO_2 -planes, namely $\text{Cu } 3d_{x^2-y^2}$, $\text{O } 2p_x$, $\text{O } 2p_y$ and $\text{Cu } 4s$ with σ bonding character and $\text{Cu } 3d_{xz}$, $\text{Cu } 3d_{yz}$ and both $\text{O } 2p_z$ with π character. Such an 8-band Hamiltonian can be further reduced into effective 3 and 1-band Hamiltonians. The latter is shown to involve a dispersion relation, that must include at least next (t), 2nd next (t') and 3rd next (t'')

³ Another possibility is to expand in plane waves and subsequently perform a projection onto Wannier orbitals. [26, 27]

2. Model

nearest neighbor hopping, [28]

$$\begin{aligned} \epsilon_{\mathbf{k}} = & -2t [\cos(k_x) + \cos(k_y)] + 4t' \cos(k_x) \cos(k_y) - 2t'' [\cos(2k_x) + \cos(2k_y)] \\ & + 4t^{(3)} [\cos(k_x) \cos(2k_y) + \cos(2k_x) \cos(k_y)] + 4t^{(4)} \cos(2k_x) \cos(2k_y) \\ & - 2t^{(5)} [\cos(3k_x) + \cos(3k_y)] + \dots - 2t^{(9)} [\cos(4k_x) + \cos(4k_y)] + \dots, \end{aligned} \quad (2.5)$$

where $\epsilon_{\mathbf{k}}$ is the Fourier transform of t_{ij} , so that Equation (2.1) takes the form of the Hamiltonian in Table 2.1 (Hubbard model).

Moreover, the 3-band Hamiltonian includes hopping up to 2nd nearest neighbors between $\text{Cu } 3d_{x^2-y^2}$, $\text{O } 2p_x$ and $\text{O } 2p_y$, where the $\text{Cu } 4s$ is partly folded down to the oxygen orbitals. This gives rise to the following tight-binding Hamiltonian [29]

$$H_t = \sum_{\substack{\mathbf{k}, \sigma, \\ l, m \in \{d, p_x, p_y\}}} h_{\mathbf{k}, lm} \hat{c}_{l\mathbf{k}\sigma}^\dagger \hat{c}_{m\mathbf{k}\sigma}, \quad (2.6)$$

$$h_{\mathbf{k}, dd} = \epsilon_d + 2t_{dd} [\cos(k_x) + \cos(k_y)] + 4t'_{dd} \cos(k_x) \cos(k_y), \quad (2.7)$$

$$h_{\mathbf{k}, p_x p_x} = \epsilon_p + 2 [t'_{pp} \cos(k_x) + t''_{pp} \cos(k_y) + t'''_{pp} \cos(k_x) \cos(k_y)], \quad (2.8)$$

$$h_{\mathbf{k}, p_y p_y} = \epsilon_p + 2 [t'_{pp} \cos(k_y) + t''_{pp} \cos(k_x) + t'''_{pp} \cos(k_y) \cos(k_x)], \quad (2.9)$$

$$h_{\mathbf{k}, dp_x} = 2 ([t_{pd} + 2t'_{pd} \cos(k_y)] \sin(k_x/2) + [t''_{pd} + 2t'''_{pd} \cos(k_y)] \sin(3k_x/2)), \quad (2.10)$$

$$h_{\mathbf{k}, dp_y} = -2 ([t_{pd} + 2t'_{pd} \cos(k_x)] \sin(k_y/2) + [t''_{pd} + 2t'''_{pd} \cos(k_x)] \sin(3k_y/2)), \quad (2.11)$$

$$\begin{aligned} h_{\mathbf{k}, p_x p_y} = & -4 [t_{pp} \sin(k_x/2) \sin(k_y/2) \\ & + t''''_{pp} (\sin(3k_x/2) \sin(k_y/2) + \sin(3k_y/2) \sin(k_x/2))]. \end{aligned} \quad (2.12)$$

The inclusion of the $\text{Cu } 4s$ orbital and the well-founded choice of dispersion corresponds to an extended version of the 3-band tight-binding model originally suggested by Emery [30] in 1987. Thus, it is often referred to as Emery model.

Starting from these effective 1 and 3-band Hamiltonians, one can perform calculations using quantum many-body methods, such as e.g. dynamical mean-field theory (DMFT). This corresponds to performing a so-called LDA+DMFT [20] calculation. The latter treats an important part of electronic correlations, which are necessary to yield the antiferromagnetic insulating phase in the proximity of half-filling. More details on DMFT will be presented in Section 3.1.

LDA+DMFT has been applied to cuprates numerous times [31–38] in the literature. In comparison to experimental data this was successful concerning the optical properties and photoemission. However, by treating both, the extended Emery model and the less involved single-band model by the hands of LDA+DMFT, surprisingly the former was revealed less suitable results. [29, 38]

Hitherto in our discussion, we considered the Coulomb interaction to be on-site and strong only in the $\text{Cu } 3d_{x^2-y^2}$. In 2013, P. Hansmann *et al.* [29] showed that non-local Coulomb interactions U_{pd} between the $\text{Cu } 3d_{x^2-y^2}$ and $\text{O } 2p$ orbital are essential to the applicability of the extended Emery model. Here, although the radial wave function of the $\text{O } 2p$ orbital is nodeless, the intra-atomic interaction U_{pp} remains less important. This is due to the typical occupation of the $\text{O } 2p$ -bands, which is almost completely

2. Model

filled. Therefore, the corresponding spectral weight near the Fermi surface is small, or equally scattering is suppressed due to the lack of empty states.

The complete interaction of the dp -model [29]

$$H_U = U_{dd} \sum_i \hat{n}_{d,i\uparrow} \hat{n}_{d,i\downarrow} + U_{pp} \sum_j \hat{n}_{p,j\uparrow} \hat{n}_{p,j\downarrow} + U_{pd} \sum_{\langle ij \rangle \sigma \sigma'} \hat{n}_{d,i\sigma} \hat{n}_{p,j\sigma'}, \quad (2.13)$$

which should be complemented by Equation (2.6). Here i and j sum over all Cu and O sites, respectively. See also Table 2.1 (dp -model). The large U_{pd} is important within the DMFT calculation, as it allows for a self-consistent determination of the d - p level splitting, i.e. $\epsilon_d - \epsilon_p$. It generally stabilizes a charge-transfer insulating [39] phase in the undoped case.

The essential physics which is included by the dp -model, as opposed to the discussed single-band Hubbard model, are incommensurate charge-density waves (CDWs). These correspond to a broken translational and rotational symmetry via intra-unit cell charge stripe order. Incommensurate CDWs have been observed experimentally by X-ray diffraction [40–46], tunneling microscopy [47, 48] and nuclear magnetic resonance [49]. Recently, these have been suspected to be of crucial importance [40, 50–54] in the interplay with the emergence of superconductivity. Hence, in principle, it would be most interesting to treat the full dp -model. However, the computational effort that DMFT and its extensions acquire grows exponentially with the number of orbitals. The possibility to include non-local Coulomb interaction into an effective Hamiltonian has been investigated. A promising method to investigate this effective interaction is constrained random phase approximation [55] (cRPA). Here, the intra- and inter-atomic electronic screening effects of the O2 p -orbitals are treated on the RPA level, while an effective $U_{dd,\omega\mathbf{q}}^{\text{cRPA}}$ remains to be treated on a many-body level.

This leads the path towards the so-called extended Hubbard model, which is in the simplest way represented by the action⁴ [56]

$$\mathcal{S} = - \sum_{\mathbf{k}\sigma} \bar{c}_{\mathbf{k}\sigma} [i\nu - \epsilon_{\mathbf{k}}] c_{\mathbf{k}\sigma} + \frac{1}{2} \sum_{q\sigma\sigma'} U_q \rho_{q\sigma}^* \rho_{q\sigma'}, \quad (2.14)$$

$$\rho_{q\sigma} = \sum_{\mathbf{k}\sigma} [\bar{c}_{\mathbf{k}\sigma} c_{\mathbf{k}+\mathbf{q}\sigma} - \langle \bar{c}_{\mathbf{k}\sigma} c_{\mathbf{k}\sigma} \rangle \delta_{q0}]. \quad (2.15)$$

This problem can be solved similarly to DMFT in extended DMFT [57] (EDMFT) by mapping onto a local problem [51, 54]. The self-consistent treatment effectively solves a Hamiltonian containing a retarded interaction, which may be written as

$$H(\tau - \tau') = \sum_{\mathbf{k},\sigma} \epsilon_{\mathbf{k}} \hat{c}_{\mathbf{k}\sigma}^\dagger(\tau) \delta(\tau - \tau') \hat{c}_{\mathbf{k}\sigma}(\tau') + \frac{1}{2} \sum_{q\sigma\sigma'} \hat{n}_\sigma(\tau) U(\tau - \tau') \hat{n}_{\sigma'}(\tau'). \quad (2.16)$$

P. Werner *et al.* discussed [51] in 2014 the application of EDMFT to cuprates in the undoped case, i.e. at half-filling, for an effective one and three-band Hamiltonian by

⁴A proper introduction to the action formalism is provided in the subsequent section.

2. Model

treating p - p and p - d interactions on a Hartree level. The results for the single-particle spectral function showed good agreement with experimental values, however to the best of our knowledge, hitherto cuprates have not been studied for the doped case nor under consideration of momentum dependence. The implementation of such schemes are a matter of current effort.

All models we have discussed here are summarized in Table 2.1 ordered in terms of their computational effort. In the scope of this project, we restrict our-selves to the single-band Hubbard model with the parameters stated in the Section 2.4. The first question to be answered is whether the least demanding model suffices to explain the experimentally observed temperature dependency of the resistivity and Hall resistivity.

2.3. The Hubbard model in quantum field theory (QFT)

Up to this point, we have given an overlook of the phenomenology and modelization of cuprates. Due to the considerable broadness of the literature on the topic it was not possible to treat this in detail. However, in our discussion we basically arrived at a very simple model. In this section, the model shall be discussed from a quantum field theoretical perspective, where we will follow parts of [58] by N. E. Bickers.

The generating functional of a physical system at finite temperature can be written in terms of a thermal partition function

$$Z = \int_{\bar{c}c} e^{-S[\bar{c},c]}, \quad (2.17)$$

$$\mathcal{S} = \mathcal{S}_0 + \mathcal{S}_{\text{int}}, \quad (2.18)$$

where \mathcal{S} is the action, which consists of two parts: the non-interacting \mathcal{S}_0 and the interacting \mathcal{S}_{int} . $\int_{\bar{c}c}$ denotes the coherent-state path integral, which is derived and discussed in Appendix B.1 or in literature [59].

The Hubbard model is given by the following choice of action:

$$\mathcal{S}_0 = \bar{c}_{\sigma x} [\partial_\tau \delta_{\mathbf{x}\mathbf{x}'} + \delta_{\tau\tau'} (t_{\mathbf{x}\mathbf{x}'} - \mu \delta_{\mathbf{x}\mathbf{x}'})] c_{\sigma' \mathbf{x}'}, \quad (2.19)$$

$$\mathcal{S}_{\text{int}} = U n_{\uparrow x} n_{\downarrow x}. \quad (2.20)$$

At this point, repeated indices are summed over, or in case of continuous quantities integrated, with ⁵

$$\sum_x = \int_0^\beta d\tau \sum_{\mathbf{x}}, \quad (2.21)$$

where $it \rightarrow \tau \in [0, \beta]$ is the imaginary time that is generated by performing a so-called Wick rotation. β is the inverse temperature and the periodicity of the imaginary time.

⁵ Alternatively one could define $\mathcal{S} \rightarrow \beta \mathcal{S}$ and $\int d\tau \rightarrow \frac{1}{\beta} \int d\tau$

2. Model

The non-interacting system is described by \mathcal{S}_0 , where $\bar{c}_{\sigma x}$ ($c_{\sigma x}$) are Grassmann fields corresponding to electron creation and annihilation with spin σ at the space-time-point $x \equiv (\tau, \mathbf{x})$ and the dispersion relation shall enter through the hopping amplitude $t_{\mathbf{x}\mathbf{x}'}$.

The interacting part \mathcal{S}_{int} consists of a 4-point interaction $v(x - x')$, which could in general be non-local in space and time,

$$\mathcal{S}_{\text{int}} = \frac{1}{2} \bar{c}_{\sigma x} c_{\sigma x} v(x - x') \bar{c}_{\sigma' x'} c_{\sigma' x'}. \quad (2.22)$$

As argued in Section 2.1, within the simplest single-band Hubbard model the interaction v is an instantaneous, on-site Coulomb interaction due to the high localization of the Cu $3d_{x^2-y^2}$ -orbital. Hence, the Hubbard interaction term in Equation (2.20) can be derived from Equation (2.22) by setting

$$v(x - x') = U \delta_{\mathbf{x}\mathbf{x}'} \delta_{\tau\tau'} \delta_{\sigma-\sigma'}. \quad (2.23)$$

Finally, the definition of the field-density reads, $n_{\sigma x} = \bar{c}_{\sigma x} c_{\sigma x}$, without summation over repeated indices. The Hubbard action, hence, satisfies $SU(2)$ invariance as well as translational invariance in space and imaginary time.

This action is in general not solvable due to the non-Gaussian contributions in both real and momentum space in Equations (2.19) and (2.20), respectively. The solution of the non-interacting system can be obtained by performing a Fourier transformation with $k \equiv (i\nu, \mathbf{k})$

$$\mathcal{S}_0 = \bar{c}_{\sigma k} [-i\nu + (\epsilon_{\mathbf{k}} - \mu)] c_{\sigma k}, \quad (2.24)$$

where $\epsilon_{\mathbf{k}}$ is the dispersion relation and μ is the chemical potential. Note that, as is well-known [60], due to the periodic nature of the imaginary time τ the frequencies $i\nu$ are discrete. These so-called Matsubara frequencies will play an important role in later discussion. Equation (2.24) yields an exact expression for the bare one-particle Green's function⁶

$$G_{0,k} = \frac{1}{i\nu - (\epsilon_{\mathbf{k}} - \mu)}. \quad (2.25)$$

To solve the interacting problem one may follow many different approximation techniques, some of which will be discussed in the next chapter. The fundamental idea that underlies all of them is to find an effective action \mathcal{S}_{eff} of Gaussian form. The proposal translates in the most general form into the formulation [58] of a self-energy matrix $\Sigma_{\sigma\sigma'kk'}$,

$$\mathcal{S} = \mathcal{S}_{\text{SCF}} + \Delta\mathcal{S}, \quad (2.26)$$

$$\Delta\mathcal{S} \rightarrow 0, \quad (2.27)$$

$$\mathcal{S}_{\text{SCF}} = \mathcal{S}_0 + \bar{c}_{\sigma k} \Sigma_{\sigma\sigma'kk'} c_{\sigma' k'}, \quad (2.28)$$

⁶ Note that, the Green's function has a relative minus to the Feynman propagator in thermal QFT, as opposed to a relative imaginary unit in real time QFT.

2. Model

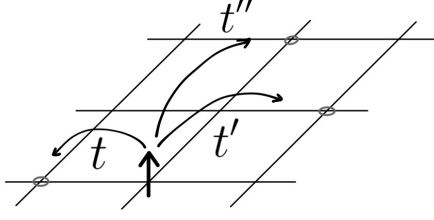


Figure 2.4.: The single band 2-dimensional Hubbard model.

where the label SCF refers to self-consistent field. In the scope of this work we will be interested in the diagonal part, which is referred to as self-energy $\Sigma_{\nu, \mathbf{k}}$

$$\Sigma_{\sigma\sigma', k k'} = \Sigma_{\sigma\sigma', k} \delta_{k k'}, \quad (2.29)$$

$$\Sigma_{\uparrow\uparrow, k} = \Sigma_{\downarrow\downarrow, k}. \quad (2.30)$$

The interacting one-particle Green's function is given as

$$G_{\mathbf{k}} = \frac{1}{i\nu - (\epsilon_{\mathbf{k}} - \mu) - \Sigma_{\mathbf{k}}}, \quad (2.31)$$

which is referred to as Dyson Equation.

2.4. Parameters to model cuprates

In the scope of this project, we employ the single-band Hubbard model as stated in Table 2.1 (Hubbard model),

$$H = \sum_{\mathbf{k}, \sigma} \epsilon_{\mathbf{k}} \hat{c}_{\mathbf{k}\sigma}^{\dagger} \hat{c}_{\mathbf{k}\sigma} + U \sum_i \hat{n}_{i, \uparrow} \hat{n}_{i, \downarrow},$$

where $\hat{c}_{\mathbf{k}\sigma}^{\dagger}$ ($\hat{c}_{\mathbf{k}\sigma}$) are electronic creation (annihilation) operators with spin $\sigma = \uparrow, \downarrow$ and momentum \mathbf{k} , $U = 2.5$ eV is a static on-site Coulomb interaction, $\hat{n}_{i, \sigma} = c_{i\sigma}^{\dagger} \hat{c}_{i\sigma}$ is the occupation operator at site i , while $\epsilon_{\mathbf{k}}$ is the associated band dispersion as in Equation (2.5),

$$\epsilon_{\mathbf{k}} = -2t [\cos(k_x) + \cos(k_y)] + 4t' \cos(k_x) \cos(k_y) - 2t'' [\cos(2k_x) + \cos(2k_y)].$$

Here, we consider the hopping on a two dimensional square lattice including next, 2nd next and 3rd next nearest neighbors: $t = 0.25$ eV, $t' = 0.05$ eV and $t'' = 0.025$ eV, as illustrated in Figure 2.4. These values have been used in previous studies [36] to successfully describe optical properties of Bi-based cuprates at different doping levels.

In Figure 2.5, displays the single-particle spectral function,

$$A^{\text{loc}}(\omega) = -\frac{1}{\pi} \text{Im} G_{\text{R}}^{\text{loc}}(\omega), \quad (2.32)$$

$$G_{\text{R}}^{\text{loc}}(\omega) = \sum_{\mathbf{k}} \frac{1}{\omega - \epsilon_{\mathbf{k}} + i\gamma}, \quad (2.33)$$

2. Model

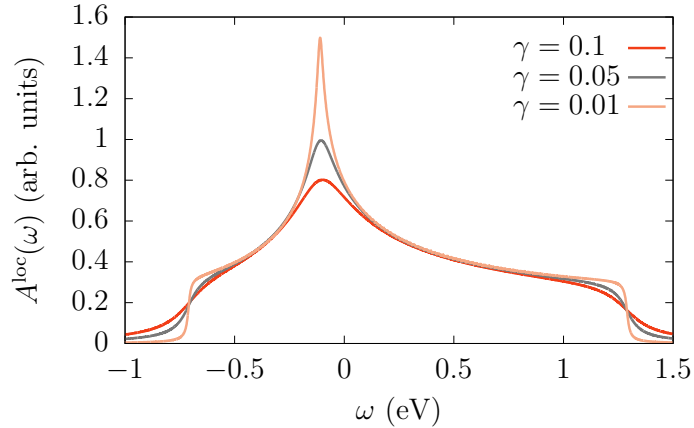


Figure 2.5.: The single-particle spectral function for the nearly non-interacting case.

where $\gamma = 0^+$ is a small artificial scattering rate. Note that particle-hole symmetry is broken by finite t' and t'' . Hence, the peak known as Van Hove singularity [35, 61] appears slightly below the chemical potential, i.e. below 0.

The focus of this project is to investigate the same parameter range as in the experiment by N. Barišić *et al.* [1]. In particular, we are interested in the so-called pseudo-gap and strange metal phases that emerge above the critical temperature of superconductivity, which is of the order of 70 K in the case of Hg-1201. In order to scan the phase diagram shown in Figure 1.1 on page 4, the doping δ and the temperature T are varied with the following values:

$$\begin{aligned}
 T(K) &= 77.37, 116.05, 145.06, 193.42, 232.10, 290.12, 386.83, 464.20 \text{ and } 580.25, \\
 \beta(\text{eV}^{-1}) &= 150, 100, 80, 60, 50, 40, 30, 25 \text{ and } 20, \\
 \delta &= 0.1, 0.15 \text{ and } 0.2.
 \end{aligned}
 \tag{2.34}$$

Here, β is the inverse temperature in eV, thus, the first two lines convey equal information. The highest temperatures are not of particular physical interest, but need to be chosen so that our numerical calculation, and in particular the DMFT(ED)⁷ part, undergoes proper annealing. The latter refers to the procedure of first computing the highest temperature for each doping and subsequently, stepwise reducing the temperature for each doping individual by using the result of the previous calculation as input for the new one at lower T .

⁷See Section 3.1.3.

3. Methods

In this chapter, we will review the methods, that we employ, to compute a solution for the single-band 2-dimensional Hubbard model, which represents our most basic description for the cuprate physics.

In Section 3.1, we introduce dynamical mean-field theory (DMFT), which is the state-of-the-art method to treat strongly correlated electron systems. This approach singles out one site on the lattice of the Hubbard model, where local Coulomb repulsion is present, and treats the rest as a self-consistently determined mean-field bath of non-interacting electrons.

Although DMFT is able to account for strong correlations in the system, it can only treat purely local correlations. In high-dimensional models this is a good approximation, because the momentum-dependence of correlations is negligible on the one particle level. However, the physics of cuprates is governed by their quasi two-dimensional copper-oxide-planes, cf. Section 2.1. As a consequence, cuprates show highly momentum-dependent scattering, as experimentally demonstrated, e.g. by angle-resolved photoemission spectroscopy (ARPES), see Chapter D. Therefore, for these systems, we can use DMFT as a mere starting point, at most.

The methods discussed in Section 3.2 include non-local fluctuations by means of diagrammatic extensions to DMFT. The formalism, that serves as a basis for these methods, is diagrammatics at the two particle level, which is introduced in Section 3.2.1. Thereupon, dynamical vertex approximation (D Γ A) and dual fermion (DF) theory are explained, in Section 3.2.2 and Section 3.2.3, respectively.

Ultimately, DMFT, D Γ A and DF enable us to compute the self-energy as a function of Matsubara frequencies, see Section 2.3. However crucially, in order to deduce physical information from the self-energy (or any observable of the system), they need to be given as a function of real frequencies.

In Section 3.3, we discuss, hence, the procedure of analytic continuation. In particular, the technique employed here is the Padé approximation, whose intrinsic strength and limitation will be illustrated in details.

3.1. Dynamical mean-field theory (DMFT)

Here, we provide a short introduction to dynamical mean-field theory (DMFT).

As a first step, we familiarize the reader with the Anderson impurity model (AIM) in Section 3.1.1. We then show how the Hubbard model is mapped onto the AIM, as illustrated in Figure 3.1. This is done in a self-consistency loop described in Section 3.1.2.

3. Methods

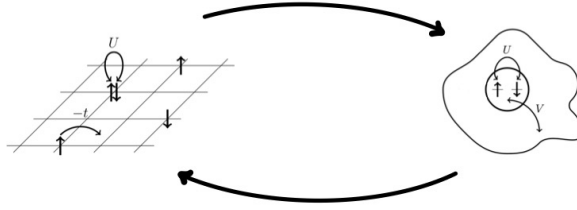


Figure 3.1.: Schematic DMFT loop.

In the course of the latter, the AIM must be solved by means of a so-called impurity solver. In Section 3.1.3, we elaborate on our choice for the impurity solver, namely exact diagonalization (ED).

3.1.1. Anderson impurity model (AIM)

The action of the AIM can be written as

$$\begin{aligned} \mathcal{S}_{\text{AIM}} = \sum_{\nu l \sigma} \left[\bar{b}_{l\sigma} (-i\nu + \varepsilon_l) b_{l\sigma} + [V_l \bar{b}_{l\sigma} c_\sigma + V_l^* \bar{c}_\sigma b_{l\sigma}] \right. \\ \left. + \bar{c}_\sigma (-i\nu - \mu) c_\sigma \right] + U \int_0^\beta d\tau n_\uparrow n_\downarrow, \end{aligned} \quad (3.1)$$

where $\bar{b}_{l\sigma}(b_{l\sigma})$ are fermionic Grassmann fields of a non-interacting bath with spin σ , on the energy level ε_l , $l \in [1, \infty]$. The fermionic fields $\bar{c}_\sigma(c_\sigma)$ describe an interacting impurity site, where double occupation costs energy U , similarly to the Hubbard model introduced in Section 2.1.¹ The impurity site hybridizes with the energy level² ε_l of the non-interacting bath via the probability amplitude $V_l(V_l^*)$.

As shown in Appendix B.3, the AIM action can be rewritten in terms of the hybridization function

$$\Delta_\nu = \sum_l \frac{|V_l|^2}{i\nu - \varepsilon_l} \quad (3.2)$$

$$= \int_{-\infty}^{+\infty} d\omega' \frac{\Delta(\omega')}{i\nu - \omega'}, \quad (3.3)$$

where $\Delta(\omega)$ is the bath density of states. This yields

$$\mathcal{S}_{\text{AIM}} = \sum_\nu \bar{c}_\sigma [-i\nu + (\Delta_\nu - \mu)] c_\sigma + U \int_0^\beta d\tau n_\uparrow n_\downarrow, \quad (3.4)$$

¹ Recall $n_\sigma = \bar{c}_\sigma(\tau) c_\sigma(\tau)$.

²The energy levels of the bath are often referred to as *bath sites*. This can be misleading: The AIM does not describe a cluster of sites with label l in real space. Instead, there are energy levels ε_l , where the impurity electron can jump to with probability amplitude V_l^* , or vice versa V_l .

3. Methods

comprising the expression for the exact solution of the bare Green's function of the AIM:

$$(\mathcal{G}_\nu)^{-1} = i\nu + \mu - \int_{-\infty}^{+\infty} d\omega' \frac{\Delta(\omega')}{i\nu - \omega'}. \quad (3.5)$$

The algorithms to solve the AIM, the so-called impurity solvers, represent a crucial part of the DMFT solution of the Hubbard model, introduced in Chapter 2. This will be further discussed in Section 3.1.3. Let us first see, however, how the Hubbard model can be mapped onto the AIM.

3.1.2. Self-consistency loop

The underlying theory of the self-consistency loop discussed in this section is dynamical mean-field theory (DMFT). Within DMFT, a lattice model (here: Hubbard model) is iteratively mapped onto an impurity model (here: AIM) through an iterative determination of its electronic bath. For a comprehensive review on the topic we refer the reader e.g. to A. Georges' *et al.* review. [62]

In a nutshell, DMFT can be understood as a self-consistency loop, where the momentum degrees of freedom are treated on a mean-field level, while all temporal and local quantum fluctuations are treated exactly. As a result the self-energy, see Equation (2.31) and above, is local by construction: Σ_ν^{loc} .

The self-consistency loop employed for DMFT can be written as follows:

$$\text{Input starting guess : } \Sigma_\nu^{\text{loc}} \quad , \text{ e.g. } \Sigma_\nu^{\text{loc}} = 0,$$

$$G_{\mathbf{k}\nu}^{\text{loc}} = [i\nu - (\epsilon_{\mathbf{k}} - \mu) - \Sigma_\nu^{\text{loc}}]^{-1}, \quad (3.6a)$$

$$G_\nu^{\text{loc}} = \sum_{\mathbf{k}} G_{\mathbf{k}\nu}^{\text{loc}}, \quad (3.6b)$$

$$(\mathcal{G}_\nu)^{-1} = (G_\nu^{\text{loc}})^{-1} + \Sigma_\nu^{\text{loc}}, \quad (3.6c)$$

$$\text{Impurity solver : } \text{in : } \mathcal{G}_\nu \quad \text{out : } G_\nu^{\text{AIM}} = G_\nu^{\text{loc}},$$

$$\Sigma_\nu^{\text{loc}} = (\mathcal{G}_\nu)^{-1} - (G_\nu^{\text{loc}})^{-1}, \quad (3.6d)$$

where $G_{\mathbf{k}\nu}^{\text{loc}}$ is the DMFT lattice Green's function computed in Equation (3.6a) from the *local* self-energy and the lattice dispersion $\epsilon_{\mathbf{k}}$. The *first DMFT self-consistency equation* is Equation (3.6b), where the local Green's function is computed by summing over all momenta. The *second DMFT self-consistency Equation* is the so-called Dyson Equation, appearing in Equations (3.6a), (3.6c) and (3.6d). As shown in Section 3.1.1, the AIM is fully defined by the choice of \mathcal{G} . Here, we assume that we have an impurity solver that solves the interacting problem stated in Equation (3.4). This loop is iterated from Equations (3.6a) to (3.6d) until a converged solution for Σ_ν^{loc} is found.

3. Methods

The impurity solver. There exists not one, but many possible impurity solvers including, e.g., exact diagonalization (ED) schemes, continuous time quantum Monte Carlo (CT-QMC) algorithms, numerical renormalization group (NRG), density matrix renormalization group (DMRG), as well as semi-analytic expressions, such as iterated perturbation theory (IPT). The choice of the impurity solver depends on many criteria. To name a few:

1. The lattice model of choice.
2. The parameter regime dictated by the problem under investigation. This refers to the range of e.g. temperature, interaction, doping and other parameters.
3. The additional approximations, that every impurity solver inevitably implies.
4. The computational effort the impurity solver demands.

Let us deduce which impurity solver is suitable for our purpose:

Ad point 1, the choice of our model has been thoroughly discussed in Chapter 2. The Hubbard model does not allow for a fully analytic expression as an 'impurity solver', unlike the Falicov-Kimball model or the Binary Disorder model, to name counterexamples. The semi-analytic technique IPT is a qualitatively good interpolation between the two limiting cases, i.e. the non-interacting limit $U = 0$ and the atomic limit $U \gg t$, of the Hubbard model. However, quantitatively it is not precise, e.g. the Mott-Hubbard metal-insulator transition appears shifted, especially in the case of finite doping.

Ad point 2, the temperature regime we are interested in is determined by the occurrence of the pseudogap phase in cuprates above the superconducting dome. As seen in Figure 1.1 on page 4, this ranges from about 70 K to 300 K. Thus, techniques only suitable for zero or extremely low temperatures, such as DMRG and NRG, are excluded.

We hence narrowed the choice down to ED or CT-QMC. Both are suitable to compute a solution for the proposed AIM and both are feasible options considering the computational effort, mentioned in point 4.

Additionally, we need to consider the availability of a program and the expertise. Within the groups at the solid states institute at TU Wien, there are currently two programs frequently used: One that contains a standard ED algorithm and the *w2dynamics*-package [63–65], which is a CT-QMC solver in the hybridization expansion.

To adequately discuss point 3 goes beyond the scope here. Nonetheless, we mention that ED acquires a systematic error from the discretization of the bath density of states, while CT-QMC is afflicted with statistic errors. The latter was problematic for the first implementations of dynamical vertex approximation, which will be used in the course of this work, due to oscillations in the high-frequency regime of observables.³

Therefore, in the scope of this work, DMFT results have been obtained by exploiting an ED algorithm, while benchmarking sample cases with CT-QMC.

³These oscillations are particularly pronounced at the two particle level, which is the corner stone of DFA. However, this is not to say, that CT-QMC and DFA mutually exclude each other. On the contrary, important progress [66] has been recently achieved on CT-QMC and implementing DFA in the *w2dynamics* package is a matter of current effort.

3. Methods

In the following section, we will continue by specifically describing the ED algorithm.

3.1.3. Exact Diagonalization (ED)

In the previous section, we have illustrated how the Hubbard model is mapped onto the AIM by means of a self-consistency loop. The last missing ingredient, to compute the self-energy in Equation (3.6d) by means of this iterative method, is the impurity solver.

In the following, the ED algorithm employed in this work and its approximations are described. The approach was first reported in 1994 [67] by M. Caffarel and W. Krauth. Moreover, it is comprehensively reviewed [62] by A. Georges *et al.*, where i.a. ED is compared to CT-QMC.

The basic idea behind ED algorithms is to approximate the bath by a finite, discrete set of Anderson parameters $\{|V_l|, \epsilon_l\}$. The number of energy levels is fixed to a given number⁴ n_s , which is typically ≤ 8 . The bare Green's function in Equation (3.6c) is hence projected to the discrete version of Equation (3.5), namely

$$(\mathcal{G}_\nu^{n_s})^{-1} = i\nu + \mu - \sum_{l=2}^{n_s} \frac{|V_l|^2}{i\nu - \epsilon_l}. \quad (3.7)$$

The projection, this implies, requires the definition of a distance between \mathcal{G} and \mathcal{G}^{n_s} , which is subsequently minimized. In the code, that we employ, the distance is defined as

$$d = \frac{1}{N+1} \sum_{n=0}^N \frac{|\mathcal{G}_{\nu_n} - \mathcal{G}_{\nu_n}^{n_s}|}{n+1} \quad (3.8)$$

The minimization of this function yields a set of Anderson parameters $\{|V_l|, \epsilon_l\}$.

The Anderson parameters define a discrete AIM Hamiltonian⁵

$$H_{\text{AIM}}^{n_s} = \sum_{l=1, \sigma}^{n_s} \left[\epsilon_l \hat{b}_{l\sigma}^\dagger \hat{b}_{l\sigma} + V_l \hat{b}_{l\sigma}^\dagger \hat{b}_{1\sigma} + V_l^* \hat{b}_{1\sigma}^\dagger \hat{b}_{l\sigma} \right] + U \hat{n}_{1\uparrow} \hat{n}_{1\downarrow}, \quad (3.9a)$$

$$\epsilon_1 = \mu, \quad V_1 = 0, \quad \hat{n}_{1\sigma} = \hat{b}_{1\sigma}^\dagger \hat{b}_{1\sigma}, \quad (3.9b)$$

where the 1st energy level $l = 1$ corresponds to the interacting impurity site. This Hamiltonian is defined in a finite-dimensional Hilbert space, which is spanned by

$$|N_{1\uparrow}, N_{2\uparrow}, \dots, N_{n_s\uparrow}\rangle \otimes |N_{1\downarrow}, N_{2\downarrow}, \dots, N_{n_s\downarrow}\rangle, \quad (3.10)$$

where $N_{l\sigma} = 0, 1$. As a next step, the Hamiltonian is diagonalized, yielding a numerically exact set of eigenstates $|i\rangle$ with eigenvalues E_i .

⁴The number of energy levels n_s includes the impurity site itself as 1st level. Therefore, the sum over l in Equation (3.7) starts at $l = 2$, summing only over the bath states.

⁵Cf. the AIM action in Equation (3.4): Here, the Hamiltonian is written in fermionic operators instead of Grassmann fields. Note that, we set $\hat{c}_\sigma^{(\dagger)} \equiv \hat{b}_{1\sigma}^{(\dagger)}$.

3. Methods

As shown in Section B.4, the AIM one-particle Green's function in its spectral representation, also called Lehmann representation [60], is given as

$$G_{\nu}^{\text{AIM}} = -\frac{1}{Z} \sum_{i,m} \frac{|\langle m | \hat{c}_{\sigma}^{\dagger} | i \rangle|^2}{E_i - E_m - i\nu} (e^{-\beta E_i} + e^{-\beta E_m}). \quad (3.11)$$

This can be explicitly computed by means of the set of eigenstates known from exact diagonalization of the Hamiltonian in Equation (3.9), and consequently the self-energy in Equation (3.6d) can be calculated.

With this procedure at hand, the self-consistency loop in Equations (3.6a) to (3.6d) can be iterated until a converged solution is found. The condition, under which a solution is considered converged, can be chosen in terms of $\Sigma_{\nu}^{\text{loc}}$, G_{ν}^{loc} or in the case of ED, most straight-forwardly, in terms of the Anderson parameters. In particular, we assume a solution to be converged when the set $\{|V_l|, \varepsilon_l\}$ remain unchanged within an absolute tolerance of 10^{-13} .

In conclusion, the ED impurity solver consists of three steps:

- Determine a set of Anderson parameters by minimization of Equation (3.8).
- Determine a set of eigenstates and eigenvalues by numerically exact diagonalization of the Hamiltonian in Equation (3.9).
- Compute the AIM one-particle Green's function, given in Equation (3.11).

3.2. Diagrammatic extensions to DMFT

In this section, we revise two ways of going beyond dynamical mean-field theory (DMFT). The fundament of this discussion remains DMFT, which has been reviewed in Section 3.1.

In Section 3.2.1, we recall the structure of diagrammatics at the two-particle level.

With the latter at hand, the so-called dynamical vertex approximation (DΓA) is described for our application, in Section 3.2.2. In particular, this corresponds to ladder DΓA in the particle-hole channel on top of ED as it is currently implemented.

Subsequently, in Section 3.2.3, the theory of dual fermions (DF) is revised.

Fundamentally, both, ladder DΓA and DF, aim to include long-range correlation effects, which are caused by collective excitations of the system. These are precursors of a phase transition and emerge when the corresponding fluctuations get strong, i.e. the correlation length of the associated susceptibility diverges. DΓA and DF are two examples of a larger group of methods recently reviewed [56] by G. Rohringer *et al.*. All of these methods have two basic steps in common:

- A non-perturbative building block is chosen amongst the two particle vertices and approximated to be local.
- A diagrammatic scheme is built around that building block to obtain a non-local self-energy, i.e. include non-local correlations beyond DMFT.

3. Methods

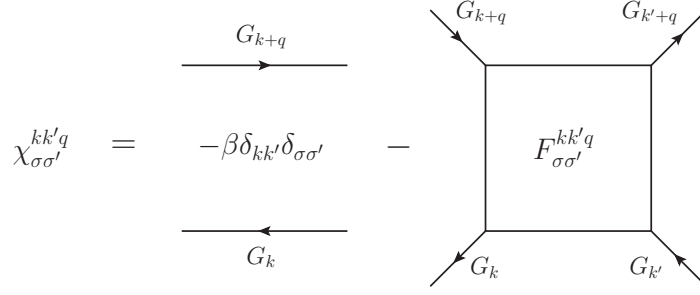


Figure 3.2.: Generalized susceptibility from Ref. [56].

The following discussion mostly follows [56] G. Rohringer *et al.*, while further details on the two-particle vertex can be found in Ref. [68].

3.2.1. Diagrammatics at the two particle level

The two-particle Green's function,

$$G_{\sigma\sigma',\mathbf{k}\mathbf{k}'\mathbf{q}}^{(2)}(\tau_1, \tau_2, \tau_3) \equiv \langle \mathcal{T}_\tau \left[\hat{c}_{\mathbf{k}\sigma}(\tau_1) \hat{c}_{\mathbf{k}+\mathbf{q},\sigma}^\dagger(\tau_2) \hat{c}_{\mathbf{k}'+\mathbf{q},\sigma'}(\tau_3) \hat{c}_{\mathbf{k}'\sigma'}^\dagger(0) \right] \rangle, \quad (3.12)$$

$$G_{\sigma\sigma',\mathbf{k}\mathbf{k}'\mathbf{q}}^{(2),\nu\nu'\omega} = \int_0^\beta d\tau_1 d\tau_2 d\tau_3 e^{i\nu\tau_1} e^{-i(\nu+\omega)\tau_2} e^{i(\nu'+\omega)\tau_3} G_{\sigma\sigma',\mathbf{k}\mathbf{k}'\mathbf{q}}^{(2)}(\tau_1, \tau_2, \tau_3), \quad (3.13)$$

in particle-hole representation describes the propagation of a particle-hole pair through the system. Note, however, that both, particle-hole and particle-particle propagators, can be extracted from this representation: A mere shift of the form $q_{pp} = q + k + k'$ recovers the process of two particles propagating. Equation (3.12) is the special case of $n = 2$ for the n -particle Green's function shown in Section C.2. Here, ν (ν') and \mathbf{k} (\mathbf{k}') are fermionic Matsubara frequencies and momenta, respectively, while ω and \mathbf{q} are bosonic.

By considering Wick's theorem [59], the two-particle Green's function consists of two disconnected parts and one connected part. Subtracting one of the disconnected parts, namely the cross-connected, defines the generalized susceptibility [68] (Figure 3.2)

$$\chi_{\sigma\sigma',\mathbf{k}\mathbf{k}'\mathbf{q}}^{\nu\nu'\omega} = G_{\sigma\sigma',\mathbf{k}\mathbf{k}'\mathbf{q}}^{(2),\nu\nu'\omega} - \beta G_k G_{k'} \delta_{q0}, \quad (3.14a)$$

$$= \underbrace{-\beta G_k G_{k+q} \delta_{kk'} \delta_{\sigma\sigma'}}_{\chi_{0,\mathbf{k}\mathbf{k}'\mathbf{q}}^{\nu\nu'\omega}} - G_k G_{k+q} F_{\sigma\sigma'}^{kk'q} G_{k'+q} G_{k'}, \quad (3.14b)$$

which is often used in computations, instead of the two-particle Green's function. In the second line we have additionally introduced the full vertex function $F_{\sigma\sigma'}^{kk'q}$, that accounts for all scattering events at the two-particle level. The lowest order of F is the bare interaction [69], $F_{\sigma\sigma'}^{kk'q} = U \delta_{\uparrow\downarrow}$. Furthermore, we defined the bare generalized susceptibility $\chi_{0,\mathbf{k}\mathbf{k}'\mathbf{q}}^{\nu\nu'\omega}$.

3. Methods

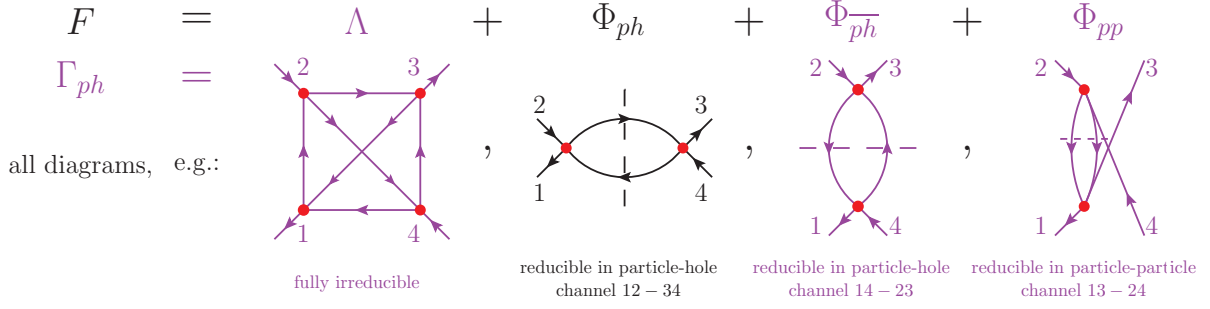


Figure 3.3.: Parquet decomposition from Ref. [56].

Choosing a particular linear combination of spin indices, allows the extraction of the physical charge (c) and spin (s) susceptibility⁶ by summation over all fermionic degrees of freedom

$$\chi_{c/s, \mathbf{k}\mathbf{k}'\mathbf{q}}^{\nu\nu'\omega} = \chi_{\uparrow\uparrow, \mathbf{k}\mathbf{k}'\mathbf{q}}^{\nu\nu'\omega} \pm \chi_{\uparrow\downarrow, \mathbf{k}\mathbf{k}'\mathbf{q}}^{\nu\nu'\omega}, \quad (3.15a)$$

$$\chi_{r, \mathbf{q}}^{\omega} = \sum_{\mathbf{k}, \mathbf{k}'} \chi_{r, \mathbf{k}\mathbf{k}'\mathbf{q}}^{\nu\nu'\omega}, \quad \text{with } r = c, s. \quad (3.15b)$$

In the particle-particle scattering representation, additionally the spin-singlet and triplet susceptibility can be defined.

Expanding the idea of one-particle irreducibility (1PI) one obtains three possibilities of two-particle irreducibility (2PI): particle-hole (ph), particle-hole transverse (\overline{ph}) and particle-particle (pp) depending on the lines that enable the separation of the corresponding diagrams. The parquet equations [58, 70], (Figure 3.3)

$$F_r^{kk'q} = \Lambda_r^{kk'q} + \Phi_{ph, r}^{kk'q} + \Phi_{\overline{ph}, r}^{kk'q} + \Phi_{pp, r}^{kk'q}, \quad (3.16a)$$

$$F_r^{kk'q} = \Gamma_{l, r}^{kk'q} + \Phi_{l, r}^{kk'q}, \quad \text{with } l = ph, \overline{ph}, pp, \quad (3.16b)$$

are then nothing more than a classification of diagrams in terms of there two-particle irreducibility. The full vertex F is decomposed into 2PI vertex functions $\Gamma_{l, r}^{kk'q}$ and their counter-parts $\Phi_{l, r}^{kk'q}$, the two-particle reducible vertices, as well as in $\Lambda_r^{kk'q}$, which is fully irreducible on the two-particle level, i.e. 2PI in all channels. The specific channel is denoted by the label $l = ph, \overline{ph}, pp$.

The full vertex F can be expressed by means of the Bethe-Salpeter Equations, e.g. for $l = ph$, it reads [58]

$$F_r^{kk'q} = \Gamma_{ph, r}^{kk'q} + \frac{1}{\beta} \sum_{k_1} \Gamma_{ph, r}^{kk_1q} G_{k_1} G_{k_1+q} F_r^{kk_1q}, \quad (3.17a)$$

$$\chi_r^{kk'q} = \chi_0^{kk'q} - \frac{1}{\beta^2} \sum_{k_1 k_2} \chi_0^{kk_1q} \Gamma_{ph, r}^{k_1 k_2 q} \chi_r^{k_2 k'q}. \quad (3.17b)$$

⁶These correspond to density and magnetic fluctuations, respectively.

3. Methods

Here, the second line refers to an equivalent formulation in terms of susceptibilities.

Finally, the Heisenberg equation of motion gives rise to the Schwinger-Dyson equation [60]

$$\Sigma_k = \frac{Un}{2} - \frac{U}{\beta^2} \sum_{k'q} F_{\uparrow\downarrow}^{kk'q} G_{k'} G_{k'+q} G_{k+q}. \quad (3.18)$$

Hence, the knowledge of the full two-particle vertex function F , through the Schwinger-Dyson equation, allows to compute the 1PI vertex, which is the one-particle quantity called the self-energy.

3.2.2. Dynamical vertex approximation (D Γ A)

In the following, we will revise the specific algorithm actually used to obtain our results. This, in fact, corresponds to a particular type of D Γ A, coined *ladder* D Γ A. For a full presentation of the D Γ A method, we refer the reader to the recent review [56] on diagrammatic extensions by G. Rohringer *et al.*, the PhD thesis by T. Schäfer [71], as well as the PhD thesis by G. Rohringer [69], or the pioneering works [72, 73] by A. Toschi, A. A. Katanin and K. Held.

The starting point for ladder D Γ A is a converged DMFT calculation. From the known set of eigenstates and eigenvalues obtained, e.g. by the exact diagonalization method any observable can be computed given its spectral representation. The DMFT loop requires the computation of the AIM one-particle Green's function, G_ν^{AIM} as given in Equation (3.11). The *bare*⁷ generalized susceptibility of the AIM is immediately accessible through

$$\chi_0^{\text{AIM},\nu\nu'\omega} = -\beta G_\nu^{\text{AIM}} G_{\nu+\omega}^{\text{AIM}} \delta_{\nu\nu'}. \quad (3.19)$$

Similarly, the AIM generalized susceptibility is computed by means of its Lehmann representation, which reads in its particle-hole representation [72]

$$\chi_{\sigma\sigma'}^{\text{AIM},\nu\nu'\omega} = \frac{1}{Z} (\chi_{123}^{\text{AIM}} + \chi_{132}^{\text{AIM}} + \chi_{312}^{\text{AIM}} + \chi_{213}^{\text{AIM}} + \chi_{231}^{\text{AIM}} + \chi_{321}^{\text{AIM}}), \quad (3.20a)$$

$$\chi_{123}^{\text{AIM}} = -\frac{1}{\beta^2} \sum_{m,n,i,j} \frac{\langle n|\hat{c}_\sigma^\dagger|m\rangle\langle m|\hat{c}_\sigma|i\rangle\langle i|\hat{c}_{\sigma'}^\dagger|j\rangle\langle j|\hat{c}_{\sigma'}|n\rangle}{i(\nu'+\omega) - E_i + E_j} \left[\frac{1}{i(\nu-\nu') + E_m - E_j} \left(\frac{e^{-\beta E_n} + e^{-\beta E_j}}{i\nu' + E_n - E_j} - \frac{e^{-\beta E_m} + e^{-\beta E_n}}{i\nu + E_n - E_m} \right) - \frac{1}{i(\nu+\omega) + E_m - E_i} \left(\frac{e^{-\beta E_i} - e^{-\beta E_n}}{i\omega + E_n - E_i} - \frac{e^{-\beta E_m} + e^{-\beta E_n}}{i\nu + E_n - E_m} \right) \right], \quad (3.20b)$$

$$\chi_{132}^{\text{AIM}} = \dots, \quad (\text{see Toschi } et al., (2007) [72] \text{ for all expressions}). \quad (3.20c)$$

The AIM generalized susceptibility contains all two-particle scattering effects, where correlation is local. When combined with G_ν^{AIM} , χ^{AIM} is used to obtain the local full

⁷Note, that the full Green's function is used to compute the bare generalized susceptibility. Here, bare refers to the fact, that the corresponding diagrams are not connected, as seen in Equation (3.14b).

3. Methods

vertex F_{loc} by means of

$$F_{\text{loc},\sigma\sigma'}^{\nu\nu'\omega} = -G_{\nu}^{\text{AIM}-1} G_{\nu'+\omega}^{\text{AIM}-1} \left[\chi_{\sigma\sigma'}^{\text{AIM},\nu\nu'\omega} - \chi_0^{\text{AIM},\nu\nu'\omega} \right] G_{\nu'+\omega}^{\text{AIM}-1} G_{\nu'}^{\text{AIM}-1}, \quad (3.21a)$$

$$F_{\text{loc},c/s}^{\nu\nu'\omega} = F_{\text{loc},\uparrow\uparrow}^{\nu\nu'\omega} \pm F_{\text{loc},\uparrow\downarrow}^{\nu\nu'\omega}, \quad (3.21b)$$

where again c and s label charge and spin, respectively.

The 2PI vertex Γ can be computed via matrix inversion in $\nu\nu'$ by means of the 'inverse' Bethe-Salpeter equation. In the case of the charge and spin susceptibility, with Equation (3.17b), this reads

$$\Gamma_{c/s}^{\text{loc},\nu\nu'\omega} = \beta^2 \left(\left[\chi_{c/s}^{\text{AIM},\nu\nu'\omega} \right]^{-1} - \left[\chi_0^{\text{AIM},\nu\nu'\omega} \right]^{-1} \right). \quad (3.22)$$

In the next step, the non-local bare DMFT susceptibility is computed via the DMFT lattice Green's function, Equation (3.6a),

$$\chi_0^{\text{loc},kk'q} = -\beta G_k^{\text{loc}} G_{k+q}^{\text{loc}} \delta_{kk'}, \quad (3.23a)$$

$$\text{with } G_k^{\text{loc}} = [i\nu - (\epsilon_{\mathbf{k}} - \mu) - \Sigma_{\nu}^{\text{loc}}]^{-1}. \quad (3.23b)$$

Here, the label loc refers to the inclusion of *exclusively* local correlations through the local self-energy of DMFT, although χ_0^{loc} is obviously \mathbf{k} -dependent as opposed to χ_0^{AIM} .

The quantities, given in Equation (3.22) and Equation (3.23), enable us to compute an auxiliary susceptibility (Ref. [71] Equation (2.47))

$$\chi_{r=c/s}^{*,\nu\nu'q} = \left[\left(\sum_{\mathbf{k}\mathbf{k}'} \chi_0^{\text{loc},kk'q} \right)^{-1} + \frac{1}{\beta^2} \left(\Gamma_r^{\text{loc},\nu\nu'\omega} - U_r \right) \right]^{-1}, \quad (3.24a)$$

$$U_{c/s} = \pm U, \quad (3.24b)$$

where inversion is performed in $\nu\nu'$ and U is the bare Hubbard- U as it appears in the Hamiltonian.

This trick causes the Bethe-Salpeter ladder in the particle-hole channels, spin and charge, to appear separated by U_r , (Ref. [71] p. 30)

$$\chi_r^{\nu\nu'q} = \chi_r^{*,\nu\nu'q} - \frac{1}{\beta} \sum_{\nu_1\nu_2} \chi_r^{*,\nu\nu_1q} U_r^{\nu_1\nu_2} \chi_r^{\nu_2\nu'q}, \quad (3.25a)$$

$$= \chi_r^{*,\nu\nu'q} - U_r \left(1 - U_r \frac{1}{\beta^2} \sum_{\nu_1\nu_2} \chi_r^{*,\nu_1\nu_2q} \right) \frac{1}{\beta^2} \sum_{\nu_3\nu_4} \chi_r^{*,\nu\nu_3q} \chi_r^{*,\nu_4\nu'q} + \mathcal{O}(\chi^{*4}), \quad (3.25b)$$

where $U_r^{\nu_1\nu_2} = \text{const.}$

The last line was obtained by iterating the equation in the former line. The latter equation builds ladder diagrams by means of the local 2PI vertex in the particle-hole channels, $\Gamma_{c/s}^{\text{loc},\nu\nu'\omega}$, combined with the momentum-dependent lattice Green's function, G_k^{loc} . By a closer look this must violate the Ward-Takahashi identity and consequently violates the Baym-Kadanoff conservation relation [74], which schematically reads⁸ $\Gamma = \frac{\delta\Sigma}{\delta G}$.

⁸ This reveals the contradiction $\arg(\mathbf{k}\text{-indep.}) = \arg(\mathbf{k}\text{-dep.})$.

3. Methods

Moriyaesque λ -correction. As a direct consequence of the violation of the Baym-Kadanoff conservation relation it seems logical to use ladder D Γ A as a single-shot calculation. However, important two-particle self-consistent properties related to the Pauli principle are lost [75] even then. In particular, the asymptotic behaviour of the self-energy is one property where this loss is reflected. We recall, that the proper asymptotic behaviour is derived by expanding the Schwinger-Dyson equation of motion, Equation (3.18), and analytic evaluation of the sum [69]

$$\Sigma_k = \frac{Un}{2} + \frac{1}{i\nu} U^2 \frac{1}{\beta^3} \underbrace{\sum_{k_1 k_2 q} \chi_{\uparrow\uparrow}^{k_1 k_2 q}}_{\frac{n}{2} \left(1 - \frac{n}{2}\right)} + \mathcal{O}\left(\frac{1}{(i\nu)^2}\right). \quad (3.26)$$

Note the direct connection to the susceptibility. Although this behaviour is not reproduced by Equation (3.25b), it offers a way of improvement as we will see in the following.

The physical interpretation of loosing two-particle self-consistent properties in this procedure is that along with non-local correlations spacial fluctuations should reenter the equations. A mean-field theory such as DMFT overestimates the correlation length ξ of the system [69]. Consider the Ornstein-Zernicke form of the correlation function at $\omega = 0$ given as

$$\chi_r^{\nu\nu'q} = \frac{A}{(\mathbf{q} - \mathbf{Q}_r)^2 + \xi^{-2}}. \quad (3.27)$$

Here, A is some constant and \mathbf{Q}_r determines the spatial modulation of the instability, e.g. antiferromagnetic, ferromagnetic charge density wave etc.. The response is at its maximum for an external perturbation which is spatially described by the specific q -vector, $\mathbf{q} = \mathbf{Q}_r$. In the case of commensurate antiferromagnetic fluctuations, relevant here, this is $\mathbf{Q}_s = (\pi, \pi)$.

In practice the overestimated correlation length ξ is compensated for by the so-called Moriyaesque λ -correction. ξ^{-2} is too small, if ξ is overestimated. ξ is decreased by adding a positive constant λ_r to χ_r^{-1} . In order to choose the value λ_r , we recall the connection between the response function and the asymptotic behaviour of the self-energy in Equation (3.26). For the response computed by hands of a Bethe-Salpether ladder in the spin and charge channel, i.e. for Equation (3.25b), the condition imposed by the Moriyaesque λ -correction reads

$$\frac{1}{\beta^3} \sum_{\nu\nu'q} \frac{1}{2} \left(\chi_s^{\lambda_s, \nu\nu'q} + \chi_c^{\lambda_c, \nu\nu'q} \right) \stackrel{!}{=} \frac{n}{2} \left(1 - \frac{n}{2} \right), \quad (3.28a)$$

$$\chi_r^{\lambda_r, \nu\nu'q} = \left[\left(\chi_r^{\nu\nu'q} \right)^{-1} + \lambda_r \right]^{-1}. \quad (3.28b)$$

In our calculation, we have additionally assumed that magnetic fluctuations are prevalent for the specific model. Hence, the λ -correction for the charge channel can be ne-

3. Methods

glected⁹, $\lambda_c \equiv 0$. As a result, the correct asymptotic behaviour, as in Equation (3.26), is enforced by means of $\lambda_s > 0$.

At last, we define yet another auxiliary quantity, a triangular vertex,

$$\gamma_r^{\nu q} = \left(\sum_{\mathbf{k}\mathbf{k}'} \chi_0^{\text{loc},\mathbf{k}\mathbf{k}'q} \right)^{-1} \frac{1}{\beta} \sum_{\nu''} \chi_r^{*,\nu\nu''q}, \quad (3.29)$$

with inversion in $\nu\nu'$. Note that the first sum goes over two momenta, but one frequency. The ladder full vertex F_{lad} in the particle-hole channels can then be computed as

$$F_{\text{lad},r=c/s}^{\nu\nu'q} = \left(\sum_{\mathbf{k}\mathbf{k}'} \chi_0^{\text{loc},\mathbf{k}\mathbf{k}'q} \right)^{-1} \left[\beta \delta_{\nu\nu'} - \chi_r^{*,\nu\nu'q} \left(\sum_{\mathbf{k}\mathbf{k}'} \chi_0^{\text{loc},\mathbf{k}\mathbf{k}'q} \right)^{-1} \right] + U_r \left(1 - U_r \frac{1}{\beta^2} \sum_{\nu_1\nu_2} \chi_r^{\lambda_r,\nu_1\nu_2q} \right) \gamma_r^{\nu q} \gamma_r^{\nu'q} \quad (3.30)$$

As the Bethe-Salpeter ladder in Equation (3.25b) is built in the spin and charge channels, the momentum-dependence of the full vertex $F_{\text{lad},r=c/s}^{\nu\nu'q}$ appears only in the spin and charge reducible vertices $\Phi_{c/s}^{\nu\nu'q}$:

$$\Phi_{c/s}^{\nu\nu'q} = F_{\text{lad},c/s}^{\nu\nu'q} - \Gamma_{\text{loc},c/s}^{\nu\nu'\omega}. \quad (3.31)$$

The final result for the full vertex F is computed by plugging Equation (3.31) in Equation (3.16), and utilizing SU(2) symmetry, $F_{\uparrow\downarrow,ph}^{k(k+q)(k'-k)} = -(F_{\uparrow\uparrow,ph}^{kkq} - F_{\uparrow\downarrow,ph}^{kkq}) = -F_s^{kkq}$.

$$F_{\uparrow\downarrow}^{kk'q} = \frac{1}{2} \left(F_{\text{lad},c}^{\nu\nu'q} - F_{\text{lad},s}^{\nu\nu'q} \right) - F_{\text{lad},s}^{\nu(\nu+\omega)(k-k')} - \frac{1}{2} \left(F_{\text{loc},c}^{\nu\nu'\omega} - F_{\text{loc},s}^{\nu\nu'\omega} \right). \quad (3.32)$$

Here, $F_{\text{lad},c/s}^{\nu\nu'q}$ is given in Equation (3.30) and $F_{\text{loc},c/s}^{\nu\nu'\omega}$ is given in Equation (3.21).

The momentum-dependent ladder D Γ A self-energy is obtained using the Schwinger-Dyson equation, Equations (3.18) and (3.32) (Ref. [71] Equations (2.27) and (2.52))

$$\Sigma_k = \frac{Un}{2} + \frac{U}{\beta^2} \sum_{\mathbf{k}'q} F_{\uparrow\downarrow}^{k\mathbf{k}'q} G_{\mathbf{k}'}^{\text{loc}} G_{\mathbf{k}'+q}^{\text{loc}} G_{\mathbf{k}+q}^{\text{loc}}, \quad (3.33a)$$

$$= \frac{Un}{2} - \frac{U}{2\beta^2} \sum_q \left[\gamma_c^{\nu q} - 3\gamma_s^{\nu q} + U\gamma_c^{\nu q} \left(\frac{1}{\beta^2} \sum_{\nu_1\nu_2} \chi_c^{\lambda_c,\nu_1\nu_2q} \right) + 3U\gamma_s^{\nu q} \left(\frac{1}{\beta^2} \sum_{\nu_1\nu_2} \chi_s^{\lambda_s,\nu_1\nu_2q} \right) + 2 - \sum_{\mathbf{k}'} \left(F_{\text{loc},c}^{\nu\nu'\omega} - F_{\text{loc},s}^{\nu\nu'\omega} \right) G_{\mathbf{k}'}^{\text{loc}} G_{\mathbf{k}'+q}^{\text{loc}} \right] G_{\mathbf{k}+q}^{\text{loc}}. \quad (3.33b)$$

The second line, Equation (3.33b), is actually evaluated in the program, which sparse from the necessity of evaluating Equation (3.32).

⁹In general, charge-density waves are present in cuprates. Thus, one may question this decision. On the other hand, charge-density waves occur mediated by O $2p_x$ and O $2p_y$ orbitals, which have been neglected by the choice of our model.

3. Methods

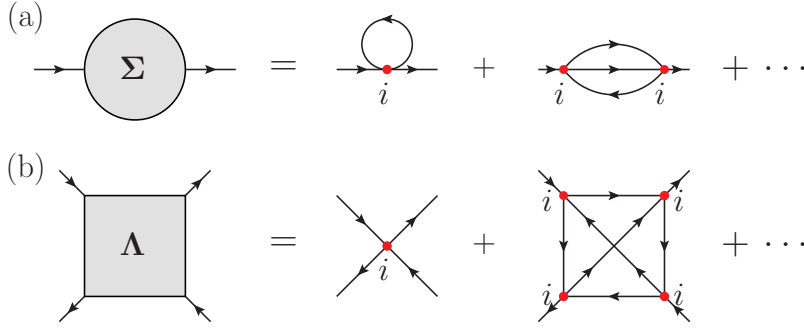


Figure 3.4.: Local vertex. (a) DMFT assumes the fully 1PI vertex, Σ , to be local, (b) in DGA the fully 2PI vertex, Λ , is assumed to be local from Ref. [56].

The approximation that ladder DGA imposes may not immediately be obvious from the technical discussion above. In fact, the approximation on the level of the parquet equations basically reads

$$F_{\uparrow\downarrow}^{kk'q} = \Lambda_{\text{loc},\uparrow\downarrow}^{\nu\nu'\omega} + \Phi_{ph,\uparrow\downarrow}^{kk'q} + \Phi_{ph,\uparrow\downarrow}^{kk'q} + \Phi_{pp,\text{loc},\uparrow\downarrow}^{\nu\nu'\omega}. \quad (3.34)$$

Note the momentum and frequency dependencies. Thus, (i) the fully 2PI vertex Λ , and (ii) the two-particle reducible vertex Φ_{pp} are assumed to be local, while $\Phi_{ph,\uparrow\downarrow}^{kk'q}$ and $\Phi_{ph,\uparrow\downarrow}^{kk'q}$ include particle-hole fluctuations on all length scales. In the following, we briefly discuss the motivation and consequences of each approximation.

The first assumption (i) that Λ is local, invokes the diagrammatic content illustrated in Figure 3.4. The locality of Λ may be an appropriate assumption under consideration of the following three aspects. Firstly, the depicted Feynman diagrams are “*topologically compact*”, hence they are supposedly connected to the most fundamental local processes. Secondly, *numerical evidence* [76] based on DCA calculations on large clusters of a fairly local Λ has been published for a two-dimensional system solved by dynamical cluster approximation (DCA) within a regime of strong non-local correlations. Finally, physically non-local correlations are typically associated with collective modes, which are per definition not expressed by Λ , but ladder diagrams. The latter include e.g. spin density waves and charge density waves. We recall that these are both important in the physical system subject to this work, namely cuprates. As the dominant non-local correlations are due to those modes associated with ladder diagrams, the momentum-dependence of Λ can be likely assumed to be suppressed.

The second approximation (ii), that Φ_{pp} is local, introduces a particular numerical advantage. It is unique to *ladder* DGA in the particle-hole representation. It would not be invoked in the numerically more demanding parquet DGA. Here, instead, the inversion to compute Γ_{pp} , analogous to Equation (3.22), is also done in fermionic indices, the shift $q_{pp} = q + k + k'$, which is necessary to change to particle-particle representation, intertwines the indices. The justification for assuming Φ_{pp} to be local is that non-local scattering prevalently occurs in the particle-hole channels, namely spin and charge.

Summarizing, the ladder DGA algorithm consists of the following five steps:

3. Methods

- Compute the AIM quantities, i.e. the AIM one-particle Green's function G_ν^{AIM} and the AIM generalized susceptibility $\chi_{\sigma\sigma'}^{\text{AIM},\nu\nu'\omega}$, of a converged DMFT calculation by hands of Equations (3.11) and (3.20a), respectively. This also discloses the bare generalized susceptibility $\chi_0^{\text{AIM},\nu\nu'\omega}$ in Equation (3.19).
- Determine the local quantities, namely the local fully connected vertex $F_{c/s}^{\text{loc},\nu\nu'\omega}$ and the local 2PI vertex $\Gamma_{c/s}^{\text{loc},\nu\nu'\omega}$ in the charge and spin channel, as well as the local bare susceptibility $\chi_0^{\text{loc},kk'q}$, in Equations (3.21) to (3.23). All three exclusively include local correlation.
- Compute the generalized susceptibility by means of the Bethe-Salpeter ladder, which includes non-local correlations in the particle-hole channel, as given by Equation (3.25b).
- Enforce a Moriyasque λ -correction as given in Equation (3.28).
- Compute the ladder DGA full vertex and the momentum-dependend ladder DGA self-energy, as obtained by Equation (3.33b)

3.2.3. Dual fermion (DF) theory

The theory of dual fermions was first introduced by A. N. Rubtsov *et al.* [77] in 2008. The code employed in this project was developed by H. Hafermann [78], while the discussion below mostly follows the recent review [56] on diagrammatic extensions by G. Rohringer *et al.*

In this section, we return to the action formalism preceded in Section 2.3 and consider the action of the Hubbard model, cf. Equations (2.19) and (2.20),

$$\mathcal{S}[\bar{c}, c] = \bar{c}_{k\sigma} [-i\nu + \epsilon_{\mathbf{k}} - \mu] c_{k\sigma} + U \bar{c}_{\uparrow x} c_{\uparrow x} \bar{c}_{\downarrow x} c_{\downarrow x}, \quad (3.35)$$

in 4-vector notation defined in Section C.1.

Adding and subtracting a Gaussian part, that is an arbitrary local hybridization function $\sum_{\mathbf{x}} \bar{c}_{\nu\mathbf{x}\sigma} \Delta_\nu c_{\nu\mathbf{x}\sigma} = \sum_{\mathbf{k}} \bar{c}_{\nu\mathbf{k}\sigma} \Delta_\nu c_{\nu\mathbf{k}\sigma}$, yields

$$\begin{aligned} \mathcal{S}[\bar{c}, c] = \sum_{\mathbf{x}} \left(\sum_{\nu\sigma} \bar{c}_{\nu\mathbf{x}\sigma} [-i\nu + \Delta_\nu - \mu] c_{\nu\mathbf{x}\sigma} + U \int_0^\beta d\tau \bar{c}_{\mathbf{x}\uparrow}(\tau) c_{\mathbf{x}\uparrow}(\tau) \bar{c}_{\mathbf{x}\downarrow}(\tau) c_{\mathbf{x}\downarrow}(\tau) \right) \\ + \sum_{\nu\mathbf{k}\sigma} \bar{c}_{\nu\mathbf{k}\sigma} [\epsilon_{\mathbf{k}} - \Delta_\nu] c_{\nu\mathbf{k}\sigma}, \end{aligned} \quad (3.36)$$

where we adopted a less compact notation to emphasize the summation. By comparison of Equation (3.36) with the action of the Anderson impurity model Equation (3.4), one can identify $\dim(\mathbf{x})$ local reference systems, given by

$$\mathcal{S}_{\text{loc}}[\bar{c}, c] = \sum_{\nu\sigma} \bar{c}_{\nu\sigma} [-i\nu + \Delta_\nu - \mu] c_{\nu\sigma} + U \int_0^\beta d\tau \bar{c}_\uparrow(\tau) c_\uparrow(\tau) \bar{c}_\downarrow(\tau) c_\downarrow(\tau). \quad (3.37)$$

3. Methods

As discussed in Section 3.1, the AIM can be numerically solved.

The Hubbard action¹⁰ is given as

$$\mathcal{S}[\bar{c}, c] = \sum_{\mathbf{x}} \mathcal{S}_{\text{loc}}[\bar{c}_{\mathbf{x}}, c_{\mathbf{x}}] + \sum_{\nu\mathbf{k}\sigma} \bar{c}_{\nu\mathbf{k}\sigma} [\epsilon_{\mathbf{k}} - \Delta_{\nu}] c_{\nu\mathbf{k}\sigma}. \quad (3.38)$$

The so-called dual fermions are introduced by a Hubbard-Stratonovich transformation, which reads

$$e^{-\bar{c}_{\nu\mathbf{k}\sigma}[\epsilon_{\mathbf{k}} - \Delta_{\nu}]c_{\nu\mathbf{k}\sigma}} = -\frac{1}{\prod_{\nu\mathbf{k}\sigma} b_{\nu\sigma}^2 [\epsilon_{\mathbf{k}} - \Delta_{\nu}]^{-1}} \int_{\tilde{c}\tilde{c}} e^{b_{\nu\sigma}^2 \bar{c}_{\nu\mathbf{k}\sigma} [\epsilon_{\mathbf{k}} - \Delta_{\nu}] \tilde{c}_{\nu\mathbf{k}\sigma} + b_{\nu\sigma} [\bar{c}_{\nu\mathbf{k}\sigma} \tilde{c}_{\nu\mathbf{k}\sigma} + \bar{c}_{\nu\mathbf{k}\sigma} c_{\nu\mathbf{k}\sigma}]}, \quad (3.39)$$

where $b_{\nu\sigma} = G_{\nu\sigma}^{\text{loc}-1}$ is a properly chosen proportionality factor, and $\tilde{c}(\tilde{c})$ are dual fields. This leads to an alternative representation of the partition function in a form

$$Z = \int_{\bar{c}c} e^{-\mathcal{S}[\bar{c}, c]} = \tilde{Z} \int_{\bar{c}\tilde{c}} \int_{\tilde{c}\tilde{c}} e^{-\mathcal{S}[\bar{c}, c; \tilde{c}, \tilde{c}]}, \quad (3.40)$$

$$\mathcal{S}[\bar{c}, c; \tilde{c}, \tilde{c}] = \sum_{\mathbf{x}} \mathcal{S}_{\text{loc}}[\bar{c}, c] + \sum_{\nu\mathbf{k}\sigma} \left\{ \bar{c}_{\nu\mathbf{k}\sigma} \left(G_{\nu\sigma}^{\text{loc}-1} \right)^2 [\Delta_{\nu} - \epsilon_{\mathbf{k}}] \tilde{c}_{\nu\mathbf{k}\sigma} - G_{\nu\sigma}^{\text{loc}-1} [\bar{c}_{\nu\mathbf{k}\sigma} \tilde{c}_{\nu\mathbf{k}\sigma} + \bar{c}_{\nu\mathbf{k}\sigma} c_{\nu\mathbf{k}\sigma}] \right\}, \quad (3.41)$$

where a sole transformation, but no approximation, has been acted.

In the next step, the physical fields $c(\bar{c})$ are integrated over.

$$Z = \tilde{Z} Z_{\text{loc}} \int_{\tilde{c}\tilde{c}} e^{-\tilde{\mathcal{S}}[\tilde{c}, \tilde{c}]}, \quad (3.42)$$

$$\tilde{\mathcal{S}}[\tilde{c}, \tilde{c}] = -\sum_{\nu\mathbf{k}\sigma} \tilde{G}_{0,k}^{-1} \bar{c}_{\nu\mathbf{k}\sigma} \tilde{c}_{\nu\mathbf{k}\sigma} + \sum_i V_{\text{eff}}[\tilde{c}_i, \tilde{c}_i], \quad (3.43)$$

where the remaining dual action $\tilde{\mathcal{S}}[\tilde{c}, \tilde{c}]$ generally contains a non-interacting part proportional to the bare dual single-particle Green's function, as well as an interacting part V_{eff} up to arbitrary order in dual fields $\tilde{c}(\tilde{c})$.

The connection between the bare dual single-particle Green's function and the self-consistently determined AIM Green's function $G_{\nu}^{\text{loc}} = [i\nu - \Delta_{\nu} + \mu - \Sigma_{\nu}^{\text{loc}}]$ is defined as

$$\tilde{G}_{0,k} = \left[(G_{\nu}^{\text{loc}})^{-1} + (\Delta_{\nu} - \epsilon_{\mathbf{k}}) \right]^{-1} - G_{\nu}^{\text{loc}}, \quad (3.44)$$

$$= G_{\nu\mathbf{k}}^{\text{loc}} - G_{\nu}^{\text{loc}}. \quad (3.45)$$

This relation allows the interpretation of dual fermions as “non-local degrees of freedom”.

The dual interaction is expanded in powers of the dual fields. Note that a Taylor expansion in $\tilde{c}(\tilde{c})$ imply variations, e.g. for first order of the form $\frac{\delta}{\delta\tilde{c}} \frac{\delta}{\delta\tilde{c}} \frac{\delta}{\delta\tilde{c}} \frac{\delta}{\delta\tilde{c}}$. Because dual

¹⁰Here, in terms of the local reference systems.

3. Methods

fields are sources to physical fields, as seen in Equation (3.41), the dual interaction of n th order consists of local connected n -particle vertex functions $F^{(2n)}$. The wisely-chosen proportionality factor $G_{\nu\sigma}^{\text{loc}-1}$ conveniently amputates all external legs. In particular, our calculations include the first order term given as [78] (Equation (A.60))

$$V_{\text{eff}}[\tilde{c}_i, \tilde{c}_i] = \frac{1}{4} \sum_{\substack{\nu\nu'\omega \\ \sigma\sigma'}} (2 - \delta_{\sigma\sigma'}) F_{\sigma\sigma'}^{\nu\nu'\omega} \tilde{c}_{i\nu\sigma} \tilde{c}_{i(\nu+\omega)\sigma} \tilde{c}_{i(\nu'+\omega)\sigma} \tilde{c}_{i\nu'\sigma}. \quad (3.46)$$

We have omitted higher-order terms, as these are assumed to be negligible¹¹ in [80] this particular case. At this point the DF approach becomes an approximation.

The system can be written in terms of a generating functional given as

$$Z[\eta, \bar{\eta}; \tilde{\eta}, \bar{\tilde{\eta}}] = \int_{\tilde{c}\bar{\tilde{c}}} e^{-\tilde{S}[\tilde{c}, \bar{\tilde{c}}] - \sum_{k\sigma} [\epsilon_{\mathbf{k}} - \Delta_{\nu}]^{-1} (G_{\nu}^{\text{loc}})^{-1} [\bar{\tilde{c}}_{k\sigma} \eta_{k\sigma} + \bar{\eta}_{k\sigma} \tilde{c}_{k\sigma}] + [\epsilon_{\mathbf{k}} - \Delta_{\nu}]^{-1} \bar{\eta}_{k\sigma} \eta_{k\sigma} + \bar{\tilde{\eta}}_{k\sigma} \tilde{c}_{k\sigma} + \tilde{c}_{k\sigma} \bar{\tilde{\eta}}_{k\sigma}}, \quad (3.47)$$

where source fields $\eta(\bar{\eta})$ and their dual analogous $\tilde{\eta}(\bar{\tilde{\eta}})$ have been introduced. The (dual) Green's function can be obtained through variations

$$G = \frac{1}{Z} \frac{\delta^2}{\delta\eta\delta\eta} Z[\eta, \bar{\eta}; \tilde{\eta}, \bar{\tilde{\eta}}] \Big|_{\eta, \bar{\eta}; \tilde{\eta}, \bar{\tilde{\eta}}=0}, \quad (3.48)$$

$$\tilde{G} = \frac{1}{Z} \frac{\delta^2}{\delta\tilde{\eta}\delta\tilde{\eta}} Z[\eta, \bar{\eta}; \tilde{\eta}, \bar{\tilde{\eta}}] \Big|_{\eta, \bar{\eta}; \tilde{\eta}, \bar{\tilde{\eta}}=0}, \quad (3.49)$$

which yields

$$G_{\mathbf{k}} = [\epsilon_{\mathbf{k}} - \Delta_{\nu}]^{-1} (G_{\nu}^{\text{loc}})^{-1} \tilde{G}_{\mathbf{k}} (G_{\nu}^{\text{loc}})^{-1} [\epsilon_{\mathbf{k}} - \Delta_{\nu}]^{-1} - [\epsilon_{\mathbf{k}} - \Delta_{\nu}]^{-1}, \quad (3.50)$$

and a relation between the physical and the dual self-energy, that reads

$$\Sigma_{\mathbf{k}} = \Sigma_{\nu}^{\text{loc}} + \frac{\tilde{\Sigma}_{\mathbf{k}}}{1 + G_{\nu}^{\text{loc}} \tilde{\Sigma}_{\mathbf{k}}}. \quad (3.51)$$

At this point, the problem formulated in Equation (3.43) actually has the same form in dual space as the original problem, Equation (3.35), but with a more complicated interaction. The advantage is that V_{eff} can be seen as a small parameter [77], and hence a perturbation expansion in these newly introduced degrees of freedom might be appropriate. Dual fermions, thus, live close to the non-interacting limit. As mentioned, they are defined as being completely delocalized, which leads to the formulation of a self-consistent condition,

$$\sum_{\mathbf{k}} \tilde{G}_{\mathbf{k}} = 0. \quad (3.52)$$

¹¹How well this is justified is a matter of current discussion [79] within the community. In practice, the computational effort to include higher orders would be considerably higher. This is why it has not been systematically investigated, but often argued, that higher order contributions are small.

3. Methods

It states that all fully local diagrams in dual space vanish.

The dual fermion self-energy can be computed in a ladder approximation scheme [78] in the dual space. In the particle-hole channel it reads [56]

$$\begin{aligned} \tilde{\Sigma}_k = & -\frac{1}{\beta^2} \frac{1}{2} \sum_{k'q} F_{\text{loc},c}^{\nu\nu'\omega} \tilde{G}_{k'} \tilde{G}_{k'+q} \tilde{G}_{k+q} \left[F_{\text{lad},c}^{\nu\nu'q} - \frac{1}{2} F_{\text{loc},c}^{\nu\nu'\omega} \right] \\ & - \frac{1}{\beta^2} \frac{3}{2} \sum_{k'q} F_{\text{loc},s}^{\nu\nu'\omega} \tilde{G}_{k'} \tilde{G}_{k'+q} \tilde{G}_{k+q} \left[F_{\text{lad},s}^{\nu\nu'q} - \frac{1}{2} F_{\text{loc},s}^{\nu\nu'\omega} \right], \end{aligned} \quad (3.53)$$

where F_{lad} and F_{loc} are exactly the same as in Section 3.2.2. The updated dual Green's function is obtained by the dual Dyson Equation

$$\tilde{G}_k^{-1} = \tilde{G}_0^{-1} - \tilde{\Sigma}_k. \quad (3.54)$$

Iterating Equations (3.53) and (3.54) until the self-consistency condition Equation (3.52) is full-filled is often referred to as inner loop. While updating the AIM and newly computing the fully connected vertex F is referred to as outer loop.

3.3. Padé Approximation

Hitherto, multiple methods have been discussed, in order to compute observables as a function of Matsubara frequencies, i.e. for imaginary time evolution. The rotation to imaginary time was essential to enable numerical computation of a thermal state, however it severely limits physical interpretation.

In this section, we address the procedure of analytic continuation, which unveils the according observables as a function of real frequencies. Only from the latter one can extract physical information. In particular, the technique employed here is the Padé approximation, whose intrinsic strength and limitation will be detailed.

Analytic continuation of numerical data $g(z_i)$ is performed in two steps:

1. Determine an analytic expression f , which fits the data such that

$$f^n(z_i) \equiv g(z_i) \quad \forall i = 1, 2, \dots, n, \quad (3.55)$$

where $n \gg 1$ and z_i is complex. In other words, f is defined on a non-empty subset $U \subset \mathbb{C}$.

2. Determine a function F defined on a larger subset $V \subset \mathbb{C}, U \subset V$, so that

$$F(z) = f(z) \quad \forall z \in U. \quad (3.56)$$

We then call F the unique analytic continuation of f .

Why is this an ill-defined procedure, but nonetheless what we do? In order to answer, we shall first understand when two analytic functions are equal. This is given by the identity theorem, which reads as follows:

3. Methods

Identity theorem: U shall be a domain (i.e. an open, non-zero subset) in the complex plain \mathbb{C} and $z_0 \in U$ shall be the limit of the series $\{z_n\} \subset U$, with $z_n \neq z_0$. If two analytic functions f and g are equal for all z_n , they are equal in the entire domain U .

Proof: Assuming f and g are equal for all z_n , i.e. $h(z_n) = f(z_n) - g(z_n) = 0, \forall z_n \neq z_0$, we want to show that $h(z) = 0, \forall z \in U$. Let us expand $h(z)$ in a Taylor series around z_0 :

$$h(z) = c_1 + c_2(z - z_0) + c_3(z - z_0)^2 + \dots \quad (3.57)$$

The constant part clearly vanishes by assumption, as f and g have the same limit

$$h(z = z_0) = c_1 = \lim_{z \rightarrow z_0} f(z) - g(z) = 0. \quad (3.58)$$

Suppose now the linear order does not vanish

$$0 \neq c_2 = \lim_{z \rightarrow z_0} \frac{h(z)}{z - z_0} = \lim_{n \rightarrow \infty} \frac{h(z_n)}{z_n - z_0} = 0, \quad (3.59)$$

which yields a contradiction, $0 \neq 0$. The last equality is obtained by looking at the series elements, while keeping in mind that $h(z_n) = 0, \forall z_n$,

$$\left\{ \frac{h(z_n)}{z_n - z_0} \right\} = \left\{ \frac{h(z_1)}{z_1 - z_0}, \frac{h(z_2)}{z_2 - z_0}, \dots \right\} = \{0, 0, \dots\}. \quad (3.60)$$

The same argument can be made for any order. Hence all coefficients of the Taylor expansion are zero. Consequently, $h(z) = 0, \forall z \in U$. *q.e.d.*

In other words, in order to determine the analytic continuation, F must be equal to f in the entire domain U , i.e. fulfill Equation (3.56). However to fulfill Equation (3.56), the functions must have an accumulation point z_0 , which requires countably infinitely many points. Thus uniqueness is impossible to achieve by means of finite numerical data.

Why should we have confidence in the result of this mathematically ill-defined problem? Because physical properties given by the specific observable of the system is checked additionally. This is detailed in the Paragraph Physical checks. As a caveat, note however, that the result ultimately remains afflicted with the systematic error introduced by a finite set of data.

In the following, we demonstrate the procedure as it was implemented in the course of this project. The code was written in c++ and benchmarked with a similar fortran program.

Padé approximation. In practice, the first step to perform Padé approximation is to fit the data, $g(z_i)$, to a chain fraction, $f^n(z)$, of fitorder n .

3. Methods

In fact, $f^n(z)$ can be written as

$$f^n(z) = \frac{a_1}{1 + \frac{a_2(z-z_1)}{1 + \frac{a_3(z-z_2)}{1 + \dots \frac{a_{n-1}(z-z_{n-2})}{1 + \frac{a_n(z-z_{n-1})}{1 + a_n(z-z_{n-1})}}}}, \quad (3.61)$$

where n is the number of parameters a_i for given $n - 1$ points z_i . In order to fix a_i so that

$$f^n(z_i) \equiv g(z_i) \quad \forall i = 1, 2, \dots, n, \quad (3.62)$$

a recursion to determine the i th parameter a_i is given by

$$f^n(z_1) = g(z_1) = a_1, \quad (3.63a)$$

$$f^n(z_i) = g(z_i) = c_1, \quad (3.63b)$$

$$c_j = \left(\frac{a_{j-1}}{c_{j-1}} - 1 \right) \frac{1}{z_i - z_{j-1}}, \quad j = 2, \dots, i - 1, \quad (3.63c)$$

$$a_i = \left(\frac{a_{i-1}}{c_{i-1}} - 1 \right) \frac{1}{z_i - z_{i-1}}, \quad i = 2, \dots, n, \quad (3.63d)$$

where c_j are mere helper to iteratively determine a_i . Note that n data values $g(z_i)$ at n data points z_i are necessary to fully determine Equation (3.62). This is demonstrated for the example of $n = 4$ in Section B.6.

Rewriting in terms of a rational function. For the purpose of investigating the analytical properties, such as poles and asymptotic behaviour, we rewrite Equation (3.62) in terms of a numerator polynomial p and denominator polynomial q . With the ansatz,

$$f^{(n)} = \frac{p^{(n)}(z)}{q^{(n)}(z)} = \frac{a_1}{1 + (z - z_1) \frac{p^{(n-1)}(z)}{q^{(n-1)}(z)}} = \frac{a_1 q^{(n-1)}(z)}{q^{(n-1)}(z) + (z - z_1) p^{(n-1)}(z)}, \quad (3.64)$$

we obtain the following recursion:

$$p^{(1)}(z) = a_n, \quad (3.65a)$$

$$q^{(1)}(z) = 1, \quad (3.65b)$$

$$p^{(j)}(z) = a_{n-j+1} q^{(j-1)}(z), \quad (3.65c)$$

$$q^{(j)}(z) = q^{(j-1)}(z) + (z - z_{n-j+1}) p^{(j-1)}(z) \quad j \in [1, n]. \quad (3.65d)$$

The application to $n = 4$ is performed in Section B.6. The recursion is used to compute the polynomial coefficients, which in turn enable to obtain the roots of the numerator and denominator. While there are many methods to unveil roots of a polynomial, here we use the Numerical Recipes routine “roots”, which employs Laguerre’s method. [81]

3. Methods

Physical input. The data, $g(z_i)$, could be any observable that depends on *one* fermionic or bosonic Matsubara frequency.¹² In fact, in the case of DMFT, DΓA and DF, this can be the self-energy $\Sigma_{\nu\mathbf{k}}$ or the single-particle Green's function $G_{\nu\mathbf{k}}$. Next, we discuss the case of fitting the $\Sigma_{\nu\mathbf{k}}$. Note that any \mathbf{k} -point has to be considered separately, hence, we drop the index here.

The input is given by Σ_{ν_j} at $\nu_j = (2j + 1)\pi/\beta$ with $j \in \mathbb{N}$. Typically $j = 0, 1, \dots, n$, where n is of the order of 10 and j does not necessarily take on all values, which effectively reduces the fit order.

For a more stable fit the constant Hartree contribution, i.e. $Un/2$, is subtracted before performing the recursion of Equation (3.63). Subsequently the chain fraction is rewritten as a rational function and the roots of numerator and denominator are computed, as described above. Finally, the analytic expression, namely the rational function, is tested for its physical properties.

Physical checks. The asymptotic behaviour of the one-particle irreducible self-energy is known to be

$$\nu \rightarrow \infty : \Sigma_{\nu} \propto -\frac{U^2 n}{2} \left(1 - \frac{n}{2}\right) \frac{1}{\nu}, \quad (3.66)$$

see Ref. [69]. This is checked by comparison to the ratio of the highest polynomial coefficients of numerator and denominator. Note that only even fit orders can yield a denominator with higher polynomial degree than the numerator, and consequently $1/\nu$ asymptotic behaviour.

Furthermore, the self-energy (as well as the Greens function) is analytic in the upper complex plane. This means that there are no poles of the rational function in the upper complex plane, or equally, there are no roots of the denominator that do not cancel with the numerator with positive imaginary part.

For good measure. From the analytic expression of the self-energy, $\Sigma(z) = \frac{p^{\Sigma}(z)}{q^{\Sigma}(z)}$, which has been examined to be physical, other observables can be computed. In particular, the single-particle Green's function

$$G_{\nu\mathbf{k}} = \frac{q^{\Sigma}(z)}{zq^{\Sigma}(z) - Kq^{\Sigma}(z) + p^{\Sigma}(z)} \equiv \frac{p^G(z)}{q^G(z)}, \quad (3.67)$$

where $K = (\epsilon_{\mathbf{k}} - \mu)$ merges all contributions constant in \mathbf{k} . Again the analyticity and the asymptotic behaviour can be checked.

By means of the single particle Green's function the spectral function can be computed as follows,

$$A(\omega) = -\frac{1}{\pi} \text{Im} G_{\mathbf{k}}(\omega) = \frac{1}{2\pi i} [G_{\mathbf{k}}^*(\omega) - G_{\mathbf{k}}(\omega)]. \quad (3.68)$$

Here, we check the zeros on the real axis to verify that the spectral function is positive within a certain range of ω around the Fermi surface, i.e. $\omega = 0$. The sum rule for the

¹²The procedure cannot be applied to quantities, which depend on multiple Matsubara frequencies, such as the generalized susceptibility.

3. Methods

spectral function,

$$\int_{-\infty}^{+\infty} d\omega A(\omega) \equiv 1, \quad (3.69)$$

is already checked by assuring the single-particle Green's function to be analytic.

A word about the fitorder. At first glance, it is counter-intuitive to use a low fitorder, because the *finite* amount of numerical data is the reason the fit is ill-conditioned in the first place. It was reasoned in Section 3.3, that a unique analytic expression can only be found when there is an accumulation point. However, considering that Matsubara frequencies are equidistant, it is not beneficial to consider many or few data points in respect to accumulation.¹³ In fact for a Padé fit procedure, each additional fitorder results in a pole, i.e. roots of the denominator. When all physical poles are retrieved, additional roots of the denominator ought to be cancelled by roots of the numerator. The root cancellation is never exact and causes artifacts in the otherwise smooth function. For higher fitorders root cancellation not only introduces artifacts, but is increasingly likely to fail, which results in unphysical contributions. Consequently, it is preferable to use a low fitorder, $5 \leq n \leq 20$.

In the next chapter this procedure of analytic continuation is applied to real data.

¹³ Only for the limit of infinity the asymptotic behaviour yields an accumulation point for equidistant data. However, as the asymptotic behaviour is known analytically this is included by a direct check, see Equation (3.66).

4. Results

In this chapter, we present the scattering rate obtained for the single band two dimensional Hubbard model by means of the self-energy and the computation of the conductivity tensor.

In Chapter 1, we highlighted novel experimental results [1] by the group of N. Barišić et al. at TU Wien. In the experiment, the DC resistivity ρ and the Hall resistivity ρ_H of a cuprate compound were measured. While in the same experimental paper the ratio ρ/ρ_H was regarded to be directly proportional to the scattering rate, we have so far expressed it in terms of the conductivity tensor. As discussed in Section 1.2 the corresponding expressions are Equations (1.4) and (1.9),

$$\rho = 1/\sigma_{xx}, \quad (4.1)$$

$$\rho_H = \sigma_{xy}/\sigma_{xx}^2. \quad (4.2)$$

The most astonishing experimental observation is the doping and compound independent behaviour of $\rho/\rho_H \hat{=} \sigma_{xx}/\sigma_{xy}$. And even more so, that it is quadratic in temperature, as it would be expected for ρ in a normal metal. The experimentalists concluded that the preliminary interpretation as a scattering rate would suggest a universal Fermi-liquid like behaviour in otherwise vastly distinct phases. Here, we aim to theoretically identify the physics observed in the experiment. We formulated our strategy in Section 1.3 and briefly recapitulate it here:

As a first step, we focused on determining a suitable model to describe the physical system. In Chapter 2, we compared different lattice models of the quasi two dimensional copper oxide-planes, whose existence characterizes all cuprates. In our work, we have employed the single band Hubbard model on a square lattice with on-site Coulomb interaction and an appropriate dispersion relation including nearest, next-nearest and next-next-nearest neighbor hopping. The exact parameters are given in Section 2.4.

In Chapter 3, the methods to solve the Hubbard model, which we employ, are reviewed. These are state-of-the-art quantum many-body methods, namely dynamical mean-field theory (DMFT) and diagrammatic extensions to it, such as dynamical vertex approximation (D Γ A) and dual fermion (DF) theory.

We recall that DMFT is able to account for strong electronic correlations in the system, yet can treat only local correlations. This manifests itself in a momentum-independent self-energy, cf. Section 3.1.2. Diagrammatic extensions to DMFT, on the other hand, are able to include spatial correlation at all length scale. It is generally achieved by applying an approximation to the two-particle level, i.e. a two-particle vertex function is assumed to be local as it would be in DMFT. Subsequently, a diagrammatic scheme is employed to compute a momentum-dependent self-energy, which accounts for local and non-local correlations.

4. Results

Ultimately, the computation of two kinds of data is interesting:

- *Extracting the scattering rate from the self-energy, by evaluating it at the Fermi surface.*
- *Direct computation of the ratio ρ/ρ_H by means of the conductivity tensor.*

We will scan the phase diagram by varying the temperature at three different values for the doping $\delta = 0.1, 0.15, 0.2$.

4.1. The self-energy

Here, we will analyze the self-energy in order to ultimately extract the scattering rate. The self-energy is generally a frequency and momentum dependent self-consistent field. While theoretically it accounts for all corrections to the non-interacting lattice dispersion relation due to *local* and *non-local* electronic correlations, in practice the method employed to compute the self-energy on the Matsubara axis introduces further approximations, such as e.g. analytic continuation. This has been discussed in Methods (Chapter 3). In this section, we, hence, focus on the evaluation of the data, also discussing additional uncertainties introduced by extracting the scattering rate.

The concept of quasiparticles is a powerful theoretical framework to describe the interacting system in terms of a renormalised non-interacting system. In particular, as we will see, the scattering rate can be defined in terms of so-called quasiparticle parameters. The quasiparticle picture is introduced by a simple claim of the form

$$G_{\mathbf{k}}^{-1} = i\nu - (\epsilon_{\mathbf{k}} - \mu) - \Sigma_{\mathbf{k}} = Z^{-1} [i\nu - (\tilde{\epsilon}_{\mathbf{k}} - \tilde{\mu})], \quad (4.3)$$

where $\tilde{\epsilon}_{\mathbf{k}} = \sum_{i,j=x,y} (k_i - k_{F,i}) v_{F,j}^*$, with the Fermi velocity $v_{F,j}^* = [\partial \epsilon_{\mathbf{k}}(m^*) / \partial k_j]_{\mathbf{k}=\mathbf{k}_F}$, has the same functional behaviour as $\epsilon_{\mathbf{k}}$ near \mathbf{k}_F , but in terms of an effective mass m^* , $[1/m^*]_{ij} = \frac{1}{\hbar^2} \frac{\partial^2 \tilde{\epsilon}}{\partial k_i \partial k_j}$.

By performing a Taylor expansion of Equation (4.3) around the Fermi surface one obtains the following expressions:

$$\omega : \quad Z = \left[1 - \frac{\partial \text{Im} \Sigma}{\partial \nu} \Big|_{\substack{i\nu \rightarrow 0 \\ \mathbf{k}=\mathbf{k}_F}} \right]^{-1}, \quad (4.4)$$

$$k_i : \quad \left[\frac{m}{m^*} \right]_{ij} = Z \left[1 + \frac{m}{\mathbf{k}_{F,i}} \frac{\partial \text{Re} \Sigma}{\partial k_j} \Big|_{\substack{i\nu \rightarrow 0 \\ \mathbf{k}=\mathbf{k}_F}} \right]. \quad (4.5)$$

On the other hand, we can expand the self-energy on the imaginary frequency axis and

4. Results

express an approximate real frequency self-energy ($i\nu \rightarrow \omega + i0^+$),

$$\Sigma_{\mathbf{k},\nu} \approx \underbrace{\text{Re}\Sigma_{\mathbf{k}_F,\nu \rightarrow 0}}_{\tilde{\mu}-\mu} + \underbrace{i \text{Im}\Sigma_{\mathbf{k}_F,\nu \rightarrow 0}}_{-i\gamma} + i\nu \underbrace{\frac{\partial \text{Im}\Sigma}{\partial \nu}}_{-\alpha} \bigg|_{\substack{\mathbf{k}_F \\ \nu \rightarrow 0}} + \sum_{i=x,y} (k_i - k_{F,i}) \frac{\partial \text{Re}\Sigma}{\partial k_i} \bigg|_{\substack{\mathbf{k}_F \\ \nu \rightarrow 0}}, \quad (4.6)$$

$$\Sigma_\omega = (\text{const. real}) - i\gamma - \omega\alpha + \mathcal{O}(\omega^2), \quad (4.7)$$

with $\gamma, \alpha > 0$.

In order to interpret these quantities, we recall the bare Green's function of the non-interacting problem, $G_{0,\mathbf{k}} = [i\nu - (\epsilon_{\mathbf{k}} - \mu)]^{-1}$, as given in Equation (2.25), which is defined by $H_0 = \sum_{\mathbf{k}} \hat{c}_{\mathbf{k}}^\dagger c_{\mathbf{k}}$. Using the Fourier Transformation given in Appendix C.3, we obtain

$$G_{0,\mathbf{k}}(\tau) = \frac{1}{\beta} \sum_{\nu} e^{-i\nu\tau} G_{0,\mathbf{k}}, \quad \tau > 0, \quad (4.8)$$

$$= -e^{-\epsilon_{\mathbf{k}}\tau} [1 - f(\epsilon_{\mathbf{k}} - \mu)], \quad (4.9)$$

by summing over Matsubara frequencies. This is analogous to the calculation in Appendix B.2. In other words, the propagation shows the proportionality

$$G_{0,\mathbf{k}}(t) \propto e^{-i\epsilon_{\mathbf{k}}t}. \quad (4.10)$$

Following the same arguments within the quasiparticle picture, yields

$$G_{\mathbf{k}}(t) \propto e^{-i(\epsilon_{\mathbf{k}} + \text{Re}\Sigma_{\mathbf{k},\omega=0})t} e^{-\gamma t}, \quad (4.11)$$

which corresponds to a inverse life time, i.e. quasiparticle scattering rate,

$$\gamma_{\mathbf{k}_F} = -\text{Im}\Sigma_{\mathbf{k}_F,\nu \rightarrow 0} \geq 0, \quad (4.12)$$

which can be varying along the Fermi surface, as is expected in the case of cuprates.

We recall that in the case of quasiparticles, the inverse life time can be further renormalized by the quasiparticle weight (controlled by α). Hence, as a first approximation we are mostly interested in the imaginary part of the self-energy on the imaginary axis.¹ This function displays particular behaviour for the paramagnetic metallic system, that is of interest here. It can be seen as a convolution of the low energy expansion, as given by Equation (4.6), and the asymptotic behaviour for high-frequencies, given by [69] (Equation (4.16))

$$\Sigma_\nu = \frac{Un}{2} + \frac{U^2n}{2} \left(1 - \frac{n}{2}\right) \frac{1}{i\nu} + \mathcal{O}\left(\frac{1}{\nu^2}\right). \quad (4.13)$$

¹ Or equally in the imaginary part of the self-energy at $\omega = 0$ and the linear behaviour or the real part of the self-energy on the real axis.

4.1.1. DMFT

In dynamical mean-field theory (DMFT) the self-energy is purely local, as discussed in Section 3.1. We compute the self-energy as a function of Matsubara frequencies by means of exact diagonalization (ED).

Fig. 4.1 shows the imaginary part of the \mathbf{k} -independent DMFT self-energy, i.e. $\text{Im}\Sigma_\nu^{\text{loc}}$, in the low-frequency regime. In the left panel, $\text{Im}\Sigma_\nu^{\text{loc}}$ is plotted at various temperatures for hole doping $\delta = 0.1$, while the right panel displays the same temperatures at higher doping $\delta = 0.2$. The temperatures $T = 580$ K, 290 K and 145 K correspond to $\beta = 20, 40$ and 80 in eV^{-1} .

The calculations were obtained by means of exact diagonalization with $n_s = 5$, i.e. 4 bath energy levels plus 1 impurity site. Each site is on average occupied by $n = 1 - \delta$ electrons. The hole-doping $\delta = 0.1$ is experimentally within the pseudogap (PG) regime of cuprates and close to the antiferromagnetic (AF) phase, while $\delta = 0.2$ is on the verge of the Fermi liquid (FL) regime. For more details on the phenomenology we refer the reader to Section 1.1.

The first observation from Figure 4.1 is that $\text{Im}\Sigma_\nu^{\text{loc}}$ is *doping-dependent*. The absolute value of the function at any point is larger when approaching half-filling (left vs. right panel), or equivalently increasing with decreasing doping.

In order to strengthen this result, we performed a benchmark at the low temperature of $T = 145$ K, i.e. $\beta = 80$, where the finite bath size of our DMFT(ED) algorithm is at its highest disadvantage. We compare the obtained ED results at $n_s = 5$ with ED $n_s = 6$ and 7, as well as CT-QMC calculations by means of the *w2dynamics*-package.² In Figure 4.2, the imaginary part of the self-energy is compared for two different dopings, which yields good agreement for all methods.

This confirms the reasonable physical trend of our numerical data: Within DMFT the corrections due to local electronic correlation are larger within the PG phase relative to the strange metal (SM) regime, and further reduces towards the FL regime.

While this is clearly *not* a universal behaviour, let us further investigate the scattering rate $\gamma_{\mathbf{k}_F}$ and in particular the T -dependence. Figure 4.1 emphasizes the discrete and T -dependent Matsubara frequencies, $\nu_n = \frac{\pi}{\beta}(2n + 1)$ with $n \in \mathbb{Z}$. Consequently, the function $\text{Im}\Sigma_\nu^{\text{loc}}$ is not immediately given at zero frequency, $i\nu \neq 0$. However, by considering Equation (4.12), we are interested in properties on the Fermi surface, i.e. real frequency $\omega = 0$ or the limit $i\nu \rightarrow 0$.

A common practice to extract quasiparticle parameters is to perform a polynomial extrapolation in the low frequency regime, in order to obtain $\text{Im}\Sigma_\nu^{\text{loc}}$ for $i\nu \rightarrow 0$. The issue we encounter in our particular case is that we aim for a T -dependent property. Fitting the first x data points, ensues a potentially spurious T -dependence, which cannot be easily disentangled to retrieve the intrinsic behaviour in T .

A more appropriate treatment of the self-energy, in order to extract physical meaning, is the analytic continuation, which can be performed in different ways. In the case of ED data Padé approximation, described in Section 3.3, is the best currently available

²The *w2dynamics*-package [63] employs continuous-time quantum Monte Carlo in the hybridization expansion.

4. Results

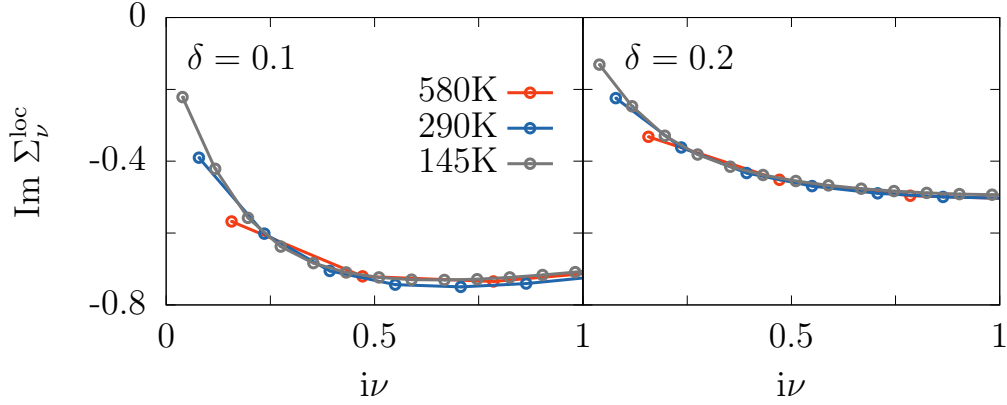


Figure 4.1.: Imaginary part of the self-energy on Matsubara axis computed in DMFT by means of exact diagonalization. The left (right) panel displays doping $\delta = 0.1$ ($\delta = 0.2$) at $T = 580$ K, 290 K and 145 K, i.e. $\beta = 20, 40$ and 80, respectively.

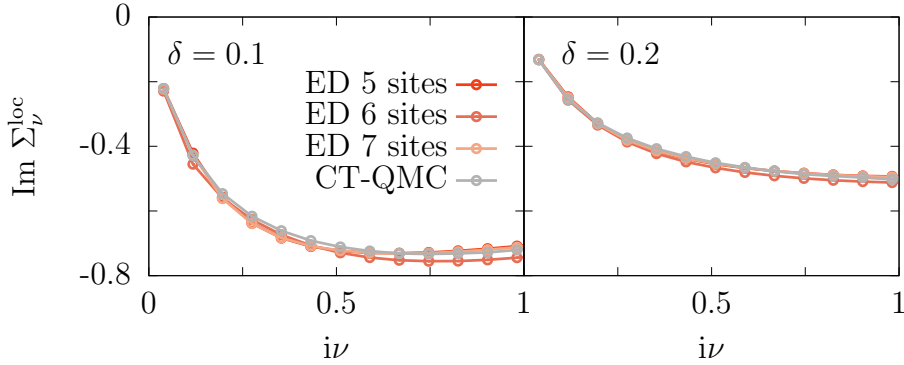


Figure 4.2.: Benchmark for exact diagonalization with $n_s = 5, 6$ and 7 and CT-QMC (*w2dynamics*-package) comparing the imaginary part of the DMFT self-energy on Matsubara axis. The left (right) panel displays doping $\delta = 0.1$ ($\delta = 0.2$) for the lowest temperature of $T = 145$ K, i.e. $\beta = 80$.

4. Results

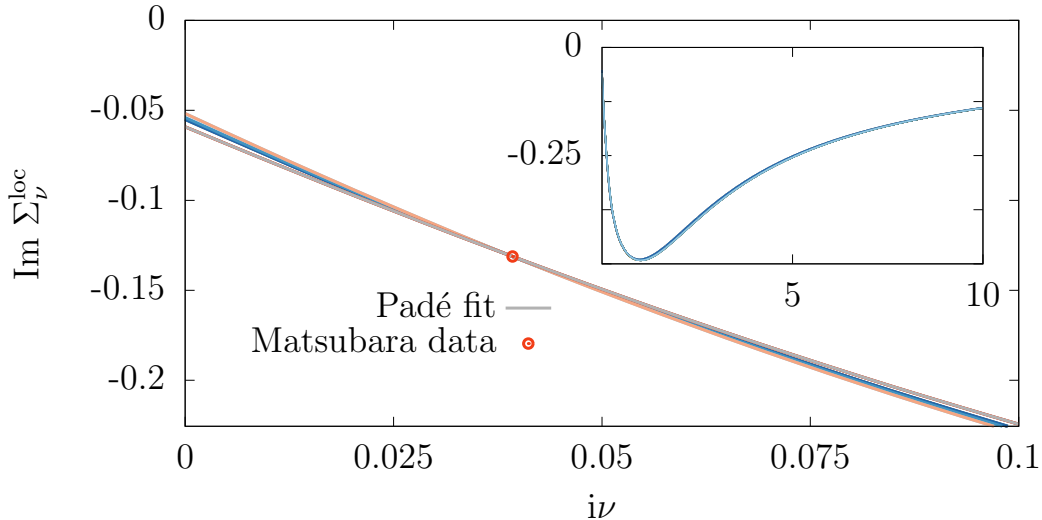


Figure 4.3.: Padé fit of self-energy at doping $\delta = 0.1$ and $T = 145$ K, i.e. $\beta = 80$. Plot shows imaginary part of the self-energy on imaginary axis for Matsubara data (ED $n_s = 5$) and several Padé fits differing in the data points taken into account. The fits spread for $i\nu \rightarrow 0$, although none has poles in the upper complex plane and all obey a physically correct asymptotic behaviour, see inset.

method despite its intrinsic limitations. Due to the inherent ambiguity the Padé fit encounters, we have employed the following strategy:

In particular, we perform 10 000 times a Padé fit of the self-energy, with randomly chosen data points among which two are within the low-frequency linear regime. For temperatures below 300 K, this was achieved by always taking into account the data of the first Matsubara frequency, while the rest is chosen randomly amongst the first 12 Matsubara frequencies. For higher temperatures, above 300 K, the Matsubara frequencies are widely separated. As a result, fits that omit the second frequency do not capture the physics well and therefore the inclusion of the second data point was enforced.

Subsequently, the fit is checked to be analytic in the upper complex plane and display the correct asymptotic behaviour for the self-energy, as given in in Equation (4.13). Approximately 0.1 – 10% pass these checks depending on doping and temperature.

In Figure 4.3, the results of several Padé fits are shown at doping $\delta = 0.1$ and $T = 145$ K. Despite passing all checks the fits spread for $i\nu \rightarrow 0$. As there is no physical argument to prefer one fit over another, we compute the mean and the variance over all physical fits along extracting the quasiparticle parameters.

Figure 4.4 displays the temperature dependence of the quasiparticle scattering rate, $\gamma_{\mathbf{k}_F}(T)$, computed by means of DMFT-ED+Padé approximation. The left panel shows $\gamma_{\mathbf{k}_F}(T) = -\text{Im}\Sigma_{\omega=0}^{\text{loc}}$ for 3 different doping levels, $\delta = 0.1, 0.15$ and 0.2 . Note that the error bar displays $5\times$ the variance.

The low temperature behaviour is dominated by T^2 -behaviour, while the high temper-

4. Results

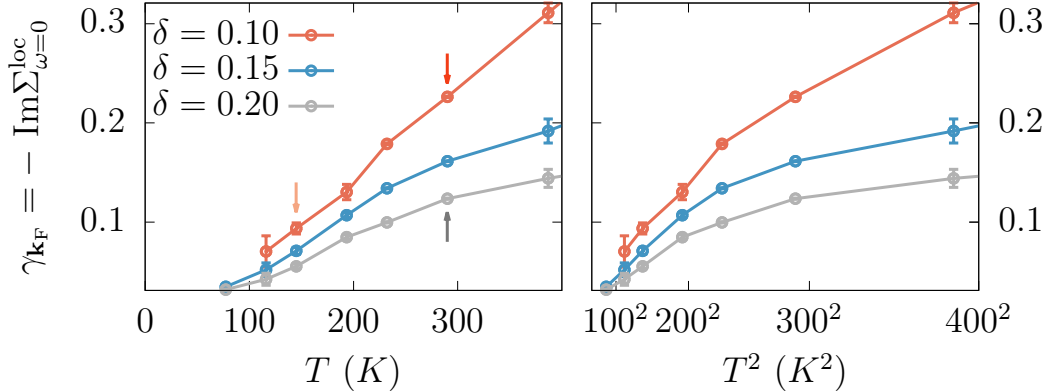


Figure 4.4.: The quasiparticle scattering rate as a function of temperature T (left) and T^2 (right). Different colors correspond to 3 doping levels. The error bar illustrates $5\times$ the variance. The data was computed by means of a dynamical mean field theory exact diagonalization algorithm with $4 + 1$ sites and Padé approximation with enforced physical constraints.

ature regime is governed by linear behaviour. This is strengthened by the right panel of Figure 4.4, where the scattering rate is plotted as a function of T^2 . By comparison with the experiment, the overall T -dependence of $\gamma_{\mathbf{k}_F}(T)$, though not universal, resembles the behaviour of the planar resistivity ρ , rather than ρ/ρ_H , where ρ_H is the Hall conductivity, (we refer the reader to Figure 1.3).

In general, the quantitative resemblance of the T -dependency to ρ is not surprising, as the planar resistivity is due to inelastic scattering events of the charge carrying quasiparticles connected to the single-particle spectral function, which is averaged over the entire Fermi surface. The generically expected behaviour of a Fermi liquid due to Sommerfeld expansion is to display $\gamma_{\mathbf{k}_F}(T) \propto aT^2 - bT^4$, where a and b are positive. The observed roughly linear behaviour might be caused by the compensation of the two expansions in the intermediate T -regime.

The spectral function of the one-particle propagator,

$$A^{\text{loc}}(\omega) = -\frac{1}{\pi} \text{Im} G_{\text{R}}^{\text{loc}}(\omega), \quad (4.14)$$

$$G_{\text{R}}^{\text{loc}}(\omega) = \frac{1}{N_{\mathbf{k}}} \sum_{\mathbf{k}} G_{\mathbf{k},\text{R}}^{\text{loc}}(\omega), \quad (4.15)$$

is a byproduct of the analytical continuation. In Figure 4.5, the spectral function is shown for three cases, in order to illustrate the changes observed in temperature and in doping.

Varying the doping from $\delta = 0.1$ to 0.2 at constant temperature $T = 290$ K suppresses the local electronic correlations. This statement is based on multiple observations in Figure 4.5: (i) The overall spectral structures at $\delta = 0.2$ are smoother and less pronounced.

4. Results

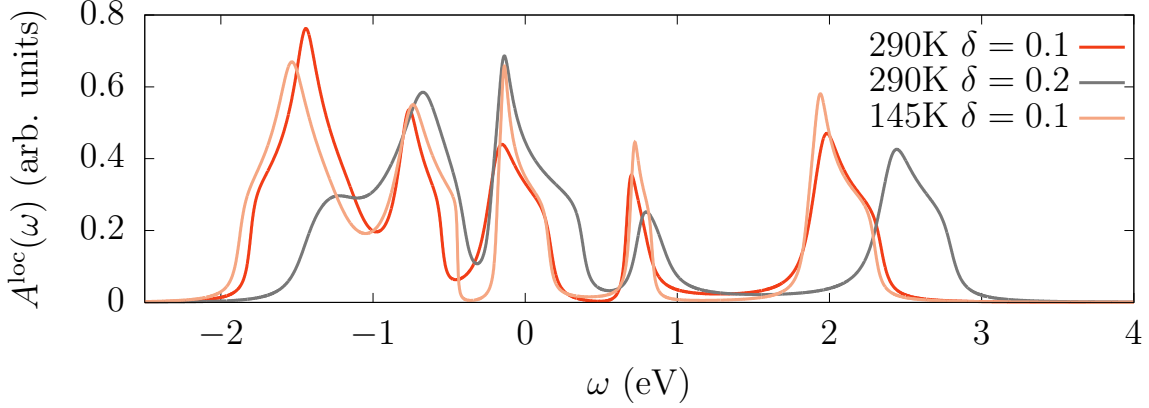


Figure 4.5.: The local spectral function computed by Equation (4.14) employing ED and Padé approximation. The three spectra correspond to one variation in doping δ and one in temperature.

(ii) The lower Hubbard band around $-U/2 = -1.25$ has more weight towards the Fermi surface at $\delta = 0.2$. (iii) The spectral weight at $\omega = 0$ is larger for $\delta = 0.2$ in magnitude and width. This so-called quasiparticle peak is due to local spin-flip processes, i.e. the Kondo-effect. As more scattering events of that kind appear close to half-filling the life time of quasiparticles is shorter and their effective mass larger for $\delta = 0.1$. All these effects are to be expected from a system of increasing hole doping, where consequently the remaining electrons can move around more easily as they become more diluted.

Decreasing the temperature to half its original value increases the lifetime of the quasiparticle, while leaving the bands stationary. However, while the electronic peaks get broader and even lose height, the hole-like peaks get more pronounced and gain height.

When comparing Figure 4.5 with spectra of the dp -model model at half-filling ([29] Figure 2), we observe qualitatively similar features. There are four peaks of similar shape and arrangement. The main difference is the energy range and the position of the chemical potential, $\omega = 0$. The shift in chemical potential in our spectra moves spectral weight to $\omega > 0$, which is consistent with hole-doping the system. Which, htis way, effectively includes the hopping via the oxygen ions by means of the dispersion relation.

Comparing to ARPES measurments ([82] Figure 2) shows that the overdoped spectra has a sharper peak just below the Fermi surface, which corresponds to $\delta = 0.2$ in Figure 4.5, as opposed by the underdoped case $\delta = 0.1$. While the overall effect of doping shows good agreement with the experimental trends, the DMFT result has the evident lack of momentum dependence. Therefore, the pseudogap can not accounted for.

4.1.2. DGA

For the dynamical vertex approximation (DGA) a ladder approximation scheme was

4. Results

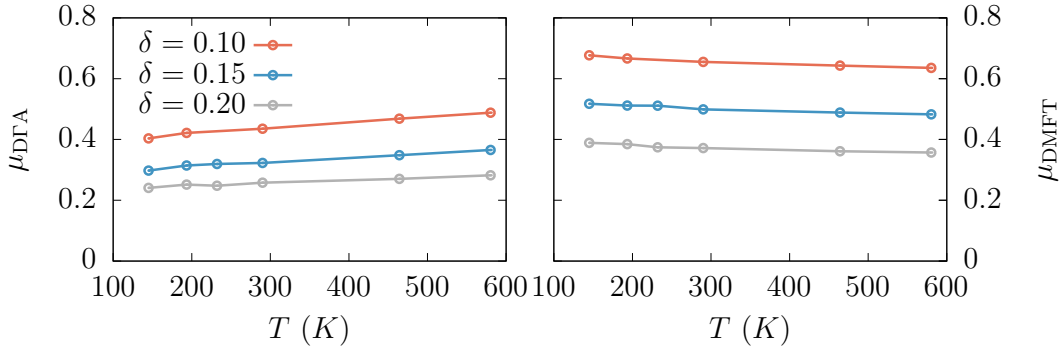


Figure 4.6.: The chemical potential as a function of temperature for three doping levels δ by means of DGA (left) and DMFT (right).

employed in the particle-hole channel, as discussed in Section 3.2.2. The self-energy is momentum dependent and includes non-local fluctuations of particle-hole ladder type processes at all length scales.

In our procedure, the Fermi surface is first computed by setting

$$-\epsilon_{\mathbf{k}} + \mu - \text{Re}\Sigma_{\mathbf{k},\nu \rightarrow 0} = 0. \quad (4.16)$$

This corresponds to finding the equipotential surface of the effective dispersion $\epsilon_{\mathbf{k}} + \text{Re}\Sigma_{\mathbf{k},\nu \rightarrow 0}$ at the level of the chemical potential μ . The chemical potential is iteratively determined by imposing the desired filling for the DGA Green's function,

$$G_{\mathbf{k}} = [i\nu - \epsilon_{\mathbf{k}} + \mu - \Sigma_{\mathbf{k}}]^{-1}, \quad (4.17)$$

where $\Sigma_{\mathbf{k}}$ is given by Equation (3.33b). A simple bisection method is applied to test which μ fulfills Equation (B.32),

$$\langle \hat{n} \rangle = \frac{1}{N_{\mathbf{k}}} \sum_{\mathbf{k}} \frac{1}{\beta} \sum_n e^{-i\nu_n 0^-} G_{\mathbf{k}}, \quad (4.18)$$

as shown in Section B.2.

In Figure 4.6 the chemical potential of DGA (left, μ_{DGA}) is juxtaposed with the chemical potential of DMFT (right, μ_{DMFT}), i.e. the energy level of the impurity in Equation (3.9). As expected, we observe a decrease in the chemical potential with increasing hole doping. The value is stable and remains approximately constant in temperature. We can identify a general trend of a lower value of μ_{DGA} compared to μ_{DMFT} .

In Figure 4.7 the Fermi surface is shown for selected values of temperature and doping. The upper row ($T = 290$ K) displays a *hole-like* Fermi surface, which refers to the curvature of the arcs. Increasing the hole doping (from left to right) decreases the enclosed area. This is a confirmation that the amount of filled states decreases and hence the electron filling is reduced. Let us highlight two points in the Brillouin zone: The nodal point is the point on the Fermi surface in $(\frac{\pi}{2}, \frac{\pi}{2})$ -direction (red arrow). The

4. Results

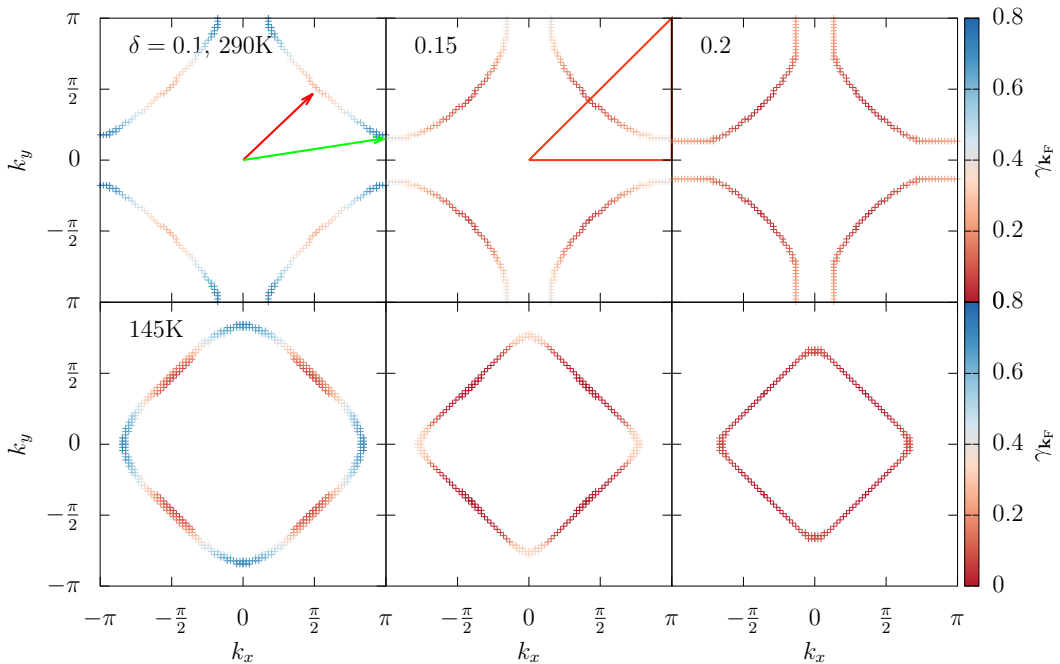


Figure 4.7.: The Fermi surface for three doping levels $\delta = 0.1, 0.15$ and 0.2 at two temperatures 290 K and 145 K corresponding to ladder D Γ A. Red (green) arrow points towards the nodal (antinodal) point.

anti-nodal point (green arrow) is the point closest to the $(\pi, 0)$ -direction, that lies on the Fermi surface.

The second row in Figure 4.7 ($T = 145$ K) is a *closed electron-like* Fermi surface. However we observe slight tendencies towards hole-like curvature near the nodal points for $\delta = 0.1$ and 0.15 . Exactly these hole-like regions are visible in ARPES spectra. This phenomenon may cause the temptation to expect a hole-like Fermi surface. Note that the anti-nodal points are dark in ARPES and it might be therefore difficult to classify, whether the Fermi surface are hole or electron-like at $\delta = 0.1$ for low temperatures. In the over-doped region, on the other hand, ARPES measurements of the whole Fermi surface are available. Our D Γ A results are in qualitative agreement with an electron-like Fermi surface result, which was observed [83] in the over-doped region.

Analogously to the DMFT results discussed in the previous section, we aim at extracting the T -dependence of the quasiparticle scattering rate $\gamma_{\mathbf{k}_F} = -\text{Im}\Sigma(\omega = 0, \mathbf{k}_F)$. To this end, the self-energy Σ_k is analytically continued for each \mathbf{k} -point on the Fermi surface. Here, again we follow a procedure for the Padé approximation by randomly choosing amongst the first 12 – 40 data points and assure the self-energy to be analytical in the upper complex plane, i.e. to have no poles. We tried to additionally enact analyticity of the Green's function at each \mathbf{k} -point. Due to the non analyticity induced

4. Results

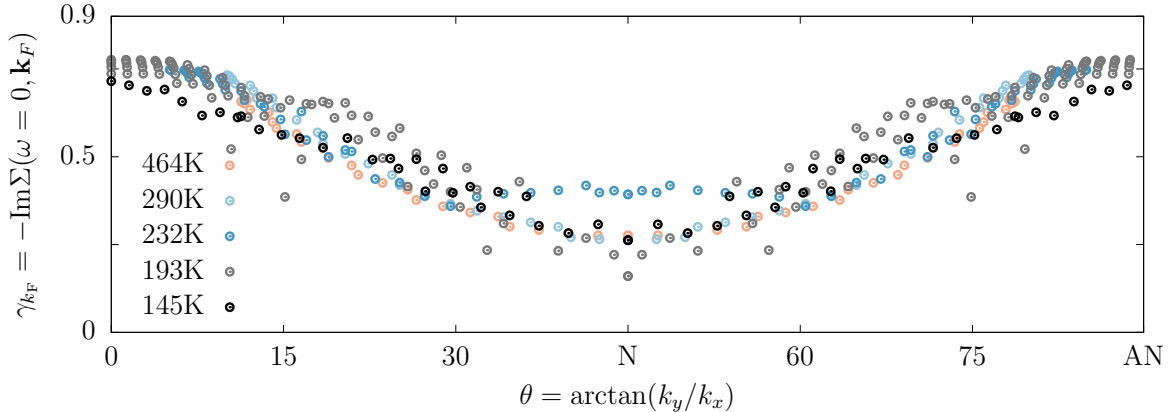


Figure 4.8.: The preliminary angle-resolved scattering rate for doping $\delta = 0.1$ at different temperatures as computed by ladder D Γ A in the ph -channel.

by the λ -correction, only the analyticity of the *local* Green's function is a good constraint to select a physical continuation of the Matsubara data. Hence, there was no further criterion adopted to discriminate between different results of the fitting procedure and we obtain between 0 and 1500 possible fits. The resulting scattering rate is averaged and its variance computed.

In Figure 4.7, the color bar displays the result for $\gamma_{\mathbf{k}_F} = -\text{Im}\Sigma(\omega = 0, \mathbf{k}_F)$ extracted from Padé fits. We observe the system to be more metallic (red color in the plot) for higher hole-doping (left to right) due to a lower scattering rate. Furthermore, we observe a strong differentiation between the nodal (red arrow) and the anti-nodal (green arrow) direction for $\delta = 0.1$ and slightly for $\delta = 0.15$. This is consistent with experiments that show an increasing suppression of spectral weight towards the anti-nodal point for lower doping. Hence the nodal point is observed to be metallic and a spectral gap opens in the direction of the anti-nodal point. The spectral gap is experimentally observed to be maximal at the anti-nodal point.

The momentum dependence of the scattering rate is particularly strong approaching the antiferromagnetic phase. In order to emphasize this, the scattering rate $\gamma_{\mathbf{k}_F}(\theta)$ for doping $\delta = 0.1$ is shown in Figure 4.8. Here, $\theta = \arctan(\frac{k_y}{k_x})$ is the angle in the center of the Brillouin zone, which spans from the anti-nodal point (closest to 0° , AN) to the nodal point (45° , N) and symmetrically extends to the next anti-nodal point towards 90° .

We shall ask: To what extent is the pseudogap behaviour of the cuprate spectra captured by ladder D Γ A? The significant increase of the scattering rate towards the anti-nodal point represents a promising trend, as it resembles the experimental observation of the pseudogap regime by means of ARPES. Let us discuss further features characterizing the pseudogap.

In a recent 2016 Nature Communications publication Chan *et al.* declared commensurate antiferromagnetic excitations as a *signature of the pseudogap* [84] in Hg-1201. In contrast, YBCO and LSCO compounds feature incommensurate antiferromagnetic fluc-

4. Results

tuations within the pseudogap region. Yet, it is claimed that the dominant pseudogap behaviour is most apparent in Hg-1201 due to its structural simplicity, see Ref. [84]. The results were obtained by means of neutron-scattering and by analyzing the dynamic susceptibility.

In order to compare our numerical results to this experimental result we would need to compute the physical spin susceptibility

$$\chi_s^{\text{phys}}(\omega_n = 0, \mathbf{q}) = 2 \int_0^\beta d\tau \langle \hat{\mathcal{S}}_z(\tau, \mathbf{q}) \hat{\mathcal{S}}_z(0, -\mathbf{q}) \rangle, \quad (4.19)$$

$$\hat{\mathcal{S}}_z(\tau, \mathbf{q}) = \frac{1}{2} [\hat{n}_{\mathbf{q}\uparrow}(\tau) - \hat{n}_{\mathbf{q}\downarrow}(\tau)], \quad (4.20)$$

where \mathbf{q} is the momentum. The maximum of the physical spin susceptibility is located at a specific momentum $\mathbf{q} = \mathbf{Q}_s = (\pi - \tilde{q}, \pi - \tilde{q})$, with $\tilde{q} = 0$ for *commensurate* and $\tilde{q} \neq 0$ for *incommensurate* antiferromagnetic fluctuations. $\hat{\mathcal{S}}_z$ is the spin operator and $\hat{n}_{\mathbf{q}\sigma}(\tau) = \sum_{\mathbf{x}} e^{-i\mathbf{q}\mathbf{x}} \hat{c}_{\mathbf{x}\sigma}^\dagger(\tau) \hat{c}_{\mathbf{x}\sigma}(\tau)$ the Fourier transformation³ of the density operator with spin σ .

Aiming at computing the physical susceptibility, we employ the generalized susceptibility calculated by the ladder D Γ A algorithm, as given in Equation (3.14b), and sum over all fermionic degrees of freedom

$$\chi_{s,\mathbf{q}}^\omega = \frac{1}{\beta^2} \sum_{\nu\nu'} \sum_{\mathbf{k}\mathbf{k}'} \chi_{s,\mathbf{k}\mathbf{k}'\mathbf{q}}^{\nu\nu'\omega}. \quad (4.21)$$

Note that $\omega = \omega_n = \frac{\pi}{\beta} 2n$ is the bosonic Matsubara frequency here. Only for $\omega_n = 0$ Equation (4.21) recovers the static limit [69] with direct physical meaning. In fact, $\chi_{s,\mathbf{q}}^{\omega=0}$ corresponds to the thermodynamic response function which describes the response of the system to an external time independent perturbation whose spatial structure is described by \mathbf{q} , without the necessity of analytic continuation.

In Figure 4.9 the static spin susceptibility computed in D Γ A is plotted for all temperatures and doping levels considered. Recall that for doping $\delta = 0.1$ (left panel) the system is in the pseudogap phase. We clearly observe that $\chi_s(i\omega_n = 0, \mathbf{q} = (\pi, q_y))$ is peaked with a maximum at $q_y = \pi$, thus $\tilde{q} = 0$. In other words, the system, according to D Γ A, displays commensurate antiferromagnetic fluctuation within the pseudogap phase. This is consistent with the experimental observation by Chan *et al.* [84]. For doping $\delta = 0.15$ and 0.2 (middle and right panel) incommensurate antiferromagnetic fluctuations emerge instead. As expected these fluctuations are much weaker; note the scale.

As discussed for Equation (3.27), the function $\chi_s(i\omega_n = 0, \mathbf{q} = (\pi, q_y))$ is of the general form

$$\chi_s(i\omega_n = 0, \mathbf{q} = (\pi, q_y)) = \frac{A}{4 \sin^2(q_y - (\pi - \tilde{q})) + \xi^{-2}}, \quad (4.22a)$$

$$\approx \frac{A}{(q_y - (\pi - \tilde{q}))^2 + \xi^{-2}}, \quad \text{for } (q_y - (\pi - \tilde{q})) \ll 1. \quad (4.22b)$$

³Defined in Section C.3.

4. Results

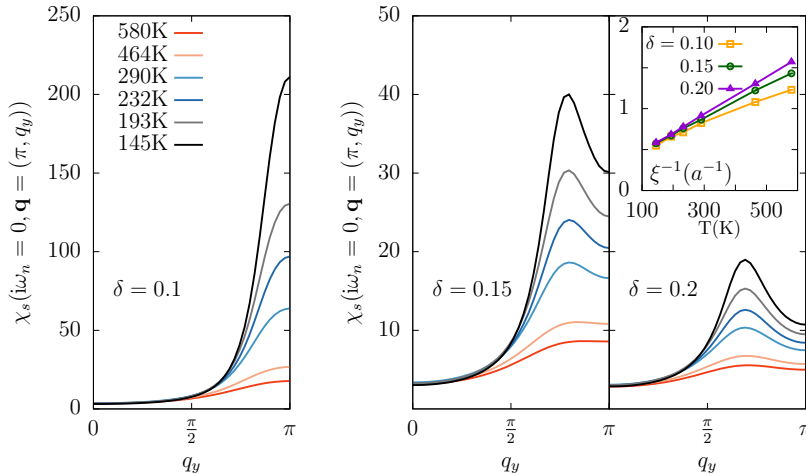


Figure 4.9.: The static spin susceptibility $\chi_s(i\omega_n = 0, \mathbf{q} = (\pi, q_y))$ as a function of the momentum component q_y . Three panels correspond to three doping levels $\delta = 0.1, 0.15$ and 0.2 , which is underdoped, optimally doped and overdoped, respectively. Inset: Temperature dependence of the correlation length ξ as obtained by fitting to $\chi_s(i\omega_n = 0, \mathbf{q} = (\pi, q_y))$ for all three doping levels.

Here A is an arbitrary real constant and ξ is the correlation length. We measure length in units of the lattice constant $a = 1$.

By means of a simple least square fit we extracted the correlation length as a function of temperature for each doping, c.f. Figure 4.9 (Inset). By closer inspection, we note that $\xi^{-1} \propto T^{\tilde{\nu}}$ changes the exponent $\tilde{\nu}$ in the intermediate temperature regime w.r.t. different doping. We stress that this is not critical behaviour, as we are not close to a phase transition and in our two dimensional system there *cannot* occur a magnetic (SU(2)) phase transition at finite temperature due to the Mermin Wagner theorem. By keeping in mind that $\tilde{\nu}$ is not a critical exponent and that ξ would exponentially grow with β for sufficiently low temperature, at least if the ground state is magnetically ordered, we note that in the temperature regime considered $\tilde{\nu} = 1$ appears to be working well for $\delta = 0.2$. $\tilde{\nu}$ decreases when approaching half-filling⁴: $\tilde{\nu} \approx 0.85$ for $\delta = 0.15$ and $\tilde{\nu} \approx 0.73$ for $\delta = 0.1$.

Let us recall our objective. We would like to understand to what extent the pseudogap behaviour is captured. Although we have observed some crucial indicators of the pseudogap phase, including enhanced scattering towards the antinodal point and commensurate antiferromagnetic fluctuations, the underlying concept of a pseudogap remains the selective suppression of spectral weight along the Fermi surface.

⁴ $\tilde{\nu} \approx 0.5$ at half-filling. The behaviour at half-filling, at sufficiently high temperature, is unpublished and not shown here. The data at half-filling has been obtained during a different project by Thomas Schäfer and we mention it here without claiming it is seen in the presented results. We only want to point out a trend we have observed without knowing what we could infer from it.

4. Results

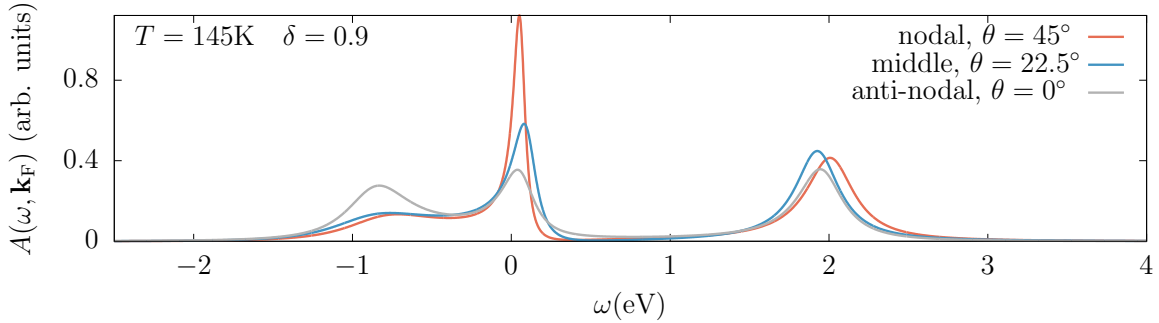


Figure 4.10.: The angle-resolved ladder DGA spectral function obtained by the automated Padé procedure described in Section 3.3 at temperature $T = 145$ K and doping $\delta = 0.1$ for three different Fermi momenta: nodal, anti-nodal and in the middle of the former two.

Figure 4.10 shows the spectral function obtained by analytical continuation by means of Padé approximation at $T = 145$ K and $\delta = 0.1$ for three exemplary Fermi momenta. The nodal point displays the experimentally expected features. Specifically, there is an upper Hubbard band at approximately 2 eV and a lower Hubbard band at approximately -0.5 eV. This is consistent with the expected separation by the distance U . A robust quasiparticle peak arises directly at the Fermi surface.

The spectral function “middle” in Figure 4.10, which is at the Fermi momentum half-way towards the anti-nodal point starting from the nodal point, observes a severe damping of the quasiparticle peak. We would expect a small spectral weight just above the Fermi surface and a dip with $A(\omega = 0, \mathbf{k}_F) \rightarrow 0$ from the viewpoint of a doped Mott insulator [85], as well as by experimental observations [86] on various cuprates by means of scanning tunneling spectroscopy. Although the scattering at $\omega = 0$ in Figure 4.10 is clearly enhanced when approaching the anti-nodal point, no unoccupied low-energy band develops according to our Padé based analytic continuation of the DGA data.

There have been previous cluster DMFT (CDMFT) calculations that are able to reproduce the spectral weight just above the Fermi surface. By means of an effective single-band $t - J$ model [85,87] and by means of the same effective single-band Hubbard model [88] with slightly different parameters⁵; $U = 8t$, $t = 0.3$ eV, $t' = 0.2t$, $t'' = 0$. At a lower doping ($\delta = 0.05$) than that considered here the pseudogap was predicted to emerge between 192 K and 288 K.

This previous literature results offers insight, in what way the pseudogap phenomenon is observable even in the Matsubara data, enabling us to take a first step by comparing our results without the considerable uncertainty introduced by analytic continuation.

In Figure 4.11, the imaginary part of the self-energy on the Matsubara axis at $T = 145$ K and doping $\delta = 0.1$ is shown. The plots correspond to four different momenta on the Fermi surface under the angle $\theta = \arctan(k_y/k_x)$. For the nodal direction with $\theta = 45^\circ$ we observe a Fermi liquid-like linear regime for small Matsubara frequencies $i\nu$.

⁵Our parameters are $U = 2.5$ eV, $t = 0.25$ eV, $t' = 0.05$ eV, $t'' = 0.025$ eV.

4. Results

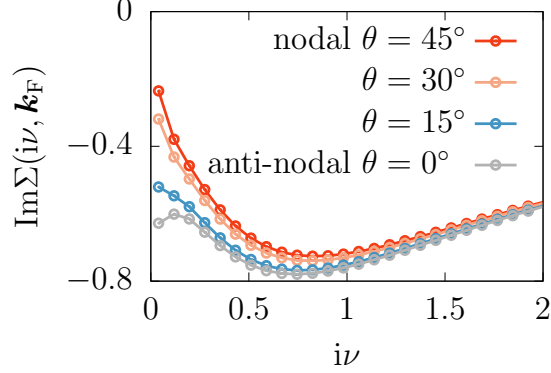


Figure 4.11.: The imaginary part of the self-energy at $T = 145$ K and doping $\delta = 0.1$ for different momenta on the Fermi surface. The angle is given by $\theta = \arctan(k_y/k_x)$.

For $\theta = 30^\circ$ optical inspection suggests that the scattering rate $\gamma_{\mathbf{k}_F} = -\text{Im}\Sigma(i\nu \rightarrow 0, \mathbf{k}_F)$ slightly increases, while the linear behaviour persists. Towards the anti-nodal point, for $\theta = 15^\circ$ and 0° , the scattering rate is strongly enhanced. At the anti-nodal point the sign of the slope changes. This indicates the complete break-down of the perturbative regime and renders the attempt to define a quasi-particle mass impossible.

The behaviour shown in Figure 4.11 is qualitatively the same observed in CDMFT calculations, where a pseudogap is clearly observed. It suggest that our implementation of an automatic evaluation by means of the Padé approximation scheme tends to reject analytic continuations that would display the pseudogap in the spectral function. It happens because among the all trials for $\mathbf{k} \approx_{\text{AN}}$ the ones that consider the Matsubara frequencies close to zero result in on Green's functions with poles in the upper complex plane. These analytic continuations lack analyticity, however in fact the lowest Matsubara frequencies are crucial for describing the pseudogap behaviour.

Since the automatic evaluation by Padé approximation fails, even the scattering rate shown in Figure 4.8 should be questioned, as it could represent an underestimation of the true scattering rate. We will thus follow two strategies in order to obtain more reliable results: (i) We analyze $G(\tau = \beta/2)$ to try to entirely circumvent the necessity of an analytic continuation, and (ii) we employ a more modern approach, namely sparse modeling [89], to the problem of analytic continuation by means of an open package.

Let us start by motivating how $G(\tau = \beta/2)$ can be interpreted. The spectral function is given by⁶

$$A(\omega, \mathbf{k}) = -\frac{1}{\pi} \text{Im} \left[\frac{1}{\omega - \epsilon_{\mathbf{k}} + \mu - \Sigma(\omega, \mathbf{k})} \right] \quad (4.23)$$

$$= -\frac{1}{\pi} \frac{\text{Im}\Sigma(\omega, \mathbf{k})}{(\omega - \epsilon_{\mathbf{k}} + \mu - \text{Re}\Sigma(\omega, \mathbf{k}))^2 + (\text{Im}\Sigma(\omega, \mathbf{k}))^2}. \quad (4.24)$$

⁶NB: $\frac{1}{a-ib} = \frac{1}{a-ib} \frac{a+ib}{a+ib} = \frac{a}{a^2+b^2} + i\frac{b}{a^2+b^2}$

4. Results

This is a Lorentzian with maximum at $\omega_{\mathbf{k}} = \epsilon_{\mathbf{k}} - \mu + \text{Re}\Sigma(\omega, \mathbf{k})$. The Fermi surface corresponds to $0 = \epsilon_{\mathbf{k}_F} - \mu + \text{Re}\Sigma(\omega, \mathbf{k})$, which yields a value of the spectral function

$$A(\omega = 0, \mathbf{k}_F) = -\frac{1}{\pi} \frac{1}{\text{Im}\Sigma(\omega = 0, \mathbf{k}_F)}. \quad (4.25)$$

The spectral function at the Fermi level on the Fermi surface is hence inversely proportional to the scattering rate. The Green's function in imaginary time is related to the spectral function by

$$G(\tau) = - \int d\omega \underbrace{\frac{e^{-\omega\tau}}{1 + e^{-\omega\beta}}}_{K(\omega, \tau)} A(\omega). \quad (4.26)$$

The kernel $K(\omega, \tau)$ can be conveniently rewritten as a sech for $\tau = \beta/2$.

$$K(\omega, \tau = \beta/2) = [e^{\omega\beta/2} + e^{-\omega\beta/2}]^{-1} \quad (4.27)$$

$$= \frac{1}{2} \text{sech}(\omega\beta/2) \quad (4.28)$$

Combined with $\int_{-\infty}^{\infty} \text{sech}(x) dx = \pi$, we identify a delta function in the limit of low temperatures, $\delta(\omega) = \lim_{\beta \rightarrow \infty} \frac{\beta}{2\pi} \text{sech}(\omega\beta/2)$. This is used to interpret $G(\tau = \beta/2)$ in terms of the spectral weight at the Fermi level and hence the inverse scattering rate,

$$\frac{\beta}{\pi} G(\tau = \beta/2) = - \int_{-\infty}^{\infty} d\omega \frac{\beta}{2\pi} \text{sech}(\omega\beta/2) A(\omega) \quad (4.29)$$

$$\gamma_{\mathbf{k}_F} = [\beta G(\tau = \beta/2, \mathbf{k}_F)]^{-1}. \quad (4.30)$$

In the last line we used Equation (4.25).

Figure 4.12 (a) shows the scattering rate approximated by means of $G(\tau = \beta/2)$. We present our numerical results for different temperatures at $\delta = 0.1$. Let us first note the qualitative agreement at low temperatures with the results of the analytic continuation, namely the Padé approximation results in Figure 4.8. At the same time, in contrast to the latter, here we can observe a clear temperature dependency of the scattering rate.

In particular, we note that for high temperatures the dependence on the angle $\theta = \arctan(k_y/k_x)$ is small. The spectral weight at the Fermi surface is large, which results in a clearly metallic behaviour for all Fermi momenta and a small scattering rate. With decreasing temperature the θ -dependence becomes more prominent.

The anti-nodal point in Figure 4.12 (a) is almost constant in the scattering rate for lower temperatures, except for the lowest temperature 145 K we have considered, where we see a decrease. This is suspicious and it ought to be analysed whether there is an issue of numerical nature. The nodal point behaves differently. It features a clearly decreasing scattering rate with decreasing temperature.

Two issues are remaining: (i) The approximation in Figure 4.12 given by Equation (4.30) holds an intrinsic temperature dependence, while (ii) the analytic continuation by means of our automatic Padé approximation procedure is not reliable especially

4. Results

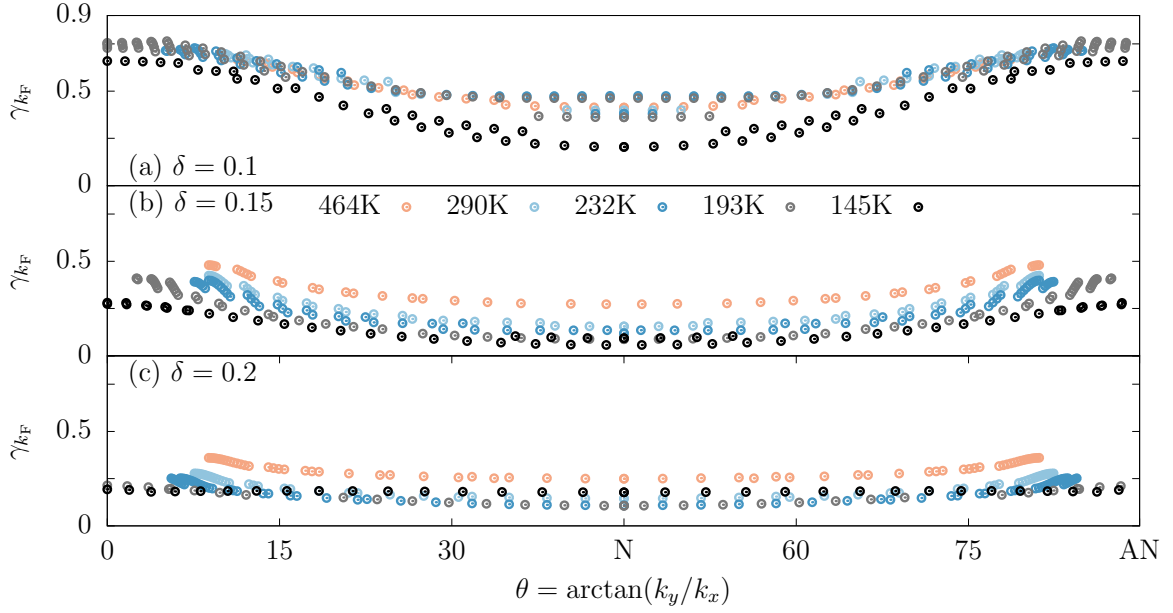


Figure 4.12.: The angle-resolved scattering rate $\gamma_{\mathbf{k}_F} = [\beta|G(\tau = \beta/2, \mathbf{k}_F)]^{-1}$ for doping (a) $\delta = 0.1$, (b) $\delta = 0.15$, and (c) $\delta = 0.2$ at various temperatures extracted from ladder D Γ A in the ph -channel, through Equation (4.30). Note that the Fermi surfaces, e.g. $\delta = 0.1$ with $T \geq 232$ K, are not closed and hence $\max \theta < 90^\circ$.

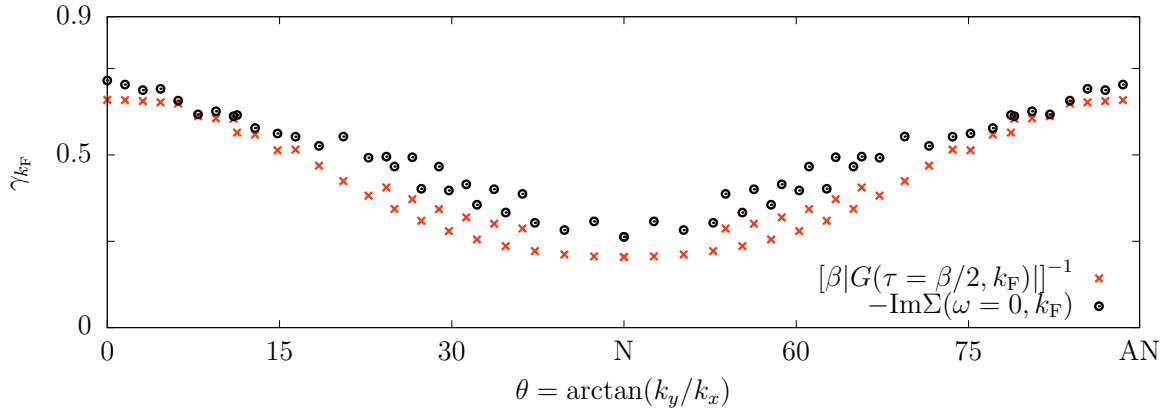


Figure 4.13.: The angle-resolved scattering rate for doping $\delta = 0.1$ at temperature $T = 145$ K computed by means of $G(\tau, \mathbf{k})$ (red crosses) and analytic continuation by means of the automated Padé approximation (black circles).

4. Results

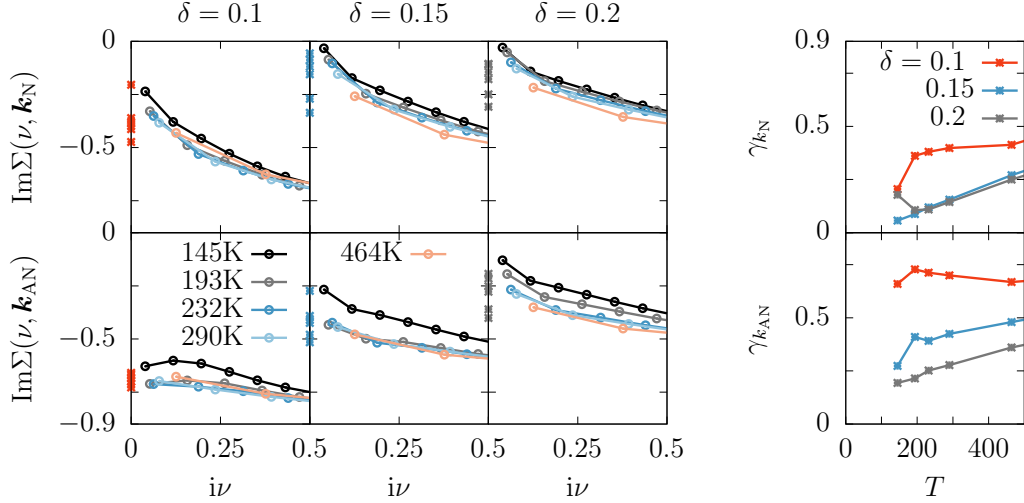


Figure 4.14.: Ladder DΓA result: The imaginary part of the self-energy (left) as a function of Matsubara frequencies in the low frequency regime, and the temperature dependence of the scattering rate (right) approximated by $\gamma_{\mathbf{k}_F} = [\beta|G(\tau = \beta/2, \mathbf{k}_F)|]^{-1}$ at the nodal (top row) and anti-nodal (bottom row). The self-energy is presented for different temperatures at hole-dopings $\delta = 0.1, 0.15$ and 0.2 (left panel: left, center and right column), where $-\gamma_{\mathbf{k}_F} = -[\beta|G(\tau = \beta/2, \mathbf{k}_F)|]^{-1}$ is projected onto $i\nu = 0$ as visual aid.

at the anti-node. This is illustrated in Figure 4.13, where the angle-resolved scattering rate for doping $\delta = 0.1$ juxtaposes the two methods, i.e. (i) and (ii), at the lowest temperature that we have considered. We recall that the error for Equation (4.30), i.e. the error for method (i), should become smaller for low temperatures.

As we have speculated by analyzing the spectral functions in Figure 4.10, the analytic continuation indeed fails to appropriately fit the anti-nodal regime. Also note that the thermal error in Figure 4.12 should tend to always underestimate the scattering towards higher temperatures. It is overestimating, because when β does not go to infinity there is no legit delta function. As a result the spectral weight, assuming it is given by $\beta G(\tau = \beta/2, \mathbf{k}_F)$, is overestimated and thus the scattering rate is underestimated. This may explain the deviation around the nodal region.

In Figure 4.14 (right panel), we show the temperature dependence of the scattering rate $\gamma_{\mathbf{k}_F}$ via Equation (4.30) for the nodal and anti-nodal direction as extracted from Figure 4.12. In the derivation of Equation (4.30) we used the assumption $[\beta|G(\tau = \beta/2, \mathbf{k}_F)|]^{-1} \approx -\text{Im}\Sigma(\nu, \mathbf{k}_F)$. In order to check this assumption, we plot the imaginary part of the self-energy (Figure 4.14 (left panel)) as a function of Matsubara frequencies in the low frequency regime. Furthermore, the value of $-\beta|G(\tau = \beta/2, \mathbf{k}_F)|^{-1}$ is projected onto $i\nu = 0$. Except for $\delta = 0.1$ at the anti-nodal point, we immediately see that the assumption is invalid even without distinguish between the temperatures.

Therefore $G(\tau = \beta/2)$ can only be interpreted as the real frequency integration given in

4. Results

Equation (4.29) and not as the scattering rate. With this limitation the main observation is that the temperature behaviour of Equation (4.29) is not universal. And by optical observation of $\text{Im}\Sigma(\nu \rightarrow 0, \mathbf{k}_F)$, it is likely that it is not universal either.

It remains interesting to compare this result to an approximation that is not affected by an intrinsic temperature dependence. This would ideally be a systematic procedure for the analytic continuation which attains the self-energy and the spectral function on the real axis. Moreover it is our interest to also analyze the spectral function itself. In particular, the θ -dependence of the pseudogap has not been agreed [88] on in the community.

There are several modern approaches to the issue of analytic continuation. One noteworthy approach is sparse modeling (SpM) [89] by J. Otsuki *et al.*. The package is fully documented and the method well explained. We recall that the relation stated in Equation (4.26) shall be inverted. In matrix representation it becomes clear that the kernel needs to be inverted, which is an ill-posed problem due to its small values at large frequencies.

$$\mathbf{G} = \mathbf{K}\mathbf{A}, \quad (4.31)$$

$$G_i \equiv G(\tau_i), \quad (4.32)$$

$$K_{ij} \equiv K(\tau_i, \omega_j), \quad (4.33)$$

$$A_j \equiv A(\omega_j) \Delta\omega. \quad (4.34)$$

A common way to cope with an ill-posed inversion is to introduce some form of regularization. Here it is useful to perform a singular value decomposition (SVD)

$$\mathbf{K} = \mathbf{U}\mathbf{S}\mathbf{V}^t. \quad (4.35)$$

\mathbf{S} is a diagonal matrix with eigenvalues s_l , while \mathbf{U} and \mathbf{V} are orthogonal matrices.

This can be used to rotate into an appropriate basis for the numerical evaluation. SpM now properly defines a cost function by means of a least absolute shrinkage and selection operator (LASSO)

$$\mathbf{A}' = \mathbf{V}^t \mathbf{A}, \quad (4.36)$$

$$\mathbf{G}' = \mathbf{U}^t \mathbf{G}, \quad (4.37)$$

$$C = \underbrace{\frac{1}{2} \sum_l (G'_l - s_l A'_l)^2}_{\chi^2} + \lambda \sum_j |A'_j|. \quad (4.38)$$

The minimization of the cost function corresponds to finding the sparse solution if λ is chosen correctly. The best value for λ must be searched by computing \mathbf{A}' for a given λ_{try} . In turn the first term in the cost function χ^2 is computed as a function of λ_{try} 's. A linear interpolation between the lowest and highest λ_{try} defines a function f . The best λ is identified by a maximum in f/χ^2 .

In Figure 4.15, we show spectral functions computed by SpM at the same points previously shown for the analytic continuation by means of Padé approximation in Figure 4.10. We can identify the similarities w.r.t. the appearance of Hubbard bands. However we encounter the unfortunate event of a missing clear maximum in f/χ^2 .

4. Results

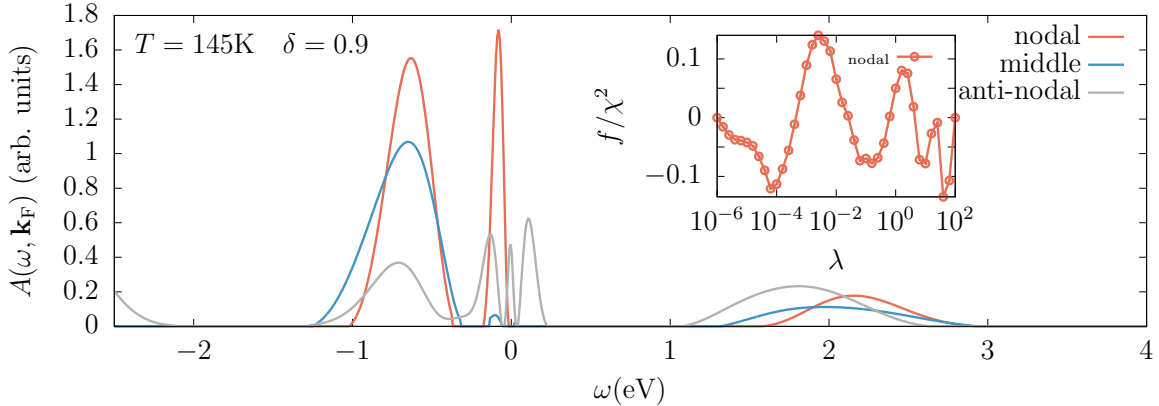


Figure 4.15.: The angle-resolved ladder DΓA spectral function computed by sparse modeling at temperature $T = 145\text{K}$ and doping $\delta = 0.1$ for three different Fermi momenta: nodal, anti-nodal and in the middle of the former two.

Therefore the result in Figure 4.15 is to be regarded with caution. Let us be more specific: The perfectly vanishing spectral function is a condition forced on the result by hand. The nodal point should be the easiest to fit and in fact the spectral weight given by Padé approximation and $\beta|G(\tau = \beta/2, \mathbf{k}_F)|$ show agreement with each other, as seen in Figure 4.13. Therefore, it is quite surprising that the nodal spectral function in Figure 4.15 would show no finite value at $\omega = 0$.

We have tried to obtain a proper fit for other parameters of doping and temperature (not shown). For momenta where we expect less metallic spectra the issues are more severe, however even for higher doping and in particular $\delta = 0.2, T = 145\text{K}$, which is less θ -dependent, we have not obtained acceptable results yet. Further work, and possibly the comparison with other analytic continuation tools is planned.

We close this section by, then, summarizing the most important observations in our numerical results obtained by ladder DΓA in the ph -channel:

- The system shows strong commensurate antiferromagnetic fluctuations for $\delta = 0.1$. For higher hole-doping, $\delta = 0.15, 0.2$, these fluctuations become weaker and incommensurate.
- The temperature dependence of the corresponding correlation length is close but not equal to T^{-1} for $\delta = 0.1, 0.15$. For $\delta = 0.2$ it seems to perfectly agree with T^{-1} .
- The imaginary part of the self-energy on the Matsubara axis clearly shows a strong momentum dependence indicating a qualitative deviation from DMFT. It develops a dip in the low Matsubara frequency range, which is associated with pseudogap behaviour.
- The analytic continuation by both methods, Padé approximation and sparse modeling, show the lower Hubbard band around -0.6eV and the upper Hubbard band

4. Results

at around 1.9 eV. Unfortunately, the automatic evaluation of the Padé approximation by taking into account physical constraints fails. On the other hand, sparse modeling, applied to our D Γ A datasets, has difficulties to find an optimal regularization parameter.

- The approximation $[\beta|G(\tau = \beta/2, \mathbf{k}_F)|]^{-1} \approx -\text{Im}\Sigma(\omega = 0, \mathbf{k}_F)$ seems to be invalid based on a simple visual inspection of $\text{Im}\Sigma(i\nu, \mathbf{k}_F)$ for $i\nu \rightarrow 0$.
- The precise temperature dependence of the scattering rate could not be extracted from our ladder D Γ A results.
- The whole set of data, and especially the non analytically continued data of $\text{Im}\Sigma(i\nu, \mathbf{k}_F)$ appears hardly compatible with an universal behaviour of the scattering rate over the whole phase diagram.

4.1.3. DF

For the dual fermion (DF) calculation a ladder approximation scheme was employed in the dual space, as discussed in Section 3.2.3. The self-energy is momentum dependent and includes non-local fluctuations on all length scales. Here, we will mainly compare the DF results to the dynamical vertex approximation (D Γ A) results, which we discussed in the previous section.

We will begin this section by pointing out that the results here are rather preliminary and should be essentially seen as a preparation for future studies as well as an inspiration for new discussions. It may sound like a disclaimer, but we think the results do not give justice to the dual fermion method yet. Let us highlight some of the issues that arise in our first approach for a comparison:

Firstly, DF is a self-consistent approach in contrast to the ladder D Γ A, which is a one-shot calculation. It is not clear whether, when comparing the two approaches, it is better to only solve the inner self-consistency loop of DF on top of the same Anderson impurity model (AIM) that was used in D Γ A, or to do a full outer self-consistency by updating the AIM. The latter changes the underlying local physics by adjusting the AIM, and hence the underlying “model”. Surely, one argument could be, that the “model” should not be changed to rigorously compare methods and hence a one-shot comparison is best. On the other hand, the more fundamentally underlying model is the 2 dimensional single-band Hubbard model. This model can only be considered solved by DF when doing an outer self-consistency. In our work, we have decided to begin by performing a one-shot comparison. This is numerically less expensive and can be used as a starting point for further discussions.

Secondly, the underlying impurity solver fetches unwanted approximations. In order to start at the same impurity model both methods need to be given the same ingredients. In particular, the full vertex and the one-particle propagator should be computed by the same underlying DMFT calculations. As we have discussed in Section 3.1.2 we employed an exact diagonalization (ED) algorithm. The main reason is that continuous time quantum Monte Carlo (CT-QMC) suffers from high frequency oscillation, that

4. Results

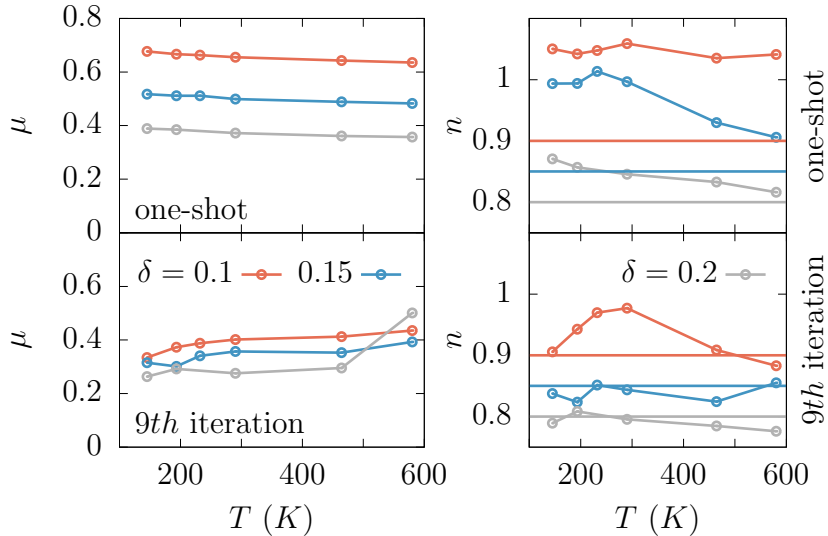


Figure 4.16.: The chemical potential (left) and corresponding filling (right) of the one-shot DF calculation (top) and 9th iteration of updating the AIM (bottom).

DFA could not cope with. Recent CT-QMC developments [66] will allow to overcome this problem in the future.

The DF implementation [78] by H. Hafermann is built on top of a CT-QMC algorithm, which is able to perform full self-consistent calculations without the need of constant attention by the user after each iteration. The main difference between CT-QMC and ED is that the former suffers from statistical errors, while the latter is prone to systematic errors introduced by a finite bath size. We have decided to use the identical full vertex and the one-particle propagator computed by ED, which we used for DFA. The curiosity of how an update of the AIM may affect the system was also studied by us performing 9 outer iterations in DF. We hence stopped without reaching convergence, merely to observe tendencies. Here, we used a somewhat delicate change of the impurity solver by starting from ED and continuing with CT-QMC. Again, it can be seen as a starting point for further discussions.

In Figure 4.16 we plot the chemical potential (left) and the corresponding filling that DF infers (right) for the one-shot calculation (top panels), as well as the 9th iteration of the outer loop (bottom row). The left hand side shows the chemical potential used for the initialization of the hybridization, while the right hand side is the effective filling this corresponds to. The deviation from the desired filling $n = 0.9, 0.85$ and 0.8 for doping $\delta = 0.1, 0.15$ and 0.2 respectively is significant.

We observe a systematic overestimation of the filling in Figure 4.16. In fact, this reaches the extent of being in the effectively electron doped region for the one-shot calculation. The 9th iteration is overall closer to to the desired filling, however this is not sufficiently close either.

The overestimated filling has direct consequences for the Fermi surface. In Figure 4.16 we show exemplary Fermi surfaces at $T = 290$ K (top row) and $T = 145$ K (bottom row)

4. Results

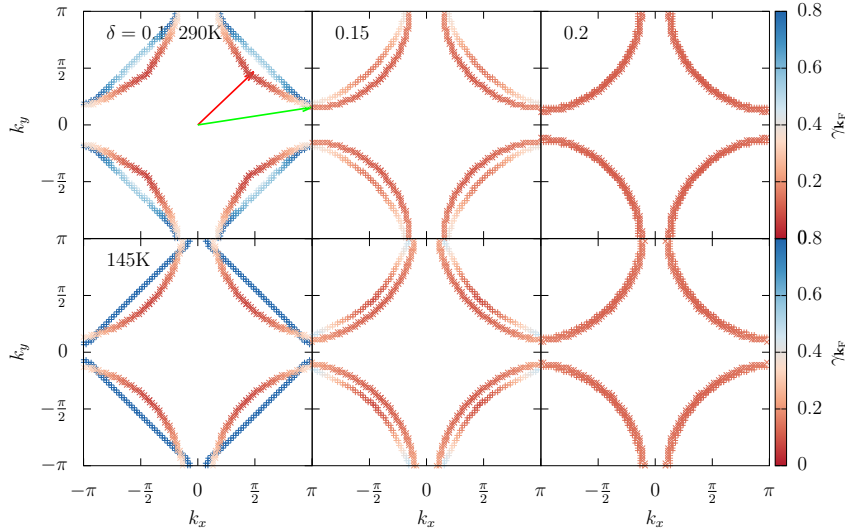


Figure 4.17.: DF results: Fermi surface at $T = 290$ K (top row) and $T = 145$ K (bottom row) for all doping levels $\delta = 0.1, 0.15$ and 0.2 . The larger surface with higher scattering and lower curvature is a one-shot DF calculation, while the smaller Fermi surface in each panel is the 9^{th} iteration of updating the AIM. For $\delta = 0.2$ the two Fermi surfaces overlap.

for all doping levels $\delta = 0.1, 0.15$ and 0.2 . Here, the larger surface with higher scattering rate and lower curvature corresponds to the one-shot calculation. Compared to D Γ A and experimental observations it is surprising that we do not observe any closed Fermi surfaces. Furthermore we observe that the Fermi surface of the highest doping is almost identical for one-shot DF and the 9^{th} iteration. It confirms that external self-consistent DF does not introduce significant corrections when the system is less correlated. When comparing all results, D Γ A, one-shot DF and the 9^{th} iteration, the volume enclosed by the Fermi surface varies significantly. On one hand, this may be due to the unstable “effective” filling the algorithm used, and on the other hand, Luttingers theorem does not apply because of the finite temperature and the strongly momentum dependent scattering.

The most important quantity we would like to compare is the temperature dependence of the scattering rate. However already during the analysis of the D Γ A results we encountered severe limitations. The analytic continuation of our preliminary DF data appears even more problematic than for D Γ A. So the only possible comparison we can engage in is to juxtapose $\beta|G(\tau = \beta/2, \mathbf{k}_F)|$ of DF with D Γ A.

Figure 4.18 shows the temperature dependence of $\beta|G(\tau = \beta/2, \mathbf{k}_F)|$ at specific momenta on the Fermi surface. The nodal (anti-nodal) point is presented for dopings $\delta = 0.1, 0.15$ and 0.2 in the top (bottom) row. We separately display the DF one-shot calculation (left column), the 9^{th} iteration in the outer loop of DF (center column) and

4. Results

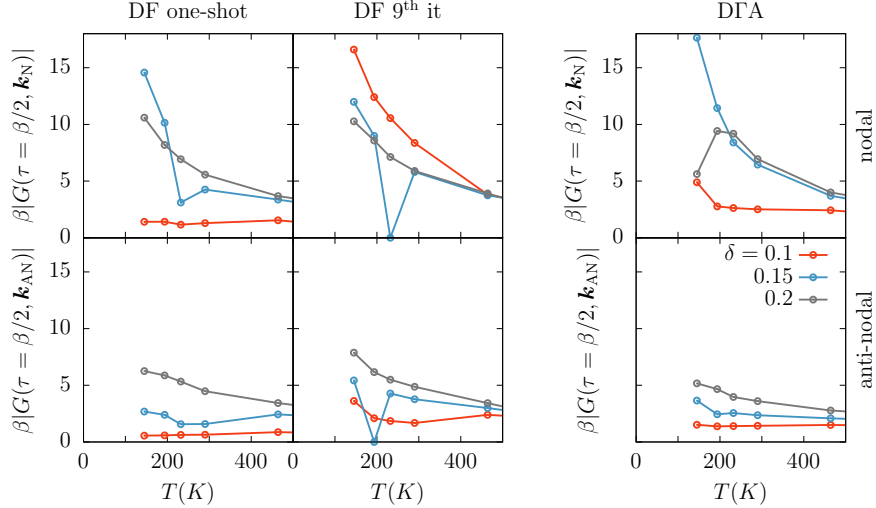


Figure 4.18.: The spectral weight approximated as the value of $\beta|G(\tau = \beta/2, \mathbf{k}_F)|$ for three dopings $\delta = 0.1, 0.15$ and 0.2 as a function of temperature. The upper panel compares DF one-shot calculations with DGA results, while the lower panel shows the *9th* iteration of updating the AIM (not converged). The panels show the nodal direction (left), the anti-nodal direction (middle) and the value of the local Green's function (right).

the DGA results (right column).

We can make only few observations here. The qualitative agreement between DF one-shot (left) and DGA (right) is much larger than of either to the *9th* iteration DF results. An overall similarity between DF one-shot and DGA is found when comparing the order of the magnitude of $\beta|G(\tau = \beta/2, \mathbf{k}_F)|$ w.r.t. doping at any temperatures. We notice that there are some outliers in the DF results, which may be slips of a numerical nature. On the other hand, the DGA results show sudden changes in the low temperature regime for $\delta = 0.1$ and 0.15 , which are likely to be artifacts arising due to the limited bath size in ED-DMFT in conjunction with DGA.

The *9th* iteration DF results bare little resemblance with anything we have observed so far and is not converged. The only tendency we may guess, is that at low doping the iterated AIM is far from where we started. It is unclear, at the moment, whether it is due to the changed impurity solver, to a poor statistics or because DF would obtain a radically different result with the external self-consistency.

For the sake of completeness, we present the full θ -dependence of $[\beta|G(\tau = \beta/2, \mathbf{k}_F)|]^{-1}$ in Figures 4.19 to 4.21. The figures separately show the doping $\delta = 0.1, 0.15$ and 0.2 , respectively. The top panel corresponds to our one-shot and the bottom row to our *9th* iteration DF calculation. We would have to point out that the scale of the y -axis for different dopings is not fixed. This is necessary in order to visually detect temperature dependent changes.

The reader may also notice that we have not shown the spin-susceptibility and the

4. Results

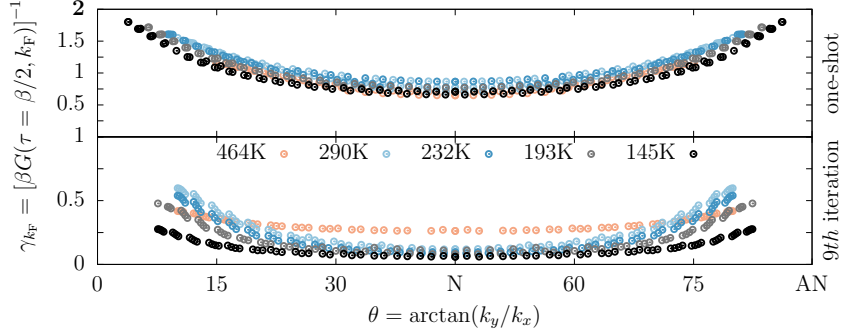


Figure 4.19.: The angle-resolved scattering rate for doping $\delta = 0.1$ at different temperatures as computed by DF.

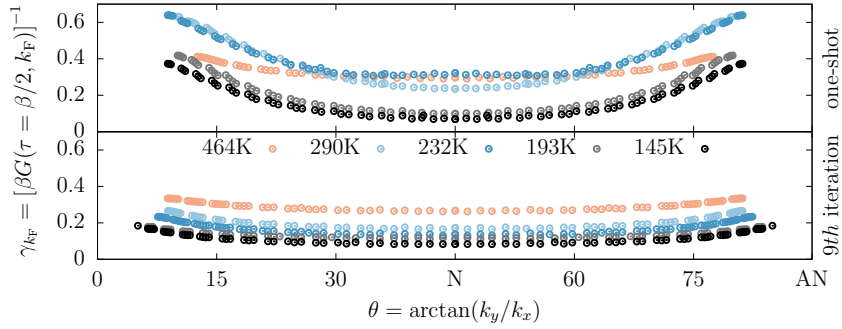


Figure 4.20.: The angle-resolved scattering rate for doping $\delta = 0.15$ at different temperatures as computed by DF.

associated correlation length. This and other topics such as a converged fully self-consistent calculation are reserved for a future investigation. A more detailed outlook in this regard will be given in Chapter 5.

We close this section by comparing the most important observations w.r.t. our numerical results obtained by DF in a one-shot calculation and in the $9th$ iteration (not converged). We focus here on a comparison with ladder D Γ A: Although for the one-shot calculation the anti-nodal behaviour qualitatively agrees for both methods, DF and D Γ A yield different magnitude for $\beta|G(\tau = \beta/2, \mathbf{k}_F)|$ for all temperatures. The nodal point shows even qualitative deviations between DF and D Γ A in the low energy regime. Furthermore some DF results seem to be outliers. The DF one-shot calculation, however, is not robust when performing further iterations. The large change throughout the 9 iteration steps we computed, suggests that the one-shot calculation is far a way from the converged DF solution of this system. In this respect it is important to recall that the one-shot DF and D Γ A results feature more similarities, than the $9th$ iteration of DF with either.

4. Results

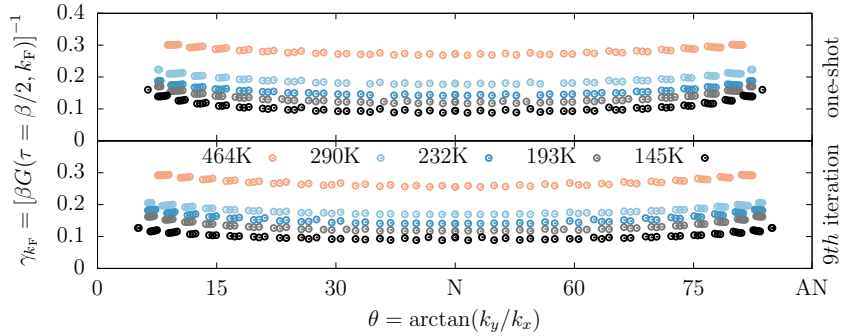


Figure 4.21.: The angle-resolved scattering rate for doping $\delta = 0.2$ at different temperatures as computed by DF.

4.2. The ratio ρ/ρ_H

We recall that $\rho/\rho_H \hat{=} \sigma_{xx}/\sigma_{xy}$ shall be computed, cf. Equations (4.1) and (4.2). Hitherto, we set the focus on the temperature dependence of the scattering rate. However, we are aiming to describe an—in principle different—aspect of the whole phase diagram of cuprates, (depicted in Figure 1.4). The experimental results [1] obtained by N. Barišić et al. at TU Wien, which reveal a surprising universal behaviour of $\rho/\rho_H \propto T^2$. In this section we try to identify many-body expressions, which can be employed to, in the future, extend numerical results to the direct calculation of ρ/ρ_H .

Here, we mostly follow H. Kontani [90], who aims to describe transport phenomena in strongly correlated Fermi liquids. Starting point of this discussion is Kubo's linear response theory [91]. We consider the first-order response w.r.t. an external perturbation $f(t)$ that couples to an operator \hat{A} of the system. The time-dependent Schrödinger equation can be solved by means of an ansatz

$$i\frac{\partial}{\partial t}|\Psi(t)\rangle = [H + V(t)]|\Psi(t)\rangle, \quad (4.39)$$

$$V(t) = \int d^3x \hat{A}f(t), \quad (4.40)$$

$$|\Psi(t)\rangle = a(t)e^{-iHt}|\Phi\rangle. \quad (4.41)$$

H is the Hamiltonian of the system without an external perturbation, $V(t)$ is the time-dependent potential that linearly couples to the external perturbation⁷. In the ansatz for the eigenstate $|\Psi(t)\rangle$ an unknown amplitude $a(t)$ enters, as well as the initial state $|\Phi\rangle$ of the unperturbed system.

By solving the differential equation for $a(t)$, we find

$$|\Psi(t)\rangle = e^{-iHt}|\Phi\rangle - ie^{-iHt} \int_0^t dt' V^{\text{Heis}}(t')|\Phi\rangle + \mathcal{O}(V^2), \quad (4.42)$$

$$V^{\text{Heis}}(t) = e^{iHt}V(t)e^{-iHt}. \quad (4.43)$$

⁷We used $\hbar = 1$.

4. Results

As a next step, we perform the measurement of some operator \hat{B} of the system. This is expressed by the Kubo formula in its general form, which reads

$$\begin{aligned} \langle \hat{B} \rangle &= \int dx' \int dt' i \langle [\hat{A}, \hat{B}] \rangle_0 \Theta(t-t') f(t), \\ \langle \dots \rangle_0 &= \langle \Phi | \dots | \Phi \rangle, & T = 0 \\ \langle \dots \rangle_0 &= \text{Tr}\{e^{-\beta H} \dots\} / \text{Tr}\{e^{-\beta H}\}, & T > 0. \end{aligned} \quad (4.44)$$

As is known, it describes the expectation of \hat{B} in the perturbed system in terms of the unperturbed system only.

Let us now apply Equation (4.44) to the measurement of DC resistivity and Hall resistivity, as discussed in Section 1.2. Here the time-dependent external perturbation is set to an adiabatically alternating field $f(t) = E_\alpha e^{-i\omega t + \eta t}$, with $\alpha = x, y, z$. $f(t)$ is adiabatically turned on, which is realized via a tiny $\eta > 0$. The case of a DC measurement is recovered for $\omega \rightarrow 0$.

The external field couples to a misplacement of the charge density, i.e. $\hat{A} = \hat{P}_\alpha = -e \int d^3x \hat{x}_\alpha \hat{n}_\mathbf{x}$. \hat{P}_α is the charge polarization operator of the system. Furthermore, we measure the induced current, which corresponds to taking the expectation value of the current density $\hat{B} = j_\alpha = -e \int d^3x \frac{\partial \hat{x}_\alpha}{\partial t} \hat{n}_\mathbf{x}$. The reader may already notice the subtle similarity in the definition of the current density and the polarization operator.

This is the key for obtaining the Nakano-Kubo formula for the conductivity (Ref. [90] Equation (3.33) - (3.35))

$$\begin{aligned} \langle j_\alpha(x) \rangle &= \int dx' \int dt' (-i) \langle [j_\alpha(x), j_\beta(x')] \rangle_0 \\ &\quad \times \left[\Theta(t-t') \frac{e^{-i\omega t'}}{i\omega} + \Theta(t'-t) \frac{e^{-i\omega t}}{i\omega} \right] eE_\beta, \end{aligned} \quad (4.45a)$$

$$j_\alpha(\omega) = \sum_\beta \sigma_{\alpha\beta}(\omega) E_\beta(\omega), \quad (4.45b)$$

$$\sigma_{\alpha\beta}(\omega) = \frac{e^2}{i\omega} K_{\alpha\beta}^R(\omega), \quad (4.45c)$$

$$K_{\alpha\beta}^R(t) = \lim_{\mathbf{q} \rightarrow 0} -i \int_\infty^0 dt' \langle [j_{\mathbf{q},\alpha}(t), j_{-\mathbf{q},\beta}(t')] \rangle_0 \Theta(t-t'), \quad (4.45d)$$

in Coulomb gauge. Here, $K_{\alpha\beta}^R(\omega) \hat{=} K_{\alpha\beta}(\omega + i\delta)$ is the retarded current-current correlation function, while $\sigma_{\alpha\beta}(\omega)$ is the conductivity tensor.

To establish ties with our numerical calculations, we have to proceed with the thermal correlation function. Hence, instead of Equation (4.45d), we will continue with

$$K_{\alpha\beta}(\omega) = \lim_{\mathbf{q} \rightarrow 0} \frac{1}{\beta} \int_0^\beta d\tau \int_0^\beta d\tau' e^{i\omega(\tau-\tau')} \langle \mathcal{T}_\tau j_{\mathbf{q},\alpha}(\tau) j_{-\mathbf{q},\beta}(\tau') \rangle_0, \quad (4.46)$$

where $\omega = 2\pi n/\beta$ are the bosonic Matsubara frequencies.

Note, that the Hall resistivity can only be measured in the presence of a magnetic field. The analysis of the full conductivity tensor, hence demands a perturbation in

4. Results

both, the electric and the magnetic field. The first approaches [92] in order to include the effects of a magnetic field within the Kubo formalism were made by Kubo himself. He employed the Wigner representation and avoided using a vector potential. It enabled a characterization in terms of “classical” and “quantum-mechanical” corrections, which contribute to the Hall coefficient. However, this approach could not be employed to discuss correlation effects [93].

In 1969 [93,94] H. Fukuyama *et al.* derived an expression for the conductivity in the presence of a uniform magnetic field on the basis of diagrammatic techniques. In their derivation a uniform magnetic field $\mathbf{H} = i\mathbf{q} \times \mathbf{A}$ is included in terms of a vector potential $\mathbf{A}_i = \mathbf{A}e^{i\mathbf{q}\cdot\mathbf{x}}$, where the limit $\mathbf{q} \rightarrow 0$ is taken in the final step of the calculation. The vector potential enters the Hamiltonian of our system⁸ by means of a Peierls substitution [95]

$$t_{ij} \rightarrow t_{ij}e^{-ie(\mathbf{A}_i+\mathbf{A}_j)\cdot(\mathbf{x}_i-\mathbf{x}_j)/2}, \quad (4.47a)$$

$$H_{\mathbf{A}} = H - \mathbf{A}(\mathbf{q}) \cdot \mathbf{j}(-\mathbf{q}) + \mathcal{O}(A^2), \quad (4.47b)$$

$$j_{\alpha}(\mathbf{q}) = -e \sum_{\mathbf{k}\sigma} \frac{\partial \epsilon}{\partial k_{\alpha}} \hat{c}_{\mathbf{k}-\mathbf{q}/2,\sigma}^{\dagger} \hat{c}_{\mathbf{k}+\mathbf{q}/2,\sigma}, \quad (4.47c)$$

Note, that we write the Hamiltonian up to the linear order w.r.t. the vector potential. Hence, the current operator which appears in the second term of Equation (4.47b) is of 0th order in \mathbf{A} .

The observable we measure though is the current operator $j^{\mathbf{A}}$ in the presence of the vector potential up to linear order. It reads (Ref. [90] Equation (3.48) and [93] (2.2))

$$j_{\alpha}^{\mathbf{A}}(\mathbf{q}) = j_{\alpha}(\mathbf{q}) - \sum_{\beta=x,y} A_{\beta}(\mathbf{q}') j_{\beta\alpha}(\mathbf{q} - \mathbf{q}') + \mathcal{O}(A^2), \quad (4.48a)$$

$$j_{\beta\alpha}(\mathbf{q}) \equiv e^2 \sum_{\mathbf{k},\sigma} \frac{\partial^2 \epsilon}{\partial k_{\beta} \partial k_{\alpha}} \hat{c}_{\mathbf{k}-\mathbf{q}/2,\sigma}^{\dagger} \hat{c}_{\mathbf{k}+\mathbf{q}/2,\sigma}. \quad (4.48b)$$

The second line defines an “auxiliary” current operator with two indices.

The derivation in [93,94] ultimately yields an expression for the thermal current-current correlation function, which includes corrections due to the magnetic field up to

⁸Namely the Hubbard model given in Equation (2.1).

4. Results

linear order in \mathbf{A} . It is (Ref. [90] Equation (3.42) - (3.44))

$$\begin{aligned}
K_{\mu\nu}(\omega) &= \lim_{\mathbf{q} \rightarrow 0} \frac{1}{\beta} \int_0^\beta d\tau \int_0^\beta d\tau' e^{i\omega(\tau-\tau')} \langle \mathcal{T}_\tau j_\mu^{\mathbf{A}}(\mathbf{q}, \tau) j_\nu^{\mathbf{A}}(-\mathbf{q}, \tau') \rangle_{\mathbf{A}} \quad (4.49) \\
&= \frac{1}{\beta} \int_0^\beta d\tau \int_0^\beta d\tau' \langle \mathcal{T}_\tau j_\mu(\mathbf{q} = 0, \tau) j_\nu(\mathbf{q} = 0, \tau') \rangle_0 \\
&\quad + \lim_{\mathbf{q} \rightarrow 0} \sum_{\alpha=x,y} A_\alpha \int_0^\beta d\tau \int_0^\beta d\tau' e^{i\omega(\tau-\tau')} \times \\
&\quad \left[-\frac{1}{\beta} \langle \mathcal{T}_\tau j_\mu(\mathbf{q}, \tau) j_{\alpha\nu}(-\mathbf{q}, \tau') \rangle_0 + \int_0^\beta d\tau'' e^{i\omega(\tau-\tau'')} \langle \mathcal{T}_\tau j_\mu(\mathbf{q}, \tau) j_\alpha(-\mathbf{q}, \tau') j_\nu(0, \tau'') \rangle_0 \right] \\
&\quad + \mathcal{O}(A^2). \quad (4.50)
\end{aligned}$$

Note, that these expressions are exact, as long as linear response theory is valid.

The first term in Equation (4.50) is of 0^{th} order in \mathbf{A} and therefore describes the current-current correlation function without the presence of a magnetic field. It is evident, that this term will, in general, only contribute to the diagonal elements of the conductivity tensor. This is based on the principle that within linear response the induced current is parallel to the applied electric field in sufficiently isotropic systems.

The second term in Equation (4.50) is of linear order in \mathbf{A} . It will contribute to the off-diagonal elements of the conductivity tensor. The basis of this is, not surprisingly, that the force of a magnetic field on moving charge is perpendicular to the movement and the field.

In particular, the second term in Equation (4.50) is composed of two parts. On one hand, there is a two particle process which is sensitive to the Fermi surface curvature $\frac{\partial^2 \epsilon}{\partial k_\beta \partial k_\alpha}$, rather than the Fermi velocity $\frac{\partial \epsilon}{\partial k_\mu}$. On the other hand, there is a three particle process.

In order to further familiarize ourself with Equation (4.50), let us first examine the standard example with $\mathbf{H} = 0$ and $\mu\nu = xx$. According to the first term $K_{xx}(\omega)$ without a magnetic field is given by

$$\begin{aligned}
K_{xx}(\omega) &= \frac{1}{\beta} \int_0^\beta d\tau \int_0^\beta d\tau' e^{i\omega(\tau-\tau')} \langle \mathcal{T}_\tau j_x(0, \tau) j_x(0, \tau') \rangle, \quad (4.51) \\
&= \frac{1}{\beta} \int_0^\beta d\tau \int_0^\beta d\tau' e^{i\omega(\tau-\tau')} (-e)^2 \sum_{\mathbf{k}\mathbf{k}', \sigma\sigma'} \frac{\partial \epsilon_{\mathbf{k}}}{\partial k_x} \left\langle \mathcal{T}_\tau \hat{c}_{\mathbf{k}_x \sigma}^\dagger(\tau) \hat{c}_{\mathbf{k}_x \sigma}(\tau) \hat{c}_{\mathbf{k}'_x \sigma'}^\dagger(\tau') \hat{c}_{\mathbf{k}'_x \sigma'}(\tau') \right\rangle \frac{\partial \epsilon_{\mathbf{k}'}}{\partial k'_x}. \quad (4.52)
\end{aligned}$$

In the next step we identify the two particle Green's function and perform the Fourier transformation, yielding

$$\begin{aligned}
G_{\sigma_1 \sigma_2 \sigma_3 \sigma_4}^{(2)}(\tau_1, \tau_2, \tau_3, \tau_4) &= (-1)^2 \left\langle \mathcal{T}_\tau \hat{c}_{\mathbf{k}_1 \sigma_1}^\dagger(\tau_1) \hat{c}_{\mathbf{k}_2 \sigma_2}(\tau_2) \hat{c}_{\mathbf{k}_3 \sigma_3}^\dagger(\tau_3) \hat{c}_{\mathbf{k}_4 \sigma_4}(\tau_4) \right\rangle, \quad (4.53) \\
G_{\sigma_1 \sigma_2 \sigma_3 \sigma_4}^{(2), \mathbf{k}_1 \mathbf{k}_2 \mathbf{k}_3 \mathbf{k}_4}(\tau_1, \tau_2, \tau_3, \tau_4) &= \frac{1}{\beta^4} \sum_{\nu_1 \nu_2 \nu_3 \nu_4} e^{i(\nu_1 \tau_1 - \nu_2 \tau_2 + \nu_3 \tau_3 - \nu_4 \tau_4)} G_{\sigma_1 \sigma_2 \sigma_3 \sigma_4}^{(2), \mathbf{k}_1 \mathbf{k}_2 \mathbf{k}_3 \mathbf{k}_4}(\nu_1, \nu_2, \nu_3, \nu_4). \quad (4.54)
\end{aligned}$$

4. Results

We obtain

$$K_{xx}(\omega) = \frac{2e^2}{\beta^2} \sum_{\mathbf{k}\mathbf{k}',\nu\nu'} \frac{\partial\epsilon_{\mathbf{k}}}{\partial k_x} \underbrace{\left[G_{\uparrow\uparrow\uparrow\uparrow}^{(2),\mathbf{k}\mathbf{k}\mathbf{k}'\mathbf{k}'}(\nu, \nu + \omega, \nu' + \omega, \nu') + G_{\uparrow\uparrow\downarrow\downarrow}^{(2),\mathbf{k}\mathbf{k}\mathbf{k}'\mathbf{k}'}(\nu, \nu + \omega, \nu' + \omega, \nu') \right]}_{G_{c,\nu\nu'\omega}^{(2),\mathbf{k}\mathbf{k}'q=0}} \frac{\partial\epsilon_{\mathbf{k}'}}{\partial k'_x}. \quad (4.55)$$

c denotes the charge channel. We employed the SU(2) symmetry by using $G_{\uparrow\uparrow\uparrow\uparrow}^{(2)} = G_{\downarrow\downarrow\downarrow\downarrow}^{(2)}$ and $G_{\uparrow\uparrow\downarrow\downarrow}^{(2)} = G_{\uparrow\downarrow\uparrow\downarrow}^{(2)}$.

As we have seen in Chapter 3, the two particle propagator can be split in three parts, namely two disconnected and one fully connected part. It reads

$$G_{\sigma\sigma',\mathbf{k}\mathbf{k}'\mathbf{q}}^{(2),\nu\nu'\omega} = \beta G_{\mathbf{k}}(\nu) G_{\mathbf{k}'}\delta_{\mathbf{q}\mathbf{0}}\delta_{\omega\mathbf{0}} - \underbrace{\beta G_{\mathbf{k}}(\nu) G_{\mathbf{k}'+\mathbf{q}}(\nu' + \omega) \delta_{\mathbf{k}\mathbf{k}'} \delta_{\nu\nu'} \delta_{\sigma\sigma'}}_{\chi_{\sigma\sigma',\mathbf{k}\mathbf{k}'\mathbf{q}}^{\nu\nu'\omega}} - G_{\mathbf{k}}(\nu) G_{\mathbf{k}+\mathbf{q}}(\nu + \omega) F_{\sigma\sigma',\mathbf{k}\mathbf{k}'\mathbf{q}}^{\nu\nu'\omega} G_{\mathbf{k}'+\mathbf{q}}(\nu + \omega) G_{\mathbf{k}'}(\nu). \quad (4.56)$$

The expression in Equation (4.56) is used to analyze and motivate approximations for $K_{xx}(\omega)$ in Equation (4.55).

First, we notice that for the single-band case, with the inversion symmetry, $\partial\epsilon_{\mathbf{k}}/\partial k_{\mu}$ is completely antisymmetric w.r.t. \mathbf{k} . Therefore one disconnected part, namely the first term in Equation (4.56), completely vanishes when summing over \mathbf{k} and \mathbf{k}' . It remains the generalized charge susceptibility χ_c in Equation (4.55).

The second term in Equation (4.56) is the disconnected part of the generalized charge susceptibility. It does not vanish when summing over \mathbf{k} and \mathbf{k}' due to the delta function $\delta_{\mathbf{k}\mathbf{k}'}$. After the summation this term is the so-called bubble contribution to $K_{xx}(\omega)$.

Lastly, the third term in Equation (4.56) is the so-called vertex correction. In many materials, though most likely not in cuprates, vertex corrections can be neglected. Neglecting vertex corrections yields the well-known expression, which is often discussed in textbooks

$$K_{xx}(\omega) = -\frac{2e^2}{\beta} \sum_{\mathbf{k},\nu\nu'} \frac{\partial\epsilon_{\mathbf{k}}}{\partial k_x} G_{\mathbf{k}}(\nu) G_{\mathbf{k}}(\nu' + \omega) \frac{\partial\epsilon_{\mathbf{k}}}{\partial k_x}. \quad (4.57)$$

We would like to mention two ways of approximating σ_{xx} building upon Equation (4.57), following e.g. lecture notes by J. Tomczak [96] at TU Wien.

First, we use $\text{Re}\sigma_{xx}(\omega) = [\text{Im}K_{xx}(\omega) - \text{Im}K_{xx}(0)]/\omega$ and take the limit $\omega \rightarrow 0$. The first approximation exploits the full spectral function $A(\mathbf{k}, \omega)$ and reads

$$\sigma_{xx} = e^2 \pi^2 \int d\omega \left(-\frac{\partial f}{\partial \omega} \right) \sum_{\mathbf{k}} A^2(\mathbf{k}, \omega) \left(\frac{\partial\epsilon_{\mathbf{k}}}{\partial k_x} \right)^2. \quad (4.58)$$

f is the Fermi function and yields $\partial f/\partial \omega = -\beta e^{\beta\omega}/(e^{\beta\omega} + 1)^2$. Note, that this is the DC conductivity tensor element as we have taken the limit $\omega \rightarrow 0$, though we omit an additional label.

4. Results

In the limit of a long quasiparticle life time and no momentum dependence, the spectral function can be further approximated. It enables an approximation for the ω integration, which is problematic especially numerically for low temperatures. The momentum independent, low scattering approximation yields

$$\sigma_{xx} = -\frac{e^2\pi^2}{2\pi\text{Im}\Sigma(i\omega \rightarrow 0)} \sum_{\mathbf{k}} \left(-\frac{\partial f}{\partial \omega} \right)_{\omega=\epsilon_{\mathbf{k}}} \left(\frac{\partial \epsilon_{\mathbf{k}}}{\partial k_x} \right)^2. \quad (4.59)$$

In order to connect the simplified expressions used here to a more general formalism, we rewrite the current-current correlation function Equation (4.55) in terms of a current vertex, which is defined via (Ref. [90] Equation (3.45))⁹

$$K_{xx}(\omega) = \frac{2e^2}{\beta^2} \sum_{\mathbf{k}\mathbf{k}',\nu\nu'} \frac{\partial \epsilon_{\mathbf{k}}}{\partial k_x} G_{c,\nu\nu'\omega}^{(2),\mathbf{k}\mathbf{k}'q=0} \frac{\partial \epsilon_{\mathbf{k}'}}{\partial k'_x} \quad (4.60)$$

$$= -\frac{2e^2}{\beta} \sum_{\mathbf{k}\nu} \frac{\partial \epsilon_{\mathbf{k}}}{\partial k_x} G_{\mathbf{k}}(\nu) G_{\mathbf{k}}(\nu + \omega) J_{x,\mathbf{k}}^{\nu\omega}. \quad (4.61)$$

The lowest order without any vertex corrections hence yields $J_{x,\mathbf{k}}^{0,\nu\omega} = \frac{\partial \epsilon_{\mathbf{k}}}{\partial k_x}$, as we can see by a comparison with Equation (4.57).

Hitherto, we focused on the case without an external magnetic field. The reformulation in terms of a current vertex J enables us to discuss the case including a static magnetic field where $K_{xy} \neq 0$ in Equation (4.50).

In 1988 H. Kohno and K. Yamada derived an expression [97] for the off-diagonal terms of the conductivity tensor which are linear in the external magnetic field. In their calculation they applied several Ward identities to maintain gauge invariance and neglected the 3P vertex correction¹⁰ to obtain (Ref. [90] (3.47))

$$K_{xy}(\omega) = \frac{ie^3}{\beta} \sum_{\nu,\mathbf{k}} \sum_{\mu,\nu}^{xy} \left[\frac{\partial G_{\mathbf{k}}(\nu + \omega)}{\partial k_{\mu}} G_{\mathbf{k}}(\nu) - G_{\mathbf{k}}(\nu + \omega) \frac{\partial G_{\mathbf{k}}(\nu)}{\partial k_{\mu}} \right] \times \left[J_{x,\mathbf{k}}^{\nu\omega} \frac{\partial}{\partial k_{\nu}} J_{y,\mathbf{k}}^{\nu\omega} \right] \varepsilon_{\mu\nu z}, \quad (4.62)$$

$\varepsilon_{\mu\nu z}$ is completely antisymmetric with $\varepsilon_{xyz} = 1$.

The expression can be further approximated by additionally neglecting 2P vertex correction. This way, one recovers the bubble approximation of the off-diagonal element in the conductivity tensor. We took this approach in order to compute the Hall resistivity

⁹The sign we see by comparing the first and second line in Equations (4.60) and (4.61), as well as comparing to the Ref. [90] originates from the definition of the two-particle Green's function.

¹⁰To this point, we have not introduced the concept of 3P vertex corrections. It is analogy to the 2P level, they can be defined considering the fully connected part of the three-particle Green's function. [79]

4. Results

for the non-interacting system in Figure 4.22. The expression we implemented [62] reads

$$\sigma_{xy} \propto \int d\omega \left(\frac{\partial f}{\partial \omega} \right) \sum_{\mathbf{k}} A^3(\mathbf{k}, \omega) \left(\frac{\partial \epsilon_{\mathbf{k}}}{\partial k_x} \right)^2 \times \left[\left(\frac{\partial^2 \epsilon_{\mathbf{k}}}{\partial k_y^2} \right) \left(\frac{\partial \epsilon_{\mathbf{k}}}{\partial k_y} \right)^2 - \left(\frac{\partial^2 \epsilon_{\mathbf{k}}}{\partial k_x \partial k_y} \right) \right]. \quad (4.63)$$

In order to build some intuition for the complexity of this problem we implemented Equations (4.58), (4.59) and (4.63). These results are preliminary and need further benchmarking. We used a weakly correlated toy model based on the non-interacting density of states shown in Figure 2.5 combined with two choices for the scattering rate, i.e. $\gamma = 0.005$ eV and¹¹ $\gamma = (10^{-3} + 10^{-6}T^2)$ eV, as well as two¹² is not dopings $\delta = 0$ and 0.2.

In Figure 4.22¹³ (top row) we present the resistivity $\rho = 1/\sigma_{xx}$ for this toy model. Here, we in particular compare Equations (4.58) and (4.59) (A vs. B) and observe that while the magnitude may indeed strongly differ, the qualitative behaviour w.r.t. temperature is the same. Furthermore, when comparing the constant scattering rate at different doping (left and center), even on this per construction weakly correlated level the T -dependence of the scattering rate does not uniquely determine the T -dependence of the resistivity.

In Figure 4.22 (middle row), the Hall coefficient $R_H = \sigma_{xy}/(\sigma_{xx})^2$ computed by means of Equations (4.58) and (4.63) is shown. The behaviour for all choices of scattering rate and doping have different T -dependence. Let us highlight that even when ρ in the middle and the right column have similar T -dependence, it does not lead to a similar T -dependence for R_H .

Figure 4.22 (bottom row) shows $\rho/\rho_H = \sigma_{xx}/\sigma_{xy}$ again computed by means of Equations (4.58) and (4.63). Merely accidentally the choice of a constant scattering rate at $\delta = 0.2$ (center column) somewhat resembles the T -dependence observed in the experiment. However, it is important to point out that this approximation includes no \mathbf{k} -dependence nor frequency dependence nor strong correlations nor vertex corrections, and is therefore not applicable to our modelization of cuprates.

As we have mentioned at the beginning this calculation is just a preliminary property to the case of cuprates, which will be analyzed further in the future. The path in order to apply the expressions discussed in this chapter to the two dimensional Hubbard model is the following:

The current vertex in Equation (4.61) should be implemented within a DGA and DF formalism. It enables the computation of $K_{xx}(\omega)$ and $K_{xy}(\omega)$ in Equations (4.61)

¹¹The choice of coefficients is not based on any specific input.

¹²For doping $\delta = 0$ the Fermi surface is very close to the Van Hove singularity. In contrast, for $\delta = 0.2$ the Fermi surface is shift such that the Fermi surface is not in the direct proximity of the Van Hove singularity.

¹³Note that the order of magnitude changes considerably between the three considered cases in Figure 4.22, i.e. for the columns. The difference in magnitude is due to the proximity to the Van Hove singularity in the half-filled case. We deliberately show only the T -dependence and omit the order of magnitude, in order to highlight the temperature behaviour.

4. Results

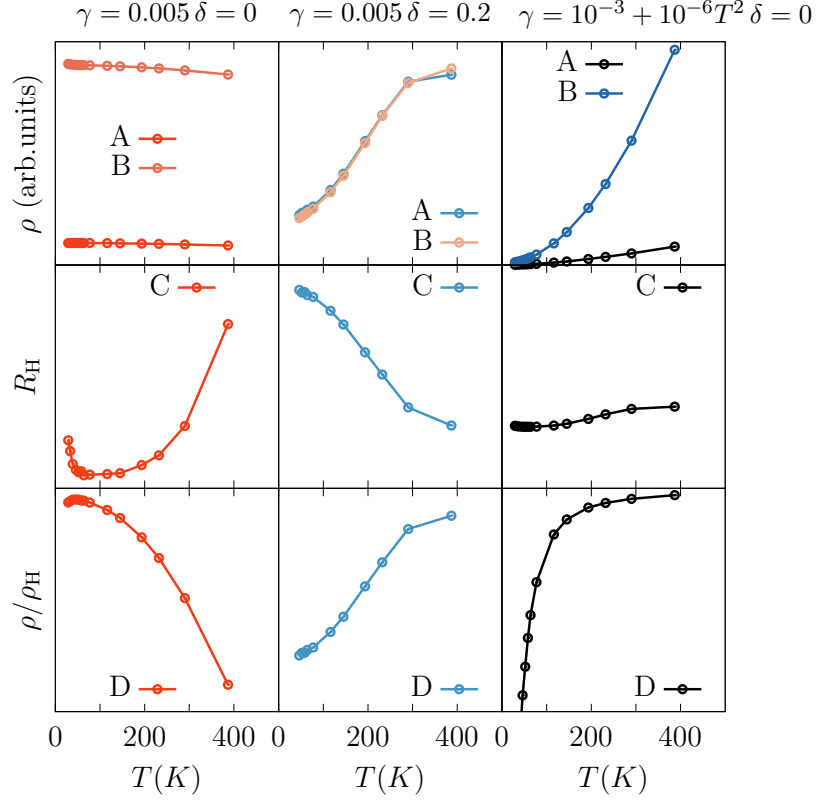


Figure 4.22.: The T -dependence of the DC resistivity $\rho = 1/\sigma_{xx}$ (top row), the Hall coefficient $R_H = \sigma_{xy}/(\sigma_{xx})^2$ (middle row) and the ratio $\rho/\rho_H = \sigma_{xx}/\sigma_{xy}$ (bottom row) for the weakly correlated system. For the density of states shown in Figure 2.5 we implemented Equation (4.58), Equation (4.59) and Equation (4.63) with $\gamma = -\text{Im}\Sigma(\omega = 0) = 0.005$ eV at half-filling (left column) and with doping $\delta = 0.2$ (center column), as well as with $\gamma = (10^{-3} + 10^{-6}T^2)$ eV at half-filling (right column). For A using Equation (4.58), B using Equation (4.59), C and D using Equations (4.58) and (4.63). Also see Footnote 13.

4. Results

and (4.62) respectively. Note, that these are given for a bosonic Matsubara frequency. An analytic continuation has to be performed in order to finally compute the conductivity tensor and take the zero frequency limit.

H. Kontani applied these expressions [98] including vertex corrections to the current operator to a single-band Hubbard model in 1998. He could reproduce both the temperature and doping dependence of R_H in cuprates, as well as the universal behaviour of ρ/ρ_H . His numerical calculations are based on the fluctuation-exchange approximation [99] (FLEX), which is a perturbative method and hence applicable in the weak-coupling regime. FLEX becomes insufficient near the Mott insulating phase and limited his analysis to $T > T^*$ and doping $|\delta| > 0.1$.

This discussion should be encouraging for two main reasons. Both, D Γ A and DF, can in principal compute the expressions in Equations (4.61) and (4.62). Most importantly both methods take into account non-local spin fluctuations like—but well beyond—FLEX.

In contrast to FLEX, D Γ A and DF are theoretically applicable to all temperature and doping regimes of the single-band Hubbard model. This might hold the keys for the description of challenging physics such as quantum critical behaviour and weak localization in and around the pseudogap regime, which has been mostly inaccessible thus far.

5. Conclusion and Outlook

This project was motivated by novel experimental findings [1] by N. Barišić *et al.* for transport mechanisms in cuprates. We recall, that while the DC resistivity characteristically changes its temperature (T) dependence throughout the rich phase diagram of cuprates, the experimental new results clearly showed a universal T^2 -dependence for the ratio of the DC resistivity over the Hall resistivity ρ/ρ_H . Strikingly, this T^2 -dependence emerges as a universal property of the whole cuprate phase diagram: It is observed, in fact, ubiquitous in the pseudogap phase, in the strange metal phase, and in the Fermi liquid phase across all hole-doping (δ) and temperature regimes, as well as in different compounds, c.f. Figure 1.4.

In this work we have started to analyze the possible connection between the experimentally observed quadratic T -dependence of ρ/ρ_H and the T -dependence of the electronic scattering rate at a level of the quantum many electron physics. The corresponding temperature trends can be easily related within the oversimplified description of a Drude model, but it was not expected that such description still holds for strongly correlated materials such as the cuprates. Our numerical results are based on calculations for the single-band Hubbard model on a square lattice with local Coulomb repulsion $U = 2.5$ eV, and hopping parameters $t = 0.25$ eV, $t = 0.5$ eV and $t'' = 0.025$ eV, which is solved by ladder dynamical vertex approximation (D Γ A) and dual fermion (DF) in order to include non-local particle-hole fluctuations beyond the weak coupling regime.

We summarize here the most important results we have obtained. In ladder D Γ A we observed the following:

- The system shows strong commensurate antiferromagnetic fluctuations for $\delta = 0.1$. For higher hole-doping, $\delta = 0.15, 0.2$, these fluctuations become weaker and incommensurate.
- The temperature dependence of the corresponding correlation length in the temperature interval considered is close but not equal to T^{-1} for $\delta = 0.1, 0.15$. For $\delta = 0.2$ it seems to perfectly agree with T^{-1} . At lower temperature an exponential growth in temperature for $T \rightarrow 0$ might appear.
- The imaginary part of the self-energy on the Matsubara axis clearly shows a strong momentum dependence indicating a qualitative deviation from the local description of DMFT. It develops a dip in the low Matsubara frequency range associated with pseudogap behaviour.
- The analytic continuation by both, Padé approximation and sparse modeling, show the lower Hubbard band around -0.6 eV and the upper Hubbard band at around

5. Conclusion and Outlook

1.9 eV. Unfortunately, the automatic evaluation of the Padé approximation by taking into account all physical constraints fails. This might be due to several causes: (i) the additional approximation introduced by the Moriya-esque λ -correction in DGA, (ii) the discretization of the DMFT(ED) bath, etc.. On the other hand, sparse modeling, applied to our DGA datasets, has difficulties to find an optimal regularization parameter.

- At the same time, the approximation $[\beta|G(\tau = \beta/2, \mathbf{k}_F)|]^{-1} \approx -\text{Im}\Sigma(\omega = 0, \mathbf{k}_F)$ seems to be invalid, in the parameter range of our interest, on the basis of a comparison against a simple visual inspection of $\text{Im}\Sigma(i\nu, \mathbf{k}_F)$ for $i\nu \rightarrow 0$.
- The precise T -dependence of the scattering rate could not be extracted from our current ladder DGA results.
- Nonetheless, the whole set of data, and especially the analytically not continued data of $\text{Im}\Sigma(i\nu, \mathbf{k}_F)$, appears hardly compatible with an universal behaviour of the scattering rate over the whole phase diagram.

As for the DF results, the outcome is at the present status of our calculations even less clear: Our current DF results are, most likely, affected by an incorrect filling due to an insufficient adjustment of the chemical potential within the self-consistency cycles. For the moment, we can merely report qualitative similarity between a one-shot DF and DGA calculation for $\beta|G(\tau = \beta/2, \mathbf{k}_F)|$. Updating the Anderson impurity model, however, leads to significant changes of the DF solution. It is unclear whether these changes are due to technical issues, such as the change of the impurity solver¹ or still to poor statistics, or whether it is because DF would indeed obtain a radically different result via the external self-consistency.

In order to improve the analysis of the existing numerical results for ladder DGA, we need to find a suitable method for performing a stable analytic continuation. One modern approach was taken in Ref. [100], where a machine learning algorithm was employed.

In the case of our DF calculations a possible solution for the adjustment of the chemical potential has already been implemented in another branch of the code. This improvement will hopefully enable a more successful repetition of the same calculation.

Under consideration of the strengths and weaknesses of ladder DGA and DF as emerged in our study, it may be rewarding to focus on the two-particle level. Here two suggestions may be followed in future studies, which both involve an analytic continuation of a bosonic quantity:

In the final part of this work we have considered the ratio ρ/ρ_H in terms of the conductivity tensor. The expressions, that we have extracted from literature, could be implemented in future DGA and DF studies. The key ingredients for these expressions

¹We first obtained all local quantities by means of an exact diagonalization scheme for a converged dynamical mean-field theory calculation. Subsequently, the one-shot DGA and DF calculations, were done using the same input. However further outer loop iterations in DF employed a continuous time QMC algorithm.

5. Conclusion and Outlook

is the generalized current vertex of Equation (4.61), which could be also expressed by means of the generalized susceptibility in the charge channel.

Further studies may also analyze whether our D Γ A/DF calculations support the spin-freezing perspective [101] that has been recently put forward by P. Werner *et al.* also for explaining the pseudogap phenomenology. This involves a closer analysis of the spin susceptibility.

At this point we may note from the quantum many-body theory viewpoint, we were not yet able to “simplify” the rich phase diagram of cuprates as suggested by the most recent experiment. But if I may add a loose translation of my initial quotation: “Everything worth-while may take a while.”

Appendices

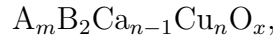
A. Crystal structure

Generally one may distinguish between:

- $\text{Ba}_{1-x}\text{K}_x\text{BiO}_3$,
- $\text{La}_{2-x}\text{M}_x\text{CuO}_{4-y}$,
- $\text{Nd}_{2-x}\text{Ce}_x\text{CuO}_4$ -Based Compounds,
- YBaCuO-Based Compounds, and
- Bi-, Tl- and Hg-Compounds.

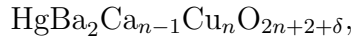
For a detailed Review see the book [15] by N. Plakida published in 2010. Here, we briefly summarize its chapter about Bi-, Tl- and Hg-Compounds. In this summary there is a special emphasize on Hg-Compounds as these are used in the resistivity measurements [1] by N. Barišić *et al.*, which are the main focus of this work.

The Bi-, Tl- and Hg-compounds can be expressed in the general formula



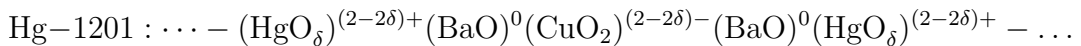
where A= Bi, Ti or Hg and B = Sr (for Bi), Ba (for Tl and Hg). Further, for Bi $m = 2$, Ti $m = 1$ or 2, while Hg $m = 1$.

The choice A=Hg, B=Ba and $m = 1$ yields



where n determines the number of CuO_2 -planes. A convention for denoting this series of compounds is $\text{Hg}-12(n-1)n$.¹ The series was discovered in 1993: Hg-1201 [102], Hg-1212 [103] and Hg-1223 [104]. And continued expanding with Hg-1234, Hg-1245 [105], up to so-called infinite layered compounds with $n \geq 6$ [106].

The crystal structure of Hg-based compounds with $n = 1, 2$ and 3 are displayed in Figure A.1. The tetragonal structures of Hg-1201, Hg-1212 and Hg-1223 accommodate correspondingly $n = 1, 2$ and 3 CuO_2 -planes parallel to the xy -plane and $n - 1$ Ca atoms are placed above the centres of the CuO_2 squares. This is sandwiched by a pair of BaO planes. Hg-ions then separate these basic layered sheets. In other words the layers are stacked in the following sequence:



¹ Analogously, the convention for $\text{TlBa}_2\text{Ca}_{n-1}\text{Cu}_n\text{O}_{2n+3+\delta}$ is Tl-12 $(n-1)n$ etc....

A. Crystal structure

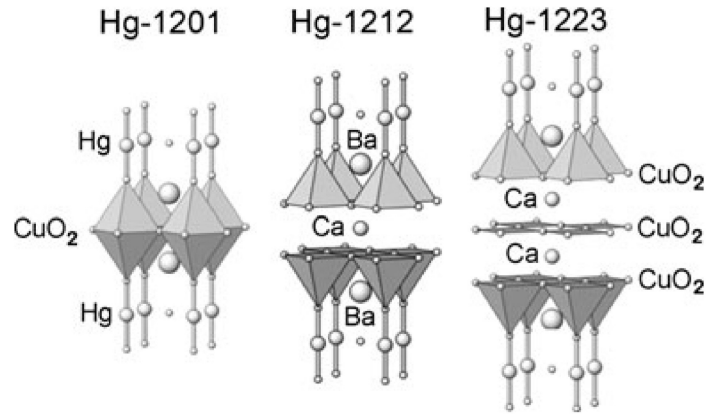


Figure A.1.: Crystal structure of mercury compounds Hg-1201, Hg-1212 and Hg-1223.[15] Fig. 2.17 [107] Fig. 10

The tetragonal structure belongs to the space group $P4/mmm$. In $\text{HgBa}_2\text{Ca}_{n-1}\text{Cu}_n\text{O}_{2n+2+\delta}$, δ denotes the doping. In case of hole doping, the compound is annealed in an oxygen atmosphere. This leads to the implementation of excess oxygen ions in the buffer layer $\text{Hg} - \text{O}_\delta$ with concentration δ . The doping is depicted in Figure A.1.

B. Derivations

B.1. The fermionic coherent state path integral

The coherent state is the eigenstate of the annihilation operator a . To define such a state in the fermionic case, we need to introduce Grassman variables, which are anticommuting numbers:

$$\{c_i, c_j\} = 0 \quad (\text{B.1})$$

Assume we have a function $f(c_i) = a + c_i b$, which is commuting. Thus b is anticommuting. To complete the definition we additionally need to define how to differentiate and integrate. To differentiate with respect to c_i from the left we must write c_i to the far left:

$$\partial_{c_i} f(c_i) = b. \quad (\text{B.2})$$

Integration must obey linearity

$$\int_{-\infty}^{\infty} dc_i \alpha f(c_i) = \alpha \int_{-\infty}^{\infty} dc_i f(c_i) \quad (\text{B.3})$$

and invariance under a shift of the c_i by a constant

$$\int_{-\infty}^{\infty} dc_i f(c_i + \beta) = \int_{-\infty}^{\infty} dc_i f(c_i). \quad (\text{B.4})$$

The only nontrivial definition up to a numerical factor is given by the Berezin integration:

$$\int_{-\infty}^{\infty} dc_i f(c_i) = b. \quad (\text{B.5})$$

With the definition of Grassman variables we can make an educated guess for the fermionic coherent state:

$$|c\rangle = e^{-\sum_i c_i a_i^\dagger} |\rangle = \prod_i (1 - c_i a_i^\dagger) |\rangle, \quad (\text{B.6})$$

B. Derivations

where $|\rangle$ is the vacuum ground state and a_i^\dagger creates an electron at \mathbf{x}_i with spin σ_i . We proof now that this is indeed the eigenstate of a with eigenvalue c_i :

$$\begin{aligned}
a_j|c\rangle &= a_j \prod_i \left(1 - c_i a_i^\dagger\right) |\rangle \\
&= \prod_{i=0}^{j-1} \left(1 - c_i a_i^\dagger\right) a_j \left(1 - c_j a_j^\dagger\right) \prod_{i=j+1} \left(1 - c_i a_i^\dagger\right) |\rangle \\
&= \prod_{i=0}^{j-1} (\dots) \left(a_j + c_j a_j a_j^\dagger\right) \prod_{i=0}^{j-1} (\dots) |\rangle \\
&\text{with } \left(a_j + c_j a_j a_j^\dagger\right) |\rangle = (0 + c_j 1) |\rangle
\end{aligned} \tag{B.7}$$

$$\begin{aligned}
c_j|c\rangle &= c_j \prod_i \left(1 - c_i a_i^\dagger\right) |\rangle \\
&= \prod_{i=0}^{j-1} \left(1 - c_i a_i^\dagger\right) c_j \left(1 - c_j a_j^\dagger\right) \prod_{i=j+1} \left(1 - c_i a_i^\dagger\right) |\rangle \\
&= \prod_{i=0}^{j-1} (\dots) \left(c_j + c_j^2 a_j^\dagger\right) \prod_{i=0} \\
&\text{with } \left(c_j + c_j^2 a_j^\dagger\right) |\rangle = \left(c_j + 0 a_j^\dagger\right) |\rangle
\end{aligned} \tag{B.8}$$

Let us state the unity to be

$$1 = \int \prod_i d\bar{c}_i dc_i e^{\sum_i \bar{c}_i c_i} |c\rangle \langle c|. \tag{B.9}$$

For the sake of more clarity and less distraction we define the following convention

$$\bar{c}c \equiv \sum_i \bar{c}_i c_i \tag{B.10}$$

$$d\bar{c}dc = \prod_i d\bar{c}_i dc_i \tag{B.11}$$

and rewrite Eq. B.9 as

$$1 = \int d\bar{c}dc e^{\bar{c}c} |c\rangle \langle c|. \tag{B.12}$$

B. Derivations

With the unity we can rewrite the trace of an operator A in terms of Grassman variables

$$\begin{aligned}
\text{tr}\{A\} &= \sum_i \langle i|A|i\rangle \\
&= \sum_i \langle i|A \int d\bar{c}dc e^{\bar{c}c}|c\rangle\langle c|i\rangle \\
&= \int d\bar{c}dc e^{-\bar{c}c} \sum_i \langle i|A|c\rangle\langle c|i\rangle \\
&= \int d\bar{c}dc e^{-\bar{c}c} \sum_i \langle -c|i\rangle\langle i|A|c\rangle \\
&= \int d\bar{c}dc e^{-\bar{c}c} \langle -c|A|c\rangle.
\end{aligned} \tag{B.13}$$

Let us introduce the time evolving state as

$$|c(t)\rangle = e^{iHt}|c\rangle \tag{B.14}$$

and the time evolution operator

$$U(f, i) \equiv \langle c^{(f)}(t_f)|c^{(i)}(t_i)\rangle \tag{B.15}$$

One can now describe the transition amplitude from one state $c^{(i)}$ to another $c^{(f)}$ at zero temperature by a path integral. We begin by dividing the time interval into $N + 1$ equal pieces $\Delta t = \frac{t_f - t_i}{N+1}$. Then introduce N complete sets of eigenstates

$$\begin{aligned}
\langle c^{(f)}|e^{-iH(t_f - t_i)}|c^{(i)}\rangle &= \int \prod_{n=1}^N d\bar{c}c \langle c^{(f)}|e^{-iH\Delta t} e^{\sum_i \bar{c}_i^{(N)} c_i^{(N)}}|c^{(N)}\rangle \\
&\quad \langle c^{(N)}|e^{-iH\Delta t} e^{\sum_i \bar{c}_i^{(N-1)} c_i^{(N-1)}}|c^{(N-1)}\rangle \dots \langle c^{(1)}|e^{-iH\Delta t}|c^{(i)}\rangle.
\end{aligned} \tag{B.16}$$

As we send $N \rightarrow \infty$ later, we can approximate $e^{-iH\Delta t} \approx (1 - iH\Delta t)$. Then rewrite $e^{\sum_i \bar{c}_i^{(n)} c_i^{(n)}}|c^{(n)}\rangle = \prod_i (1 + \bar{c}_i^{(n)} c_i^{(n)})|c^{(n)}\rangle$, which leads for each time step to an evaluation of the Hamiltonian, yielding

$$\begin{aligned}
\langle c^{(n)}|e^{-iH\Delta t} e^{\sum_i \bar{c}_i^{(n-1)} c_i^{(n-1)}}|c^{(n-1)}\rangle &= \langle c^{(n)}|(1 - iH[a^\dagger, a]\Delta t) \prod_i (1 + \bar{c}_i^{(n-1)} c_i^{(n-1)})|c^{(n-1)}\rangle \\
&= (1 - iH[\bar{c}, c]\Delta t) \prod_i (1 + \bar{c}_i^{(n-1)} c_i^{(n-1)}) \langle c^{(n)}|c^{(n-1)}\rangle.
\end{aligned} \tag{B.17}$$

Now inserting the definition of the coherent state from Eq. B.6 and then using $\bar{c}^{(n)} =$

B. Derivations

$(\frac{1}{\Delta t} \bar{c}^{(n-1)}) \Delta t + \bar{c}^{(n-1)}$ yields

$$\begin{aligned}
\langle c^{(n)} | c^{(n-1)} \rangle &= \langle | e^{\sum_k \bar{c}_k^{(n)} a_k^{(n)}} e^{-\sum_l c_l^{(n-1)} a_l^{\dagger(n-1)}} | \rangle \\
&= \langle | e^{\sum_k \bar{c}_k^{(n-1)} \frac{1}{\Delta t} a_k^{(n)} \Delta t + \sum_k \bar{c}_k^{(n-1)} a_k^{(n)}} e^{-\sum_l c_l^{(n-1)} a_l^{\dagger(n-1)}} | \rangle \\
&= \langle c^{(n-1)} | e^{\sum_i \bar{c}_i^{(n-1)} \frac{1}{\Delta t} a_i^{(n)} \Delta t} | c^{(n-1)} \rangle \\
&= \langle c^{(n-1)} | e^{\sum_i a_i^{\dagger(n-1)} \partial_t a_i^{(n)} \Delta t} | c^{(n-1)} \rangle
\end{aligned} \tag{B.18}$$

Gathering all the terms from Eq.s B.16 - B.18 for Eq. B.15 gives the evolution operator as

$$\langle c^{(f)} | e^{-iH(t_f - t_i)} | c^{(i)} \rangle = \lim_{N \rightarrow \infty} \int \prod_{n=0}^N d\bar{c} dc \langle c^{(f)} | e^{\sum_{n=1}^N \sum_i (a_i^{\dagger(n)} \partial_t a_i^{(n)} - iH[a_i^{\dagger(n)}, a_i^{(n)}]) \Delta t} | c^{(i)} \rangle, \tag{B.19}$$

which is by taking the limit and adapting a more convenient notation, given by

$$U(f, i) = \int_{\bar{c}c} \langle c^{(f)} | e^{\int_{t_i}^{t_f} dt (a^\dagger \partial_t a - iH[a^\dagger a])} | c^{(i)} \rangle. \tag{B.20}$$

Here the path integral is denoted by $\int_{\bar{c}c} = \int \prod_{n=0}^{\infty} d\bar{c} dc$ and the summation over time intervals is replaced by an integral $\sum_{n=1}^N \Delta t \rightarrow \int_{t_i}^{t_f} dt$

Finally we have all the ingredients to derive the expression we are truly interested in, the partition function. The most straightforward way to arrive at the partition function is simply to sum up all energy eigenstates of the system with the appropriate Boltzmann factor $e^{-\beta H}$, where β is the inverse temperature and H is the Hamiltonian¹. We thus choose $A = e^{-\beta H}$ in Eq. B.13

$$Z = \int d\bar{c} dc e^{-\bar{c}c} \langle -c | e^{-\beta H} | c \rangle. \tag{B.21}$$

The expression for Z is very similar to Eq. B.16, with $i(t - t') = \beta$. To proceed in analogy to the time evolution operator we divide the imaginary time interval β into $M + 1$ equal pieces of 'duration' $\Delta\tau = \frac{\beta}{M+1}$.

$$\begin{aligned}
Z &= \int d\bar{c} dc \int \prod_m d\bar{c}^{(m)} dc^{(m)} \langle -c | e^{-H\Delta\tau} e^{\bar{c}^{(M)} c^{(M)}} | c^{(M)} \rangle \\
&\quad \langle c^{(M)} | e^{-H\Delta\tau} e^{\bar{c}^{(M-1)} c^{(M-1)}} | c^{(M-1)} \rangle \dots \langle c^{(1)} | e^{-H\Delta\tau} e^{\bar{c}c} | c \rangle,
\end{aligned} \tag{B.22}$$

where we rewrite the terms

$$\langle c^{(m)} | e^{-H\Delta\tau} e^{\bar{c}^{(m-1)} c^{(m-1)}} | c^{(m-1)} \rangle = \langle c^{(m-1)} | e^{-(\bar{c}^{(m-1)} \partial_\tau c^{(m)} + H)\Delta\tau} e^{\bar{c}^{(m-1)} c^{(m-1)}} | c^{(m-1)} \rangle \tag{B.23}$$

and impose boundary conditions $-c = c^M$ and $c = c^0$ and hence $c^0 = -c^M$. In the limit $M \rightarrow \infty$ the partition function finally takes the form

$$Z = \int_{\bar{c}c} e^{-\int_0^\beta d\tau (\bar{c} \partial_\tau c + H)}, \tag{B.24}$$

¹To work with the grand canonical ensemble replace $H \rightarrow H - \mu N$

B. Derivations

with boundary condition $c(\tau = 0) = -c(\tau = \beta)$. It is analogous to Eq. B.20, however due to the extra exponential in the expression for the trace and the boundary condition all states nicely disappear and we are left with an expression for the fields.

A familiar approach in quantum field theory on the other hand is to express the partition function in terms of the action

$$Z = \int_{\bar{c}c} e^{iS} = \langle 0|0 \rangle_{\text{src}}, \quad (\text{B.25})$$

where the suffix src indicates the presence of sources. The crucial assumption is that the system is in the ground state at $t \rightarrow \infty$ and $t' \rightarrow -\infty$. It can be reasoned as follows: Assume an arbitrarily small shift $H \rightarrow (1 - i\delta)H$ in a time evolving state

$$\begin{aligned} |c(t)\rangle &= e^{iHt}|c\rangle \\ &= \sum_{n=0}^{\infty} e^{iE_n t} \langle n|c\rangle |n\rangle, \end{aligned} \quad (\text{B.26})$$

and take the limit $t \rightarrow -\infty$. Except for the ground state, which we choose to be $E_0 = 0$, all states are multiplied by a vanishing exponential factor. The limit is thus $\langle 0|c\rangle|0\rangle$, and similar for $\lim_{t' \rightarrow \infty} \langle c(t')| = \langle 0|\langle c|0\rangle$. The constant values $\langle 0|c\rangle$ and $\langle c|0\rangle$ are simply swallowed by the normalization later on, therefore they do not concern us and we simply assume the ground state at $t \rightarrow \infty$ and $t' \rightarrow -\infty$. So in other words Eq. B.25 evaluates all possible paths from $t \rightarrow \infty$ to $t' \rightarrow -\infty$.

How do we connect Eq. B.24 and Eq. B.25 with each other? The trick is here to perform a Wick rotation to imaginary time $it \rightarrow \tau$. It puts the Boltzman factor on the same level as the time evolution. As the action contains integration over time, Eq. B.25 appears after a Wick Rotation as

$$Z = \int_{\bar{c}c} e^{-S} = \langle 0|0 \rangle_{\text{src}}, \quad (\text{B.27})$$

where in the great canonical ensemble the action is given by

$$S = \int_0^\beta d\tau (\bar{c}\partial_\tau c + H) \quad (\text{B.28})$$

B.2. Filling and chemical potential

The one-particle Green's function in imaginary time τ , as it appears in Equation (2.31), is defined as

$$G(\mathbf{k}, \tau) = -\frac{1}{Z} \text{tr}\{e^{-\beta H} \mathcal{T}_\tau \hat{c}_\mathbf{k}(\tau) \hat{c}_\mathbf{k}^\dagger(0)\}, \quad (\text{B.29})$$

where \mathcal{T}_τ is the imaginary time ordering operator and $\hat{c}(\hat{c}^\dagger)$ are fermionic second quantization operators that were denoted by $a(a^\dagger)$ in the derivation of the fermionic coherent state path integral in Section B.1.

B. Derivations

Let us compute the filling defined as the thermal average of the density operator $\hat{n} = \hat{c}_{\mathbf{k}}^\dagger \hat{c}_{\mathbf{k}}$,

$$\langle \hat{n} \rangle = \bigcirc = \frac{1}{N_{\mathbf{k}}} \sum_{\mathbf{k}} \langle \hat{c}_{\mathbf{k}}^\dagger \hat{c}_{\mathbf{k}} \rangle. \quad (\text{B.30})$$

Using $\langle \hat{c}^\dagger \hat{c} \rangle = G(\mathbf{k}, \tau = 0^-)$ and the Fourier transformation defined in Equation (C.12), yields

$$\langle \hat{n} \rangle = \frac{1}{N_{\mathbf{k}}} \sum_{\mathbf{k}} G(\mathbf{k}, \tau = 0^-) \quad (\text{B.31})$$

$$= \frac{1}{N_{\mathbf{k}}} \sum_{\mathbf{k}} \frac{1}{\beta} \sum_n e^{-i\nu_n 0^-} G(\mathbf{k}, i\nu_n). \quad (\text{B.32})$$

By introducing the Fermi function as a weight function, this expression can be rewritten by means of the residual theorem,

$$\oint_{\Gamma} dz f(z) = 2\pi i \sum_{a \in \Gamma} \text{Res}_a f(z), \quad (\text{B.33})$$

in terms of a sum over the poles of the Green's function:

$$\frac{1}{\beta} \sum_n e^{-i\nu_n 0^-} G(\mathbf{k}, i\nu_n) = \sum_{z_0 \in \text{poles of } G} \text{Res}_{z_0} \{f(z)G(\mathbf{k}, z)\}, \quad (\text{B.34})$$

where $f(z) = 1/(e^{\beta z} + 1)$ is the Fermi function. If we enter the non-interacting Greens function Equation (2.25), here $G^0(\mathbf{k}, z) = \frac{1}{z - (\epsilon(\mathbf{k}) - \mu)}$, we find

$$\langle n \rangle = \frac{1}{N_{\mathbf{k}}} \sum_{\mathbf{k}} \sum_{z_0 \in \text{poles of } G} \text{Res}_{z_0} \left\{ \frac{f(z)}{z - (\epsilon(\mathbf{k}) - \mu)} \right\} \quad (\text{B.35})$$

$$= \frac{1}{N_{\mathbf{k}}} \sum_{\mathbf{k}} f(\epsilon(\mathbf{k}) - \mu) \quad (\text{B.36})$$

$$= \frac{(\text{number of occupied states})}{(\text{total number of states})}, \quad (\text{B.37})$$

where in the last line we used the simplified picture true only at $T = 0$, that $f(\epsilon(\mathbf{k}) - \mu) = 1$, if a state with quantum number \mathbf{k} is occupied, and respectively $f(\epsilon(\mathbf{k}) - \mu) = 0$, if empty.

Numerically, we can sum over all available Matsubara frequencies. But note that,

$$\frac{1}{\beta} \sum_n \frac{e^{i\nu_n 0^-}}{i\nu_n} = f(z = 0) = \frac{1}{2}, \quad (\text{B.38})$$

is not absolutely convergent without the convergent factor $e^{i\nu_n 0^-}$.² The trick is to add and subtract as follows

$$\frac{1}{\beta} \sum_n \frac{e^{i\nu_n 0^-}}{i\nu_n} = \frac{1}{\beta} \sum_n \left[\frac{e^{i\nu_n 0^-}}{i\nu_n} - \frac{1}{i\nu_n} \right] + \frac{1}{2}, \quad (\text{B.39})$$

² Just like the logarithm does not have asymptotic behaviour for large arguments.

B. Derivations

where the sum over $\frac{e^{i\nu_n 0^-}}{i\nu_n} - \frac{1}{i\nu_n} \propto \left(\frac{1}{i\nu_n}\right)^2$ is convergent.

If you did not believe that $G(k, i\nu_n) \propto \frac{c_1}{i\nu_n}$, $c_1 \equiv 1$, let me convince you. The high-frequency expansion of the Green's function is of the general form

$$G(i\nu_n) = \frac{c_1}{i\nu_n} + \frac{c_2}{(i\nu_n)^2} + \frac{c_3}{(i\nu_n)^3} + \dots \quad (\text{B.40})$$

Using Equation (C.11) and partial integration, we can determine the coefficients as follows:

$$G(i\nu_n) = \int_0^\beta d\tau e^{i\nu_n \tau} G(\tau) \quad (\text{B.41})$$

$$= \frac{-G(\beta) - G(0)}{i\nu_n} - \frac{-G'(\beta) - G'(0)}{(i\nu_n)^2} + \frac{-G''(\beta) - G''(0)}{(i\nu_n)^3} + \dots \quad (\text{B.42})$$

Considering Equation (B.31) and the antiperiodicity, namely $G(\tau) = -G(\tau + \beta)$, yields $G(\beta) = -n$. Using the anti-commutation relation, it is clear that $G(0^+) = -(1 - n)$. Hence, the value of $c_1 = -G(\beta) - G(0) = +n + (1 - n) \equiv 1$.

B.3. The hybridization function of AIM

The full Hamiltonian of the Anderson Impurity Model (AIM) in terms of Grassmann variables is given by

$$H = \sum_{l,\sigma} \varepsilon_l \bar{b}_{l\sigma} b_{l\sigma} + \sum_{l,\sigma} [V_l \bar{b}_{l\sigma} c_\sigma + V_l^* \bar{c}_\sigma b_{l\sigma}] + U n_\downarrow n_\uparrow - \mu \sum_\sigma \bar{c}_\sigma c_\sigma, \quad (\text{B.43})$$

where the first term is the bath Hamiltonian. Here $\bar{b}_{l\sigma}, b_{l\sigma}$ are the fields of a fermionic non-interacting bath with spin σ and orbital l degree of freedom and energy levels ε_l . The second term describes the hybridization between the bath and an impurity site. The Grassmann fields \bar{c}_σ, c_σ describe creation and annihilation on the impurity. Hence V_l describes the hopping of an impurity Fermion to the bath and V_l^* vice versa, respectively. The remaining two terms describe the impurity at a chemical potential μ with on-site Coulomb repulsion, also called Hubbard- U , U .

The partition function is given by the Fourier transformation of B.25

$$Z = \int d\bar{c}dc d\bar{b}db \exp \left(- \sum_{\nu,l,\sigma} \bar{b}(-i\nu + \varepsilon_l)b + [V_l \bar{b}_{l\sigma} c_\sigma + V_l^* \bar{c}_\sigma b_{l\sigma}] + \bar{c}_\sigma (-i\nu - \mu) c_\sigma + U [\bar{c}, c] \right), \quad (\text{B.44})$$

where $d\bar{c}dc = \prod_{\nu\sigma} \bar{c}_{\nu\sigma} dc_{\nu\sigma}$ and respectively $d\bar{b}db = \prod_{\nu,l,\sigma} \bar{b}_{\nu l\sigma} db_{\nu l\sigma}$, following the convention of B.10, while $\bar{c}c = \sum_{\nu,l,\sigma} \bar{c}_{\nu\sigma} c_{\nu\sigma}$ and $\bar{c}c = \sum_{\nu,l,\sigma} \bar{c}_{\nu l\sigma} b_{\nu l\sigma}$. We now integrate over the bath degrees of freedom. Let us consider the integration over one particular index

B. Derivations

$i = \nu, l, \sigma$ in the sum in the exponent:

$$\int d\bar{b}_i db_i \exp(-\bar{b}_i (i\nu - \varepsilon_l) b_i - [V_l \bar{b}_i c_{\nu\sigma} + \text{c.c.}]) \quad (\text{B.45})$$

$$= \int d\bar{b}_i db_i (1 - \bar{b}_i (i\nu - \varepsilon_l) b_i) \left(1 - [V_l \bar{b}_i c_{\nu\sigma} + \text{c.c.}] + \frac{1}{2} |V_l|^2 [V_l \bar{b}_i c_{\nu\sigma} + \text{c.c.}] [V_l \bar{b}_i c_{\nu\sigma} + \text{c.c.}] \right)$$

NB: All terms vanish except $1 \times \frac{1}{2} |V_l|^2 [\dots]$, and $\bar{b}_i (i\nu - \varepsilon_l) b_i \times 1$.

$$\begin{aligned} &= (i\nu - \varepsilon_l) + |V_l|^2 \bar{c}_{\nu\sigma} c_{\nu\sigma} \\ &= (i\nu - \varepsilon_l) \exp\left(\bar{c}_{\nu\sigma} \frac{|V_l|^2}{i\nu - \varepsilon_l} c_{\nu\sigma}\right). \end{aligned} \quad (\text{B.46})$$

Now defining the *hybridization function*,

$$\Delta_\nu = \sum_l \frac{|V_l|^2}{i\nu - \varepsilon_l}, \quad (\text{B.47})$$

and using B.46, we can evaluate B.44, yielding

$$Z = \mathcal{N} \int d\bar{c} dc \exp(\bar{c} (i\nu + \mu - \Delta_\nu) c - U n_\downarrow n_\uparrow), \quad (\text{B.48})$$

where \mathcal{N} is the normalization factor, which swallowed the prefactor of B.46.

B.4. Lehmann representation of one-particle Green's function

$$G_{\mathbf{k}\nu} = - \int_0^\beta d\tau e^{i\nu\tau} \langle \mathcal{T}_\tau [\hat{c}_{\mathbf{k}\sigma}(\tau) \hat{c}_{\mathbf{k}\sigma}^\dagger(0)] \rangle, \quad (\text{B.49})$$

$$= - \frac{1}{Z} \int_0^\beta d\tau e^{i\nu\tau} \text{Tr} \left(e^{-\beta H} \hat{c}_{\mathbf{k}\sigma}(\tau) \hat{c}_{\mathbf{k}\sigma}^\dagger(0) \theta(\tau) - e^{-\beta H} \hat{c}_{\mathbf{k}\sigma}^\dagger(0) \hat{c}_{\mathbf{k}\sigma}(\tau) \theta(-\tau) \right)$$

$$= - \frac{1}{Z} \int_0^\beta d\tau e^{i\nu\tau} \sum_{i,m} e^{-\beta E_i} \langle i | e^{\tau H} \hat{c}_{\mathbf{k}\sigma} e^{-\tau H} | m \rangle \langle m | \hat{c}_{\mathbf{k}\sigma}^\dagger | i \rangle$$

$$= - \frac{1}{Z} \sum_{i,m} e^{-\beta E_i} \left| \langle m | \hat{c}_{\mathbf{k}\sigma}^\dagger | i \rangle \right|^2 \int_0^\beta d\tau e^{\tau(i\nu + E_i - E_m)}$$

$$= \frac{1}{Z} \sum_{i,m} e^{-\beta E_i} \left| \langle m | \hat{c}_{\mathbf{k}\sigma}^\dagger | i \rangle \right|^2 \frac{1 - e^{\beta(i\nu + E_i - E_m)}}{E_i - E_m - i\nu}$$

$$= \frac{1}{Z} \sum_{i,m} \frac{\left| \langle m | \hat{c}_{\mathbf{k}\sigma}^\dagger | i \rangle \right|^2}{E_i - E_m - i\nu} (e^{-\beta E_i} + e^{-\beta E_m}) \quad (\text{B.50})$$

B.5. Hubbard Stratonovic transformation

Let us first note a simple property of any Gaussian integral over a real variable ($r \in \mathbb{R}$)

$$\int dr e^{-(ar+bs)^2} = \int dr e^{-a^2r^2-2abrs-b^2s^2} = \sqrt{\frac{\pi}{a}} = \mathcal{N}, \quad (\text{B.51})$$

$$\mathcal{N}e^{b^2s^2} = \int dr e^{-a^2r^2-2abrs}, \quad (\text{B.52})$$

$$\int ds e^{b^2s^2} = \mathcal{N}^{-1} \int dr \int ds e^{-a^2r^2-2abrs}, \quad (\text{B.53})$$

where integrals range from $-\infty$ to $+\infty$.

In a very similar manner, we can shift an integral over one fermionic field to another by means of the Hubbard-Stratonovic transformation. Assume the partition function is given as

$$Z = \int_{\bar{c}c} e^{-\mathcal{S}}, \quad (\text{B.54})$$

$$\mathcal{S} = B^2\bar{c}c. \quad (\text{B.55})$$

Then this is equal to

$$\mathcal{S} = B^{-2} \int_{\bar{f}f} \int_{\bar{c}c} e^{-AB(\bar{c}f+\bar{f}c)-B^2\bar{f}f}. \quad (\text{B.56})$$

B.6. Padé fit for $n = 4$

In order to fully understand the fitting procedure of Padé approximation, let's consider an example of $n = 4$, cf. Equation (3.63).

$$i = 1 : f^n(z_1) = a_1 = g(z_1) \quad (\text{B.57a})$$

$$i = 2 : f^n(z_2) = \frac{a_1}{1 + a_2(z_2 - z_1)} = g(z_2) = c_1 \quad (\text{B.57b})$$

$$\rightarrow a_2 = \left(\frac{a_1}{c_1} - 1 \right) \frac{1}{z_2 - z_1}$$

$$i = 3 : f^n(z_3) = g(z_3) = c_1 \quad (\text{B.57c})$$

$$c_2 = \left(\frac{a_1}{c_1} - 1 \right) \frac{1}{z_3 - z_1}$$

$$\rightarrow a_3 = \left(\frac{a_2}{c_2} - 1 \right) \frac{1}{z_3 - z_2}$$

$$i = 4 : f^n(z_4) = g(z_4) = c_1 \quad (\text{B.57d})$$

$$c_2 = \left(\frac{a_1}{c_1} - 1 \right) \frac{1}{z_4 - z_1}$$

$$c_3 = \left(\frac{a_2}{c_2} - 1 \right) \frac{1}{z_4 - z_2}$$

$$\rightarrow a_4 = \left(\frac{a_3}{c_3} - 1 \right) \frac{1}{z_4 - z_3}$$

Rewriting in terms of a rational function. As a next step, we will apply Equation (3.65). In order to properly add polynomials we expand them in their coefficients,

$$p^{(j)}(z) = \sum_{l=0}^L c_l^{(j)} z^l, \quad L = \text{Int}((j-1)/2), \quad (\text{B.58a})$$

$$q^{(j)}(z) = \sum_{m=0}^M d_m^{(j)} z^m, \quad M = \text{Int}(j/2), \quad (\text{B.58b})$$

yielding a recursion for the coefficients $c_l^{(j)}$ and $d_m^{(j)}$:

$$c_{l=0}^{(j=1)} = a_n, \quad c_{l>0}^{(j=1)} = 0, \quad (\text{B.59a})$$

$$d_{m=0}^{(j=1)} = 1, \quad d_{m>0}^{(j=1)} = 0, \quad (\text{B.59b})$$

$$c_l^{(j)} = a_{n-j+1} d_l^{(j-1)}, \quad (\text{B.59c})$$

$$d_m^{(j)} = d_m^{(j-1)} - z_{n-j+1} c_m^{(j-1)} + c_{m-1}^{(j-1)}. \quad (\text{B.59d})$$

Again, let us consider the example of $n = 4$:

$$f^4(z) = \frac{a_1}{1 + \frac{a_2(z-z_1)}{1 + \frac{a_3(z-z_2)}{1 + a_4(z-z_3)}}}, \quad (\text{B.60})$$

B. Derivations

$$4 : c_0^{(1)} = a_4, \tag{B.61a}$$

$$d_0^{(1)} = 1,$$

$$3 : c_0^{(2)} = a_3 d_0^{(1)}, \tag{B.61b}$$

$$d_0^{(2)} = d_0^{(1)} - z_3 c_0^{(1)},$$

$$d_1^{(2)} = c_0^{(1)},$$

$$2 : c_0^{(3)} = a_2 d_0^{(2)}, \tag{B.61c}$$

$$c_1^{(3)} = a_2 d_1^{(2)},$$

$$d_0^{(3)} = d_0^{(2)} - z_2 c_0^{(2)},$$

$$d_1^{(3)} = d_1^{(2)} + c_0^{(2)},$$

$$1 : c_0^{(4)} = a_1 d_0^{(3)},$$

$$c_1^{(4)} = a_1 d_1^{(3)}, \tag{B.61d}$$

$$d_0^{(4)} = d_0^{(3)} - z_1 c_0^{(3)},$$

$$d_1^{(4)} = d_1^{(3)} - z_1 c_1^{(3)} + c_0^{(3)},$$

$$d_2^{(4)} = c_1^{(3)}.$$

C. Formalism

C.1. Sum convention

Repeated indices in 4-vector notation are summed over

$$x = (\tau, \mathbf{x}) \text{ and } k = (i\nu, \mathbf{k}), \quad (\text{C.1})$$

$$\sum_x = \int_0^\beta d\tau \sum_{\mathbf{x}}, \quad (\text{C.2})$$

$$\sum_k = \frac{1}{\beta} \sum_\nu \frac{1}{N_{\mathbf{k}}} \sum_{\mathbf{k}}, \quad (\text{C.3})$$

when not stated otherwise.

C.2. n-particle Green's functions

The n -particle imaginary time Green's function is defined as

$$G_{i_1 \dots i_{2n}}^{(n)}(\tau_1, \dots, \tau_{2n}) = (-1)^n \langle \mathcal{T}_\tau \left[\hat{c}_{i_1}(\tau_1) \hat{c}_{i_2}^\dagger(\tau_2) \hat{c}_{i_3}(\tau_3) \dots \hat{c}_{i_{2n}}^\dagger(\tau_{2n}) \right] \rangle, \quad (\text{C.4})$$

$$= \frac{1}{Z} \text{Tr} \left(e^{-\beta H} \mathcal{T}_\tau \left[\hat{c}_{i_1}(\tau_1) \hat{c}_{i_2}^\dagger(\tau_2) \hat{c}_{i_3}(\tau_3) \dots \hat{c}_{i_{2n}}^\dagger(\tau_{2n}) \right] \right), \quad (\text{C.5})$$

$$Z = \text{Tr} (e^{-\beta H}) \text{ and } \hat{c}_{i_j}^{(\dagger)}(\tau_j) = e^{\tau_j H} \hat{c}_{i_j}^{(\dagger)} e^{-\tau_j H} \quad (\text{C.6})$$

where even indices are creation, \hat{c}^\dagger , and odd indices are annihilation operators, \hat{c} .

The one-particle Green's function is defined as

$$G_{\mathbf{k}}(\tau) = G_{\mathbf{k}\sigma, \mathbf{k}\sigma}^{(1)}(\tau, 0) = -\langle \mathcal{T}_\tau \left[\hat{c}_{\mathbf{k}\sigma}(\tau) \hat{c}_{\mathbf{k}\sigma}^\dagger(0) \right] \rangle, \quad (\text{C.7})$$

$$G_{\mathbf{k}\nu} = \int_0^\beta d\tau e^{i\nu\tau} G_{\mathbf{k}}(\tau). \quad (\text{C.8})$$

C.3. Fourier transformation and Matsubara frequencies

$$\hat{c}_{\mathbf{k}\nu}^\dagger = \sum_{\mathbf{x}} \int_0^\beta d\tau e^{i(\nu\tau + \mathbf{k}\mathbf{x})} \hat{c}_{\mathbf{x}}^\dagger(\tau), \quad (\text{C.9})$$

$$\hat{c}_{\mathbf{x}}^\dagger(\tau) = \frac{1}{\beta} \sum_{\nu, \mathbf{k}} e^{-i(\nu\tau + \mathbf{k}\mathbf{x})} \hat{c}_{\mathbf{k}\nu}^\dagger \quad (\text{C.10})$$

C. Formalism

and complex conjugated for \hat{c} .

The single-particle Green's function

$$G_{\mathbf{k}\nu} = \int_0^\beta d\tau \sum_{\mathbf{x}} e^{i(\nu\tau + \mathbf{k}\mathbf{x})} G_{\mathbf{x}}(\tau), \quad (\text{C.11})$$

$$G_{\mathbf{x}}(\tau) = \frac{1}{\beta} \sum_{\nu} \frac{1}{N_{\mathbf{k}}} \sum_{\mathbf{k}} e^{-i(\nu\tau + \mathbf{k}\mathbf{x})} G_{\mathbf{k}\nu} \quad (\text{C.12})$$

$$\text{Fermionic: } \mathbf{k}, \nu = \frac{\pi}{\beta}(2n + 1), \quad (\text{C.13})$$

$$\text{Bosonic: } \mathbf{q}, \omega = \frac{\pi}{\beta}2n, \quad (\text{C.14})$$

D. Angle-resolved photoemission spectroscopy (ARPES)

▶ ARPES explained 

The basic idea of angle-resolved photoemission spectroscopy (ARPES) is to excite photoelectrons by means of a monochromatic beam and measure the kinetic energy of the emitted electrons under a specific angle. As is schematically shown in Figure D.1. The measurement of the angle-resolved spectrum¹ has a one-to-one relation to the one-particle spectral function

$$A(\omega, \mathbf{k}) = -\frac{1}{\pi} \Im G^R(\omega, \mathbf{k}). \quad (\text{D.1})$$

The general concept of the photoelectric effect, which was originally observed by Hertz in 1887 [108] and later explained by Einstein in 1905 [?] is shown in Figure D.2 (left). Assume the photon with energy $\hbar\omega$ is able to excite electrons with binding energy E_B of filled bands in the valance band, and possibly core-levels. In addition to the binding energy, the work function² Φ_0 of the sample must be overcome, yielding a kinetic energy E_{kin} of the photoelectron, given as

$$E_{\text{kin}} = \hbar\omega - |E_B| - \Phi_0. \quad (\text{D.2})$$

The measurement of E_{kin} corresponds to photoelectron spectroscopy (PES). In ARPES

¹In addition to the inverse ARPES.

² The energy needed by an electron on the Fermi surface in order to leave the material

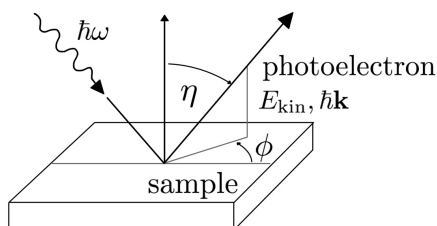


Figure D.1.: Angle-resolved photoemission spectroscopy (ARPES). A photon $\hbar\omega$ is absorbed by the sample, which subsequently emits a photoelectron with kinetic energy E_{kin} and momentum $\hbar\mathbf{k}$ under the polar angle θ and azimuthal angle ϕ .

D. Angle-resolved photoemission spectroscopy (ARPES)

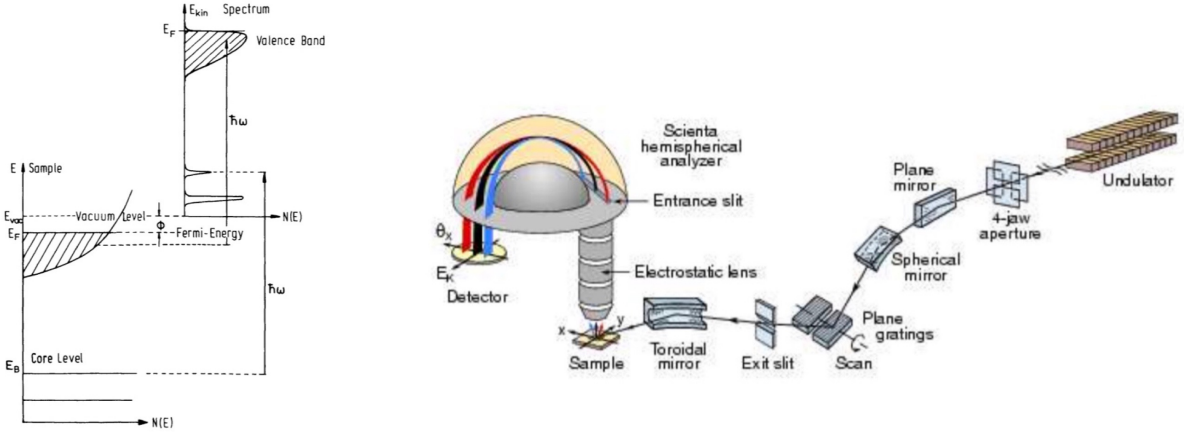


Figure D.2.: ARPES (left) Relation between the energy levels in a solid and electron distribution produced by photons of energy $\hbar\omega$. [109] (right) Schematic experimental setup.[110]

the emission angles, i.e. the angle of the emitted photoelectron to the surface normal (θ) and azimuthal angle (ϕ) are measured in addition to the energy spectrum. Hence, the momentum $\hbar\mathbf{k}$ is completely determined, with absolute value of $|\mathbf{k}| = \sqrt{2mE_{kin}/\hbar^2}$. The component parallel to the surface of the momentum is conserved resulting in the following simple expression for the lattice momentum inside the solid

$$\hbar\mathbf{k}_{\parallel} = \sqrt{2mE_{kin}} \sin(\theta), \quad (D.3)$$

where m is the mass of the electron and \mathbf{k}_{\parallel} is given in the extended zone scheme³. Here, the momentum of the photon is neglected. Note that the copper-oxide planes in cuprates are quasi two-dimensional planes and hence, \mathbf{k}_{\parallel} , corresponding to $k_x = |\mathbf{k}_{\parallel}| \cos(\phi)$ and $k_y = |\mathbf{k}_{\parallel}| \sin(\phi)$, is all we are interested in.

A prototypical beamline of the experimental setup is shown in Figure D.2 (right). A synchrotron beam is extracted from a so-called insertion device⁴ and subsequently monochromized and focused onto a sample. The emitted photoelectrons are collected by an analyser, where the kinetic energy and emission angles are determined. Note that the experimental setup is situated in high vacuum. [110] [109]

The ARPES spectra measured for $\text{HgBa}_2\text{CuO}_{4+\delta}$, which is subject of this work, is shown in Figure D.3. The I. M. Vishik et al. carefully optimized the ARPES procedure for $\text{HgBa}_2\text{CuO}_{4+\delta}$, which is extremely sensitive to experimental conditions. Two

³ Not reducing the \mathbf{k}_{\parallel} to the first Brillouin zone

⁴ Synchrotron: Electrons are bend by a magnetic field to travel on a circle emitting bremsstrahlung. Insertion device: Arrays of magnets with alternating magnetic fields form a straight section in the synchrotron. The electrons move on a sinusoidal trajectory due to the alternating poles. This leads to emission of synchrotron radiation at each turn. Insertion devices are classified by the periodicity of the alternating magnetic fields resulting in continuous or tunable quasi-discrete spectra. The classes are called wigglers and undulators, respectively.

D. Angle-resolved photoemission spectroscopy (ARPES)

of the main challenges are mentioned here: Firstly, the crystal structure lacks a neutral cleavage plane. The unit cell of $\text{HgBa}_2\text{CuO}_{4+\delta}$ is made of layers (with charge): $\text{Cu}^{2+}\text{O}_2^{2-}$ (-2), Ba^{2+} (+2), O^{-2} (-2), Hg^{2+} (+2), O^{-2} (-2) and Ba^{2+} (+2). This can be seen in Figure 2.1. Hence, neighboring planes have opposite charge and therefore a slice of layers would lead to polar catastrophe, which is compensated by self-doping or mixed-termination⁵. [111] Secondly, the intensity yield against the background (BG) varies rapidly with the photon energy. The quasiparticle peak could only be observed for the range $19 \text{ eV} \leq \hbar\omega \leq 19.4 \text{ eV}$, near the nodal point.

In Figure D.3 (a) - (f) the intensity of the electron yield with binding energy $E_B = E - E_F$, as in Equation (D.2), is plotted over the lattice momentum parallel to the surface, as in Equation (D.3). The plots correspond to different angles θ , as defined in Figure D.3 in the top right corner. The Fermi momentum k_F is the point at which the energy distribution curve is closest to the Fermi energy E_F , as is marked in (b) by a red line. In Figure D.3 (g) the BG measurement is shown, while in (h) the measurement of the sample at k_F is shown. By subtracting BG from the k_F measurement the density of filled states that were excited by the procedure, becomes visible. We observe a pronounced peak near the Fermi surface for close to the nodal point at $\theta = 45^\circ$. The so-called quasiparticle peak appears only in a narrow range $\theta \geq 27^\circ$. This could mean that the filled states do not get excited for any reason, or as is commonly believed. The spectral function shows a strong \mathbf{k} -dependence, where there is no quasiparticle peak at the anti-nodal points with $\theta = 0^\circ$ and 90° . Further the constant shift or step that is observed for $E - E_F < 0$ with respect to $E - E_F > 0$ is due to secondary electrons that encountered inelastic scattering, as is commonly observed in ARPES spectra. [112] [113]

Other cuprate compounds have been investigated. Here is a list of literature we referred to: [113], [12], [114], [115], [112], [116], [110] and [109].

⁵The surface layer is not distinct.

D. Angle-resolved photoemission spectroscopy (ARPES)

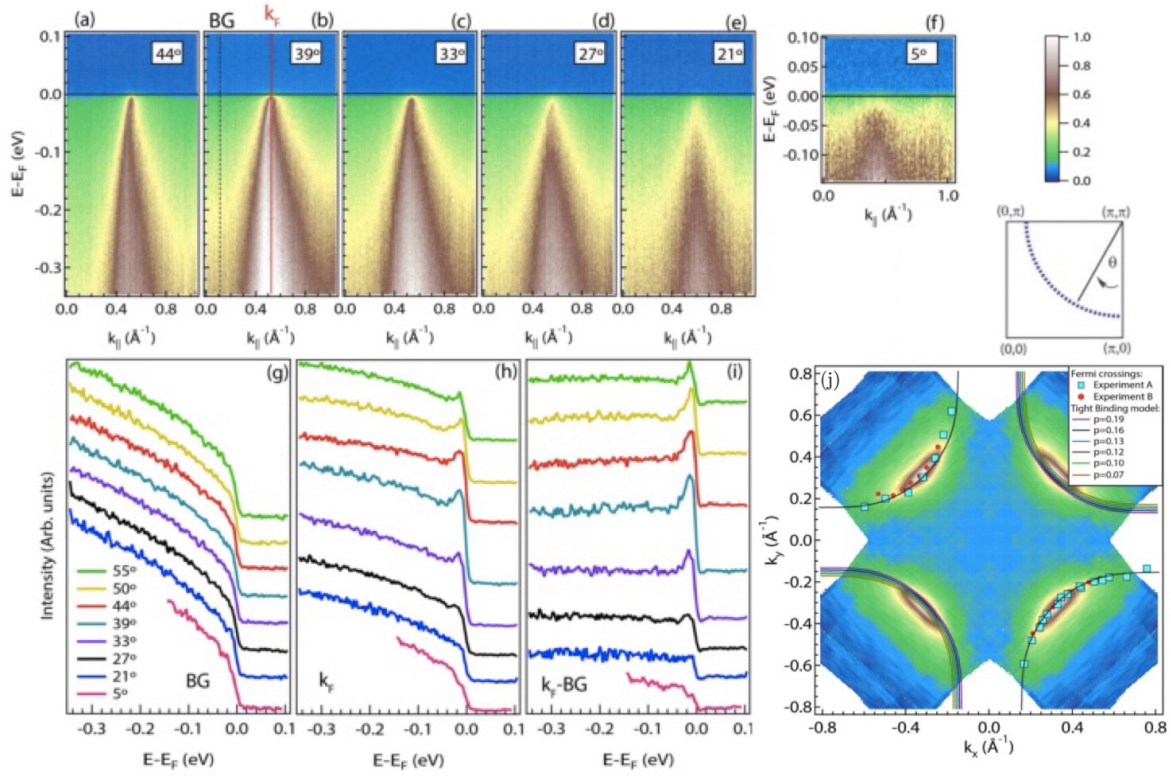


Figure D.3.: ARPES (a)-(f) Near-nodal cuts at different angles θ showing the energy distribution curve (ECD) as a function of the crystal momentum component k_{\parallel} . All images have the same linear color scale. Color scale, which is in arbitrary units, and θ are defined on the right hand side. Data taken with 19 eV photons, cuts parallel to $\Gamma(0,0)M(\pi,\pi)$, and $T = 10$ K. Red vertical line in (b) marks k_F and black dashed line marks momentum of BG of EDCs. (g) BG EDCs, taken at momentum indicated in (b). (h) EDC at k_F . (i) EDC at k_F with BG EDC subtracted. (j) Fermi surface map, k_F for each cut, and tight-binding model Fermi surfaces. Map is produced by integrating cuts within a $[20]meV$ window centered at E_F . Four-fold symmetrization is applied to the color map, but not k_F data. Red and blue symbols are Fermi surface crossings for two different experiments on two different batches of crystals. Experiment A was performed with 19 eV photons and experiment B was performed with 19.4 eV photons. Solid lines are tight-binding Fermi surfaces enclosing different volumes, that are not our concern here. [113]

Bibliography

- [1] N. Barišić, M. K. Chan, M. J. Veit, C. J. Dorow, Y. Ge, Y. Tang, W. Tabis, G. Yu, X. Zhao, and M. Greven, *Hidden Fermi-liquid behavior throughout the phase diagram of the cuprates* (2015).
- [2] H. K. Onnes, *The resistance of pure mercury at helium temperatures*, Commun. Phys. Lab. Univ. Leiden, **12**, 120 (1911).
- [3] W. Meissner and R. Ochsenfeld, *Ein neuer Effekt bei Eintritt der Supraleitfähigkeit*, Die Naturwissenschaften, **21**, 787 (1933).
- [4] J. Bardeen, *Theory of the Meissner Effect in Superconductors*, Physical Review, **97**, 1724 (1955).
- [5] L. N. Cooper, *Bound Electron Pairs in a Degenerate Fermi Gas*, Physical Review, **104**, 1189 (1956).
- [6] J. Bardeen, L. N. Cooper, and J. R. Schrieffer, *Microscopic Theory of Superconductivity*, Physical Review, **106**, 162 (1957).
- [7] J. Bardeen, L. N. Cooper, and J. R. Schrieffer, *Theory of Superconductivity*, Physical Review, **108**, 1175 (1957).
- [8] J. G. Bednorz and K. A. Mueller, *Possible high T_c superconductivity in the $Ba?La?Cu?O$ system*, Zeitschrift fuer Physik B Condensed Matter, **64**, 189 (1986).
- [9] N. M. Plakida, *Spin fluctuations and high-temperature superconductivity in cuprates*, Physica C: Superconductivity and its Applications, **531**, 39 (2016).
- [10] M. Imada, A. Fujimori, and Y. Tokura, *Metal-insulator transitions*, Reviews of Modern Physics, **70**, 1039 (1998).
- [11] M. Atikur Rahman, M. Zahidur Rahaman, and M. Nurush Samsuddoha, *A Review on Cuprate Based Superconducting Materials Including Characteristics and Applications*, American Journal of Physics and Applications(Online) Md. Atikur Rahman, Md. Zahidur Rahaman, Md. Nurush Samsuddoha. A Review on Cuprate Based Superconducting Materials Including Characteristics and Applications. American Journal of Physics and Applications, **3**, 39 (2015).
- [12] T. Tohyama and S. Maekawa, *Angle-resolved photoemission in high T_c cuprates from theoretical viewpoints*, Superconductor Science and Technology, **13**, R17 (2000).

Bibliography

- [13] S. Sachdev, *Where is the quantum critical point in the cuprate superconductors?*, *physica status solidi (b)*, **247**, 537 (2010).
- [14] Y. Li, V. Balédent, N. Barišić, Y. Cho, B. Fauqué, Y. Sidis, G. Yu, X. Zhao, P. Bourges, and M. Greven, *Unusual magnetic order in the pseudogap region of the superconductor $\text{HgBa}_2\text{CuO}_{4-\delta}$* , *Nature*, **455**, 372 (2008).
- [15] N. Plakida, *High-Temperature Cuprate Superconductors*, volume 166 of *Springer Series in Solid-State Sciences*, Springer Berlin Heidelberg, Berlin, Heidelberg (2010).
- [16] H. J. *Electron Correlations in Narrow Energy Bands*, *Proceedings of the Royal Society of London A: Mathematical, Physical and Engineering Sciences*, **276** (1963).
- [17] M. C. Gutzwiller, *Effect of Correlation on the Ferromagnetism of Transition Metals*, *Physical Review Letters*, **10**, 159 (1963).
- [18] J. Kanamori, *Electron Correlation and Ferromagnetism of Transition Metals*, *Progress of Theoretical Physics*, **30**, 275 (1963).
- [19] M. Born and R. Oppenheimer, *Zur Quantentheorie der Molekeln*, *Annalen der Physik*, **389**, 457 (1927).
- [20] K. Held, *Electronic Structure Calculations using Dynamical Mean Field Theory*, *Advances in Physics*, **56**, 829 (2007).
- [21] P. Hohenberg and W. Kohn, *Inhomogeneous Electron Gas*, *Physical Review*, **136**, B864 (1964).
- [22] W. Kohn and L. J. Sham, *Self-Consistent Equations Including Exchange and Correlation Effects*, *Physical Review*, **140**, A1133 (1965).
- [23] C. Rodriguez, N. Christensen, and E. Peltzer y Blancá, *Electronic structure of mercury-based high- T_c compounds: $\text{HgBa}_2\text{Cu}_n\text{O}_{2n+2}$ ($n = 1,2,3$)*, *Physica C: Superconductivity*, **216**, 12 (1993).
- [24] O. K. Andersen, *Linear methods in band theory*, *Physical Review B*, **12**, 3060 (1975).
- [25] O. K. Andersen, T. Saha-Dasgupta, R. W. Tank, C. Arcangeli, O. Jepsen, and G. Krier, *Developing the MTO Formalism* (1999).
- [26] G. H. Wannier, *The Structure of Electronic Excitation Levels in Insulating Crystals*, *Physical Review*, **52**, 191 (1937).
- [27] N. Marzari and D. Vanderbilt, *Maximally localized generalized Wannier functions for composite energy bands*, *Physical Review B*, **56**, 12847 (1997).

Bibliography

- [28] O. Andersen, A. Liechtenstein, O. Jepsen, and F. Paulsen, *LDA energy bands, low-energy hamiltonians, t' , t'' , t_{\perp} (k), and J_{\perp}* , Journal of Physics and Chemistry of Solids, **56**, 1573 (1995).
- [29] P. Hansmann, N. Parragh, A. Toschi, G. Sangiovanni, and K. Held, *Importance of d - p Coulomb interaction for high T_C cuprates and other oxides*, New Journal of Physics, **16**, 033009 (2013).
- [30] V. J. Emery, *Theory of high- T_C Superconductivity in Oxides*, Physical Review Letters, **58**, 2794 (1987).
- [31] A. V. Boris, N. N. Kovaleva, O. V. Dolgov, T. Holden, C. T. Lin, B. Keimer, and C. Bernhard, *In-Plane Spectral Weight Shift of Charge Carriers in $YBa_2Cu_3O_{6.9}$* , Science, **304**, 708 (2004).
- [32] M. Ortolani, P. Calvani, and S. Lupi, *Frequency-Dependent Thermal Response of the Charge System and the Restricted Sum Rules of $La_{2-x}Sr_xCuO_4$* , Physical Review Letters, **94**, 067002 (2005).
- [33] A. Toschi, M. Capone, M. Ortolani, P. Calvani, S. Lupi, and C. Castellani, *Temperature Dependence of the Optical Spectral Weight in the Cuprates: Role of Electron Correlations*, Physical Review Letters, **95**, 097002 (2005).
- [34] A. Comanac, L. de' Medici, M. Capone, and A. J. Millis, *Optical conductivity and the correlation strength of high-temperature copper-oxide superconductors*, Nature Physics, **4**, 287 (2008).
- [35] A. Toschi and M. Capone, *Optical sum rule anomalies in the cuprates: Interplay between strong correlation and electronic band structure*, Physical Review B, **77**, 014518 (2008).
- [36] D. Nicoletti, O. Limaj, P. Calvani, G. Rohringer, A. Toschi, G. Sangiovanni, M. Capone, K. Held, S. Ono, Y. Ando, and S. Lupi, *High-temperature optical spectral weight and fermi-liquid renormalization in bi-based cuprate superconductors*, Physical Review Letters, **105**, 077002 (2010).
- [37] L. de' Medici, X. Wang, M. Capone, and A. J. Millis, *Correlation strength, gaps, and particle-hole asymmetry in high- T_c cuprates: A dynamical mean field study of the three-band copper-oxide model*, Physical Review B, **80**, 054501 (2009).
- [38] X. Wang, L. de' Medici, and A. J. Millis, *Theory of oxygen K edge x-ray absorption spectra of cuprates*, Physical Review B, **81**, 094522 (2010).
- [39] J. Zaanen, G. A. Sawatzky, and J. W. Allen, *Band gaps and electronic structure of transition-metal compounds*, Physical Review Letters, **55**, 418 (1985).

Bibliography

- [40] G. Ghiringhelli, M. Le Tacon, M. Minola, S. Blanco-Canosa, C. Mazzoli, N. B. Brookes, G. M. De Luca, A. Frano, D. G. Hawthorn, F. He, T. Loew, M. M. Sala, D. C. Peets, M. Salluzzo, E. Schierle, R. Sutarto, G. A. Sawatzky, E. Weschke, B. Keimer, and L. Braicovich, *Long-Range Incommensurate Charge Fluctuations in $(Y,Nd)Ba_2Cu_3O_{6+x}$* , *Science*, **337**, 821 (2012).
- [41] A. J. Achkar, R. Sutarto, X. Mao, F. He, A. Frano, S. Blanco-Canosa, M. Le Tacon, G. Ghiringhelli, L. Braicovich, M. Minola, M. Moretti Sala, C. Mazzoli, R. Liang, D. A. Bonn, W. N. Hardy, B. Keimer, G. A. Sawatzky, and D. G. Hawthorn, *Distinct Charge Orders in the Planes and Chains of Ortho-III-Ordered $YBa_2Cu_3O_{6+\delta}$ Superconductors Identified by Resonant Elastic X-ray Scattering*, *Physical Review Letters*, **109**, 167001 (2012).
- [42] J. Chang, E. Blackburn, A. T. Holmes, N. B. Christensen, J. Larsen, J. Mesot, R. Liang, D. A. Bonn, W. N. Hardy, A. Watenphul, M. v. Zimmermann, E. M. Forgan, and S. M. Hayden, *Direct observation of competition between superconductivity and charge density wave order in $YBa_2Cu_3O_{6.67}$* , *Nature Physics*, **8**, 871 (2012).
- [43] S. Blanco-Canosa, A. Frano, E. Schierle, J. Porras, T. Loew, M. Minola, M. Bluschke, E. Weschke, B. Keimer, and M. Le Tacon, *Resonant x-ray scattering study of charge-density wave correlations in $YBa_2Cu_3O_{6+x}$* , *Physical Review B*, **90**, 054513 (2014).
- [44] W. Tabis, Y. Li, M. L. Tacon, L. Braicovich, A. Kreyssig, M. Minola, G. Dellea, E. Weschke, M. J. Veit, M. Ramazanoglu, A. I. Goldman, T. Schmitt, G. Ghiringhelli, N. Barišić, M. K. Chan, C. J. Dorow, G. Yu, X. Zhao, B. Keimer, and M. Greven, *Charge order and its connection with Fermi-liquid charge transport in a pristine high- T_c cuprate*, *Nature Communications*, **5**, 5875 (2014).
- [45] E. H. da Silva Neto, R. Comin, F. He, R. Sutarto, Y. Jiang, R. L. Greene, G. A. Sawatzky, and A. Damascelli, *Charge ordering in the electron-doped superconductor $Nd_{2-x}CexCuO_4$* , *Science*, **347** (2015).
- [46] R. Comin, R. Sutarto, E. H. da Silva Neto, L. Chauviere, R. Liang, W. N. Hardy, D. A. Bonn, F. He, G. A. Sawatzky, and A. Damascelli, *Broken translational and rotational symmetry via charge stripe order in underdoped $YBa_2Cu_3O_{6+y}$* , *Science*, **347** (2015).
- [47] R. Comin, A. Frano, M. M. Yee, Y. Yoshida, H. Eisaki, E. Schierle, E. Weschke, R. Sutarto, F. He, A. Soumyanarayanan, Y. He, M. Le Tacon, I. S. Elfimov, J. E. Hoffman, G. A. Sawatzky, B. Keimer, and A. Damascelli, *Charge Order Driven by Fermi-Arc Instability in $Bi_2Sr_{2-x}LaxCuO_{6+\delta}$* , *Science*, **343**, 390 (2014).
- [48] E. H. da Silva Neto, P. Aynajian, A. Frano, R. Comin, E. Schierle, E. Weschke, A. Gyenis, J. Wen, J. Schneeloch, Z. Xu, S. Ono, G. Gu, M. Le Tacon, and A. Yaz-

Bibliography

- dani, *Ubiquitous Interplay Between Charge Ordering and High-Temperature Superconductivity in Cuprates*, *Science*, **343**, 393 (2014).
- [49] T. Wu, H. Mayaffre, S. Krämer, M. Horvatić, C. Berthier, W. Hardy, R. Liang, D. Bonn, and M.-H. Julien, *Incipient charge order observed by NMR in the normal state of YBa₂Cu₃O_y*, *Nature Communications*, **6**, 6438 (2015).
- [50] S. Peli, S. D. Conte, R. Comin, N. Nembrini, A. Ronchi, P. Abrami, F. Banfi, G. Ferrini, D. Brida, S. Lupi, M. Fabrizio, A. Damascelli, M. Capone, G. Cerullo, and C. Giannetti, *The room temperature prodrome of charge-order in copper oxides* (2015).
- [51] P. Werner, R. Sakuma, F. Nilsson, and F. Aryasetiawan, *Dynamical screening in La₂CuO₄*, *Physical Review B*, **91**, 125142 (2015).
- [52] M. Tsuchiizu, Y. Yamakawa, and H. Kontani, *p-orbital density wave with d symmetry in high-T_c cuprate superconductors predicted by the renormalization-group + constrained RPA theory* (2015).
- [53] Y. Yamakawa and H. Kontani, *Spin-Fluctuation-Driven Nematic Charge-Density Wave in Cuprate Superconductors: Impact of Aslamazov-Larkin Vertex Corrections*, *Physical Review Letters*, **114**, 257001 (2015).
- [54] P. Werner and M. Casula, *Dynamical screening in correlated electron systems—from lattice models to realistic materials*, *Journal of Physics: Condensed Matter*, **28**, 383001 (2016).
- [55] F. Aryasetiawan, T. Miyake, and R. Sakuma, *The Constrained RPA Method for Calculating the Hubbard U from First-Principles* *Graduate School of Advanced Integration Science*, **1** (2011).
- [56] G. Rohringer, H. Hafermann, A. Toschi, A. A. Katanin, A. E. Antipov, M. I. Katsnelson, A. I. Lichtenstein, A. N. Rubtsov, and K. Held, *Diagrammatic routes to non-local correlations beyond dynamical mean field theory* (2017).
- [57] T. Ayrál, S. Biermann, and P. Werner, *Screening and nonlocal correlations in the extended Hubbard model from self-consistent combined *G W* and dynamical mean field theory*, *Physical Review B*, **87**, 125149 (2013).
- [58] N. E. Bickers, *Self-Consistent Many-Body Theory for Condensed Matter Systems*, In D. Sénéchal, A.-M. Tremblay, and C. Bourbonnais, editors, *Theoretical Methods for Strongly Correlated Electrons*, 237–296, Springer New York, New York, NY (2004).
- [59] a. Altland and B. Simons, *Condensed Matter Field Theory*, volume 115 (2010).

Bibliography

- [60] A. A. Abrikosov, L. P. Gorkov, I. E. Dzyaloshinski, and I. E. Dzyaloshinski, *Methods of Quantum Field Theory in Statistical Physics*, Dover Books on Physics Series, Dover Publications (1975).
- [61] K. Yamada, *Electron Correlations in Metals*, Cambridge University Press (2004).
- [62] A. Georges, G. Kotliar, W. Krauth, and M. J. Rozenberg, *Dynamical mean-field theory of strongly correlated fermion systems and the limit of infinite dimensions*, Reviews of Modern Physics, **68**, 13 (1996).
- [63] N. Parragh, A. Toschi, K. Held, and G. Sangiovanni, *Conserved quantities of $SU(2)$ -invariant interactions for correlated fermions and the advantages for quantum Monte Carlo simulations*, Physical Review B, **86**, 155158 (2012).
- [64] P. Gunacker, M. Wallerberger, E. Gull, A. Hausoel, G. Sangiovanni, and K. Held, *Continuous-time quantum Monte Carlo using worm sampling*, Physical Review B, **92**, 155102 (2015).
- [65] P. Gunacker, M. Wallerberger, T. Ribic, A. Hausoel, G. Sangiovanni, and K. Held, *Worm-improved estimators in continuous-time quantum Monte Carlo*, Physical Review B, **94**, 125153 (2016).
- [66] J. Kaufmann, P. Gunacker, and K. Held, *Continuous-time quantum Monte Carlo calculation of multi-orbital vertex asymptotics* (2017).
- [67] M. Caffarel and W. Krauth, *Exact diagonalization approach to correlated fermions in infinite dimensions: Mott transition and superconductivity*, Physical Review Letters, **72**, 1545 (1994).
- [68] G. Rohringer, A. Valli, and A. Toschi, *Local electronic correlation at the two-particle level*, Physical Review B, **86**, 125114 (2012).
- [69] G. Rohringer, *New routes towards a theoretical treatment of nonlocal electronic correlations*, 318 (2013).
- [70] I. T. Dyatlov, V. V. Sudakov, and K. A. Ter-Martirosyan, *Asymptotic meson-meson dispersion theory*, Sov. Phys. JETP, **4**, 767 (1957).
- [71] T. Schäfer, *Classical and quantum phase transitions in strongly correlated electron systems* (2016).
- [72] A. Toschi, A. A. Katanin, and K. Held, *Dynamical vertex approximation: A step beyond dynamical mean-field theory*, Physical Review B - Condensed Matter and Materials Physics, **75** (2007).
- [73] K. Held, A. A. Katanin, and A. Toschi, *Dynamical vertex approximation – an introduction* (2008).

Bibliography

- [74] G. Baym and L. P. Kadanoff, *Conservation Laws and Correlation Functions*, Physical Review, **124**, 287 (1961).
- [75] G. Rohringer and A. Toschi, *Impact of non-local correlations over different energy scales: A Dynamical Vertex Approximation study*, 1–31 (2016).
- [76] T. A. Maier, M. Jarrell, and D. J. Scalapino, *Pairing interaction in the two-dimensional Hubbard model studied with a dynamic cluster quantum Monte Carlo approximation*, Physical Review B, **74**, 094513 (2006).
- [77] A. N. Rubtsov, M. I. Katsnelson, and A. I. Lichtenstein, *Dual fermion approach to nonlocal correlations in the Hubbard model*, Physical Review B, **77**, 033101 (2008).
- [78] H. Hafermann, *Numerical approaches to spatial correlations in strongly interacting fermion systems*, Ph.D. thesis, Universität Hamburg (2009).
- [79] T. Ribic, P. Gunacker, S. Isakov, M. Wallerberger, G. Rohringer, A. N. Rubtsov, E. Gull, and K. Held, *Role of three-particle vertex within dual fermion calculations* (2017).
- [80] J. Gukelberger, E. Kozik, and H. Hafermann, *Diagrammatic Monte Carlo approach for diagrammatic extensions of dynamical mean-field theory – convergence analysis of the dual fermion technique* (2016).
- [81] W. H. Press, S. A. Teukolsky, W. T. Vetterling, and B. P. Flannery, *Numerical Recipes: The Art of Scientific Computing* (2007).
- [82] C. Kim, P. J. White, Z.-X. Shen, T. Tohyama, Y. Shibata, S. Maekawa, B. O. Wells, Y. J. Kim, R. J. Birgeneau, and M. A. Kastner, *Systematics of the Photoemission Spectral Function of Cuprates: Insulators and Hole- and Electron-Doped Superconductors*, Physical Review Letters, **80**, 4245 (1998).
- [83] M. Hashimoto, T. Yoshida, H. Yagi, M. Takizawa, A. Fujimori, M. Kubota, K. Ono, K. Tanaka, D. H. Lu, Z.-X. Shen, S. Ono, and Y. Ando, *Doping evolution of the electronic structure in the single-layer cuprate $\text{Bi}_{2-x}\text{Sr}_{2-x}\text{La}_x\text{CuO}_{6+d}$: Comparison with other single-layer cuprates*, Physical Review B, **77**, 094516 (2008).
- [84] M. K. Chan, C. J. Dorow, L. Mangin-Thro, Y. Tang, Y. Ge, M. J. Veit, G. Yu, X. Zhao, A. D. Christianson, J. T. Park, Y. Sidis, P. Steffens, D. L. Abernathy, P. Bourges, and M. Greven, *Commensurate antiferromagnetic excitations as a signature of the pseudogap in the tetragonal high- T_c cuprate $\text{HgBa}_2\text{CuO}_{4+\delta}$* , Nature Communications, **7**, 10819 (2016).
- [85] H. Eskes, M. B. J Meinders, and G. A. Sawatzky, *Anomalous Transfer of Spectral Weight in Doped Strongly Correlated Systems*, Physical Review Letters, **67**, 1035 (1991).

Bibliography

- [86] P. Cai, W. Ruan, Y. Peng, C. Ye, X. Li, Z. Hao, X. Zhou, D. H. Lee, and Y. Wang, *Visualizing the evolution from the Mott insulator to a charge-ordered insulator in lightly doped cuprates*, *Nature Physics*, **12**, 1047 (2016).
- [87] I. Sega and P. Prelovsek, *Quasiparticle properties in effective models for strongly correlated electrons*, *PHYSICAL REVIEW B*, **42** (1990).
- [88] S. Sakai, S. Blanc, M. Civelli, Y. Gallais, M. Cazayous, M.-A. Méasson, J. S. Wen, Z. J. Xu, G. D. Gu, G. Sangiovanni, Y. Motome, K. Held, A. Sacuto, A. Georges, and M. Imada, *Raman-Scattering Measurements and Theory of the Energy-Momentum Spectrum for Underdoped $\text{Bi}_2\text{Sr}_2\text{CaCuO}_{8+\delta}$ Superconductors: Evidence of an s -Wave Structure for the Pseudogap*, *Physical Review Letters*, **111**, 107001 (2013).
- [89] J. Otsuki, M. Ohzeki, H. Shinaoka, and K. Yoshimi, *Sparse modeling approach to analytical continuation of imaginary-time quantum Monte Carlo data*, *Physical Review E*, **95**, 061302 (2017).
- [90] H. Kontani, *Transport Phenomena in Strongly Correlated Fermi Liquids*, volume 251 (2013).
- [91] R. Kubo, *Statistical-Mechanical Theory of Irreversible Processes. I. General Theory and Simple Applications to Magnetic and Conduction Problems*, *Journal of the Physical Society of Japan*, **12**, 570 (1957).
- [92] R. Kubo, *Wigner Representation of Quantum Operators and Its Applications to Electrons in a Magnetic Field*, *Journal of the Physical Society of Japan*, **19**, 2127 (1964).
- [93] H. Fukuyama, H. Ebisawa, and Y. Wada, *Theory of Hall Effect. I*, *Progress of Theoretical Physics*, **42**, 494 (1969).
- [94] H. Fukuyama, *Theory of Hall Effect. II*, *Progress of Theoretical Physics*, **42**, 1284 (1969).
- [95] R. Peierls, *Zur Theorie des Diamagnetismus von Leitungselektronen*, *Zeitschrift fuer Physik*, **80**, 763 (1933).
- [96] J. M. Tomczak, *Spectral and Optical Properties of Correlated Materials*, Ph.D. thesis (2007).
- [97] H. Kohno and K. Yamada, *A General Expression for Hall Coefficient Based on Fermi Liquid Theory*, *Progress of Theoretical Physics*, **80**, 623 (1988).
- [98] H. Kontani, K. Kanki, and K. Ueda, *Hall effect and resistivity in high- T_c superconductors: The conserving approximation*, *Physical Review B*, **59**, 14723 (1999).

Bibliography

- [99] N. E. Bickers, D. J. Scalapino, and S. R. White, *Conserving approximations for strongly correlated electron systems: Bethe-salpeter equation and dynamics for the two-dimensional hubbard model*, Physical Review Letters, **62**, 961 (1989).
- [100] L.-F. Arsenault, R. Neuberg, L. A. Hannah, and A. J. Millis, *Projected regression method for solving Fredholm integral equations arising in the analytic continuation problem of quantum physics*, Inverse Problems, **33**, 115007 (2017).
- [101] P. Werner, S. Hoshino, and H. Shinaoka, *Spin-freezing perspective on cuprates*, PHYSICAL REVIEW B, **94** (2016).
- [102] S. N. Putilin, E. V. Antipov, O. Chmaissem, and M. Marezio, *Superconductivity at 94 K in HgBa₂CuO_{4+δ}*, Nature, **362**, 226 (1993).
- [103] S. Putilin, E. Antipov, and M. Marezio, *Superconductivity above 120 K in HgBa₂CaCu₂O_{6+δ}*, Physica C: Superconductivity, **212**, 266 (1993).
- [104] E. Antipov, S. Loureiro, C. Chailout, J. Capponi, P. Bordet, J. Tholence, S. Putilin, and M. Marezio, *The synthesis and characterization of the HgBa₂Ca₂Cu₃O_{8+δ} and HgBa₂Ca₃Cu₄O_{10+δ} phases*, Physica C: Superconductivity, **215**, 1 (1993).
- [105] K. Lokshin, D. Pavlov, M. Kovba, E. Antipov, I. Kuzemskaya, L. Kulikova, V. Davydov, I. Morozov, and E. Itskevich, *Synthesis and characterization of overdoped Hg-1234 and Hg-1245 phases; the universal behavior of T_c variation in the HgBa₂Can-1CunO_{2n+2+δ} series*, Physica C: Superconductivity, **300**, 71 (1998).
- [106] A. Iyo, Y. Tanaka, H. Kito, Y. Kodama, P. M. Shirage, D. D. Shivagan, K. Tokiwa, and T. Watanabe, *Material synthesis of HgBa₂Can-1CunO_y multilayered cuprates under high pressure*, Journal of Physics: Conference Series, **108**, 012046 (2008).
- [107] E. V. Antipov, A. M. Abakumov, and S. N. Putilin, *Chemistry and structure of Hg-based superconducting Cu mixed oxides*, Superconductor Science and Technology, **15**, R31 (2002).
- [108] D. M. Edwards and J. A. Hertz, *Electron-magnon interactions in itinerant ferromagnetism. II. Strong ferromagnetism*, Journal of Physics F: Metal Physics, **3**, 2191 (1973).
- [109] S. Hüfner, *Photoelectron spectroscopy: principles and applications* (2003).
- [110] A. Damascelli, Z.-X. Shen, and Z. Hussain, *Angle-resolved photoemission spectroscopy of the cuprate superconductors* (2002).
- [111] N. Nakagawa, H. Y. Hwang, and D. A. Muller, *Why some interfaces cannot be sharp* (2006).

Bibliography

- [112] W. S. Lee, T. Yoshida, W. Meevasana, K. M. Shen, D. H. Lu, W. L. Yang, X. J. Zhou, X. Zhao, G. Yu, Y. Cho, M. Greven, Z. Hussain, and Z.-X. Shen, *Study of HgBa₂CuO_{4+δ} by Angle-Resolved Photoemission Spectroscopy* (2006).
- [113] I. M. Vishik, N. Barišić, M. K. Chan, Y. Li, D. D. Xia, G. Yu, X. Zhao, W. S. Lee, W. Meevasana, T. P. Devereaux, M. Greven, and Z.-X. Shen, *Angle-resolved photoemission spectroscopy study of HgBa₂CuO_{4+δ}*, *Physical Review B*, **89**, 195141 (2014).
- [114] D. S. Dessau, Z.-X. Shen, D. M. King, D. S. Marshall, L. W. Lombardo, P. H. Dickinson, A. G. Loeser, J. DiCarlo, C.-h. Park, A. Kapitulnik, and W. E. Spicer, *Key features in the measured band structure of Bi₂Sr₂CaCu₂O_{8+δ}: Flat bands at E_F and Fermi surface nesting*, *Physical Review Letters*, **71**, 2781 (1993).
- [115] T. Timusk and B. Statt, *The pseudogap in high-temperature superconductors: an experimental survey*, *Reports on Progress in Physics*, **62**, 61 (1999).
- [116] P. A. Lee, N. Nagaosa, and X. G. Wen, *Doping a Mott insulator: Physics of high-temperature superconductivity*, *Reviews of Modern Physics* (2006).